SPACE WEATHER AND THE MOST MICROSATELLITE

by KRISTINA A. SKARET
B.Sc., McGill University, 1998

A THESIS SUBMITTED IN PARTIAL FULFILMENT OF
THE REQUIREMENTS FOR THE DEGREE OF
MASTER OF SCIENCE

in

THE FACULTY OF GRADUATE STUDIES

Department of Physics and Astronomy

We accept this thesis as conforming
to the required standard

THE UNIVERSITY OF BRITISH COLUMBIA

April, 2001

In presenting this thesis in partial fulfilment of the requirements for an advanced degree at the University of British Columbia, I agree that the Library shall make it freely available for reference and study. I further agree that permission for extensive copying of this thesis for scholarly purposes may be granted by the head of my department or by his or her representatives. It is understood that copying or publication of this thesis for financial gain shall not be allowed without my written permission.

Department of Physics and Astronomy
The University of British Columbia
Vancouver, Canada
Date April 26, 2001

Abstract

The MOST (*M*icrovariability and *O*scillations of *St*ars) microsatellite is designed to obtain the most precise stellar photometry ($\Delta L/L \sim 10^{-6}$) ever achieved. In preparation for the launch of the first satellite devoted to asteroseismology, a complete evaluation of space weather in the baseline orbit including radiation analysis is performed, providing a 'weather forecast' for the mission in order to assist the MOST instrument team with crucial planning decisions.

Results of assessing the effects of space weather include recommendations for the choice of orbit, design structure, operating guidelines, and data reduction guidelines. This analysis has aided the MOST team to convince the Canadian Space Agency (CSA) to identify a launch vehicle capable of taking MOST to a polar sun-synchronous orbit. Preliminary shielding recommendations have been incorporated into the mechanical design of the telescope. Estimates of the amount of degradation the CCD will experience, including the number of Single Event Effects (SEEs, effects caused by interaction with a single cosmic ray), have influenced current operating procedure guidelines. It is shown that radiation doses to the CCD are not expected to cause critical failure of the detector. A minimum mission lifetime is established for a worse-case radiation environment and found to be of sufficiently long duration to meet all primary scientific objectives. As the impact of the radiation environment (and other orbital environment related factors) is less than critical thresholds, the forecast for the MOST microsatellite looks 'sunny and warm'.

Table of Contents

List of Tables:

List of Figures:

LIST OF ACRONYMS

ACR: Anomalous Cosmic Rays
ACS: Attitude Control System
CCD: Charge-Coupled Device
CME: Coronal Mass Ejection
CRAND: Cosmic Ray Albedo Neutron Decay
CREME: Cosmic Ray Effects on Micro-Electronics
CRRES: Combined Release and Radiation Effects Satellite
CVZ: Continuous Viewing Zone
DAO: Dominion Astrophysical Observatory
DSNU: Dark Signal Non-Uniformity
ESRTC: European Space Research and Technology Center
FUSE: Far-infrared Ultraviolet Explorer
FES: Fine Error Sensor
GCR: Galactic Cosmic Radiation
HST: Hubble Space Telescope
IGRF: International Geomagnetic Reference Field
IMO: Inverted Mode
MIS: Metal Insulating Semiconductor
MOS: Metal Oxide Semiconductor
MOSFET: Metal Oxide Semiconductor Field Effect Transistor
MOST: Microvariability and Oscillations of Stars
LEO: Low Earth Orbit
ONV: Orbit Normal Vector
QE: Quantum Efficiency
SAA: South Atlantic Anomaly
SEB: Single Event Burnout
SEE: Single Event Effects
SEF: Single Event Failure
SEFI: Single Event Functional Interrupt
SEGR: Single Event Gate Rupture
SEL: Single Event Latchup
SEP: Solar Energetic Particle
SEU: Single Event Upsets
SHE: Single Hard Error
SOHO: Solar and Heliospheric Observatory
SPENVIS: Space Environment Information System
WET: Whole Earth Telescope
WIRE: Wide-field Infra-Red Explorer

Acknowledgements and Dedication

Many people have contributed to this thesis in many different ways. On the academic side, my sincere thanks go out to my supervisor, Jaymie Matthews, for always staying interested and patient, with his sense of humour constantly prevailing. I am also grateful to the MOST science team at UBC, Rainer Kuschnig, Gordon Walker, Ron Johnston, John Pazder, and Evgenya Shkolnik for their comments and discussions, and for their support of my work, and to our partners at CSA (Glen Campbell) and Dynacon. I'm grateful to Stephenson Yang for introducing me to the world of observational astronomy. And of course, I owe much to Janet Johnson, our graduate secretary at UBC for her endless patience and great advice, as well as to all my friends and family who helped me through hard times by providing good times (you know who you are!).

This thesis is dedicated to my father, Dr. Reg J. Skaret (1949-2000). His incredible support, encouragement, and enthusiasm ensured that I follow my dreams. I could not have completed this project without his guidance. He was an amazing man, and an even more amazing father. As you read this thesis, know that I owe much of every success in my life to him. He will be truly missed.

Look dad - I finished!

Chapter 1: Introduction

1.1 Space Weather and Astronomy

Astronomers who use space telescopes don't have to cope with the hassles of a cloudy night at the observatory, or poor seeing due to atmospheric interference. At first glance, the space environment would appear to be very calm and 'weather-free'. But on closer inspection, one finds that low-Earth orbit (LEO) is actually quite active, has its own weather, and its own set of problems which space astronomers must be aware of.

The chance to peer out at space from outside the atmosphere affords astronomers the ability to analyse wavelength regions opaque through the Earth's atmosphere. For others, the telescope needs to be in orbit about the Earth to escape the scintillation noise associated with a turbulent atmosphere and to have a complete duty cycle. The sensitivity and capacity of micro-electronics such as memory devices, signal processors, and photo-electric detectors has provided astronomers with a new chance to probe regimes not before open for observation. However, the trade-off has repetitively been an increasing sensitivity to the charged particle environment associated with the space environment.

The near-Earth radiation environment is complex. All variety of atoms, from light protons to uranium nuclei (z=92), are accelerated to high energies by a wide variety of sources, some of which remain mysteries even today. Plasma from the solar wind constantly injects and replenishes the supply of charged particles which bombard satellites. Hence, the number and intensity of the particles varies strongly during the solar cycle.

The presence of 'cosmic radiation' first discovered in 1912 by Hess (Van Allen 1983) creates adverse conditions in the space orbital environment. During very strong Coronal Mass Ejections (CMEs) from the sun, charged particle interaction with the Earth's magnetosphere can be so severe that charged particles reach northern latitudes, disrupting power supplies, creating dangerous currents through long oil pipelines, and wiping out radio communications. These events are few and isolated to solar maximum here on Earth. However, in the orbital environment with less geomagnetic shielding, satellites experience much higher doses as well as a greater duration of exposure to

charged particles. Thus, satellites in LEO must be designed to tolerate isolated solar events associated with a large flux of charged particles as well as the ambient flux of charged particles mostly concentrated in the Van Allen Radiation belts.

The radiation environment can produce a myriad of hazards to an orbiting spacecraft. The most critical effect is a Single Event Failure (SEF) in which a single interaction between a charged particle and an onboard micro-electronic (usually memory) device causes critical failure. Luckily, SEFs are very rare in modern satellites as critical microelectronics are normally duplicated to provide onboard redundancy, or backup. SEFs are just one of a class of effects called Single Event Effects (SEEs; Section 6.2) which are caused by a single particle interaction with a micro-electronic device. Most SEEs do not interrupt normal operations but do necessitate regular ground communications with the satellite including regular uplink of operating sequences to avoid more critical effects.

The presence of the Van Allen Radiation belts and the implications of regular traverses through their particle rich environments often influences the choice of orbit for a satellite (Chapter 4). In the heart of the radiation belts in LEO (a feature called the South Atlantic Anomaly (SAA) because of its geographical location) it is often not possible to collect good data. Charged particles may hit detectors creating spurious signal (Section 4.2), or as in the case of the Hubble Space Telescope (HST), the satellite may be powered down in order to reduce long term damage. For space asteroseismology missions such as MOST (Section 1.3), one great advantage of being in orbit is the ability to observe a target for an extended period of time. Thus, the loss of data through the SAA can be detrimental to meeting science goals.

Regular passes through the radiation belts also cause cumulative damage in sensitive microelectronics. Gradually, charged particles can destroy the physical properties of specific devices. In particular, silicon lattices are broken down by charged particles. Charge coupled devices (CCDs; Section 1.4) are one type of device utilised regularly by astronomers and space astronomers alike and are susceptible to this effect of space weather. Charge may also accumulate within circuits over time. If the cumulative charge buildup is sufficiently high to create a discharge, critical failure is a possibility depending on the design of the satellite.

Space astronomers must also be aware of how the orbital environment effects parts specific to telescopes. Coatings used on optical components could potentially interact with atomic oxygen to cause browning.

In order to mitigate the damage caused by space weather and avoid critical failures, it is essential for a thorough radiation analysis to be performed on a spacecraft. A satellite should always use radiation hardened parts, on-board redundancy in critical operating devices, and regular planned ground communications. Incorporation of a space 'weather forecast' into operating procedure and data reduction guidelines will help ensure all scientific goals will be met. A good knowledge of the ambient radiation environment of the satellite should also provide a minimum mission lifetime estimate and be used in designing the satellite to make sure there is sufficient on-board shielding.

1.2 Space Weather and MOST

The aim of this thesis is to provide a complete radiation analysis for the MOST (*M*icrovariability and *O*scillations of *S*tars) microsatellite in order to assist the MOST instrument team with crucial planning decisions, essentially providing the 'weather forecast' for the mission. A brief introduction to the MOST mission and the MOST CCD is found in Sections 1.3 and 1.4 respectively.

Chapter 2 is a primer on the physical processes that trap particles in the Earth's magnetosphere. Chapter 3 describes the approach to modeling the radiation environment employed in this study.

In Chapter 4, the baseline orbital parameters are evaluated for the MOST microsatellite mission. This analysis has aided the MOST team to convince the Canadian Space Agency (CSA) to identify a launch vehicle capable of taking MOST to a polar sun-synchronous orbit. Deviations in Local Time of Ascending Node (LTAN) were shown to adversely affect science operations and hence, launch opportunities to these orbits were ruled out.

Chapter 5 employs the techniques outlined in Chapter 3 to assess the radiation environment for the baseline orbit. The radiation environment of the baseline orbit was used to provide a forecast for MOST.

This weather forecast has played important role in the development of the MOST microsatellite mission. As this work was progressing, so was the mechanical design of the telescope. Based on results presented here, the design was fine-tuned such that sufficient shielding is present to protect sensitive spacecraft parts, yet minimum amounts of heavy materials are used in order to reduce mass constraints. Current operating procedure guidelines were established in conjunction with this study in order to minimise impact on scientific data due to cosmic rays (Section 4.2) and single event effects (SEEs, Section 6.2). A minimum mission lifetime was established for a worse-case radiation environment and found to be of sufficiently long duration to meet all primary scientific objectives. As the impact of the radiation environment (and other orbital environment related factors) is less than critical thresholds, the forecast for the MOST microsatellite looks 'sunny and warm'.

1.3 The MOST microsatellite: A Space Seismology Pioneer

The MOST space satellite project is unique in Canadian astronomy. Funded by the Canadian Space Agency (CSA), MOST is Canada's first microsatellite mission (the bus is roughly the dimension and mass of a suitcase). A picture of the satellite itself is shown in Figure 1.1. The driving science goal behind MOST is to probe the internal structure and central composition of nearby stars by measuring brightness oscillations with amplitudes as small as a few micro-magnitudes to apply the techniques of asteroseismology.

Figure 1.1 Photo of a mock-up of the MOST microsatellite with coffee mug showing scale.

Asteroseismology was born through helioseismology, the study of the five-minute oscillations of the sun (Demarque & Guenther 1999). It has allowed astronomers to peer into the sun's interior and compare results to the Standard Solar Model (Matthews 1990). Similar to the way geophysicists use pressure waves (p-waves) created by

earthquakes to infer the thickness and composition of the Earth's internal layers, asteroseismologists use sound waves, induced by convective turbulence of the Sun's surface, to probe the sun's interior. Asteroseismologists use spherical harmonics to describe the *nonradial pulsations* created by sound waves as they resonate in acoustic cavities beneath the solar surface. As the behavior of the sound waves is directly related to the medium in which they travel, the mode patterns imprinted on the stellar surface by these waves contains information on the internal structure and composition of the star. Thus, the tools of an asteroseismologist are the eigenfrequencies (and to a lesser extent, amplitudes) of the mode patterns (Tassoul 1990). The difference between asteroseismology and helioseismology is that only simple nonradial patterns (i.e. low degree (l) and high overtone (n)) are detectable when observing the integrated light from a point source. The sun is resolvable as a disk and thus, even high spatial frequency modes which do not result in variations of the total disc are detectable.

The challenge in the observation of seismic oscillations is the relatively low change in either Doppler velocity or overall brightness of the star. The Doppler velocities due to vibration of the Sun in integrated light are only a few cm/s, and the overall brightness fluctuations are on the order of a few micromagnitudes. Current ground-based detection thresholds are ~3 m/s in Doppler velocity and 100 micromagnitudes in brightness fluctuations (photometric precision is limited by noise due to atmospheric scintillation). Recent reports of oscillations in alpha Ursae Majoris by Busazi et al. (1999), using the starsensor camera onboard the failed infrared satellite WIRE, show that it is possible to detect low amplitude stellar variability from space. However, the variations correspond to periods of days and hours, and amplitudes of hundreds of micromagnitudes, well above the regime to be explored by MOST.

The MOST design is optimized to detect oscillations of amplitudes of a few micromag in as few as ten days of monitoring a star brighter than V~6 (solar p-modes decay in ~10 days). In order to detect solar-type oscillations of 4 ppm amplitude in a V=3.0 magnitude star with 99% confidence, the rms noise level must be below 1.08% ppm, equivalent to a signal to noise (S/N) value of 3.7 (Matthews & Kuschnig 2000). Table 1.1 shows the detection limits based on numerical simulations performed by Kuschnig (2000). Maintaining a high duty cycle will reduce relative background noise

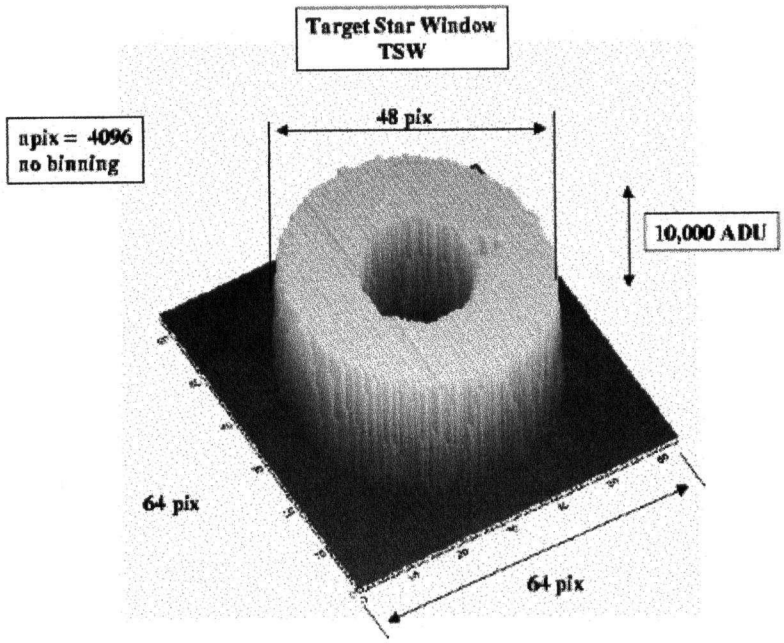

Figure 1.2 Fabry microlens pupil image as projected on the CCD (after Matthews & Kuschnig, 2000b)

contributions to allow MOST to resolve fine structure in the stellar eigenfrequency spectrum, a particularly sensitive tool for measuring core He fraction. Thus, we will be able to date *individual* main sequence stars. Asteroseismology of metal poor subdwarfs, believed to be the oldest objects in the galaxy due to their primitive composition, will allow us to place a meaningful lower limit on the age of the Milky Way and the Universe.

The MOST team has adopted a simple design for the space photometer. A 15-cm Maksutov telescope feeds a Charge Coupled Device (CCD) camera with a set of Fabry microlenses positioned above the detector focal plane. The starbeam is directed onto one of these lenses, which projects an image of the telescope pupil onto the CCD, covering about 2000 pixels in total. As the starbeam moves over the lens due to the tracking errors of the attitude control system (ACS), the pupil image remains fixed on the same pixels (Figure 1.2). This minimises the MOST instrumental sensitivity to image wander and CCD flatfield variations. A schematic of the Focal plane with science CCD and Attitude Control System (ACS) CCD is shown in Figure 1.3. The microlens array is only projected onto a small area of the science CCD. Since many of the MOST science targets

(Appendix A) are very bright (>V~2), the light must be spread out over a sufficiently large number of pixels in order to reduce the amount of saturation in a given exposure. However, the light must be concentrated enough so that when observing fainter targets (V<6), the telescope still operates in a high signal regime. One pupil image spans 80 × 80 pixels.

More background on the MOST mission and its specific science goals can be found at the MOST website: http://www.astro.ubc.ca/MOST/

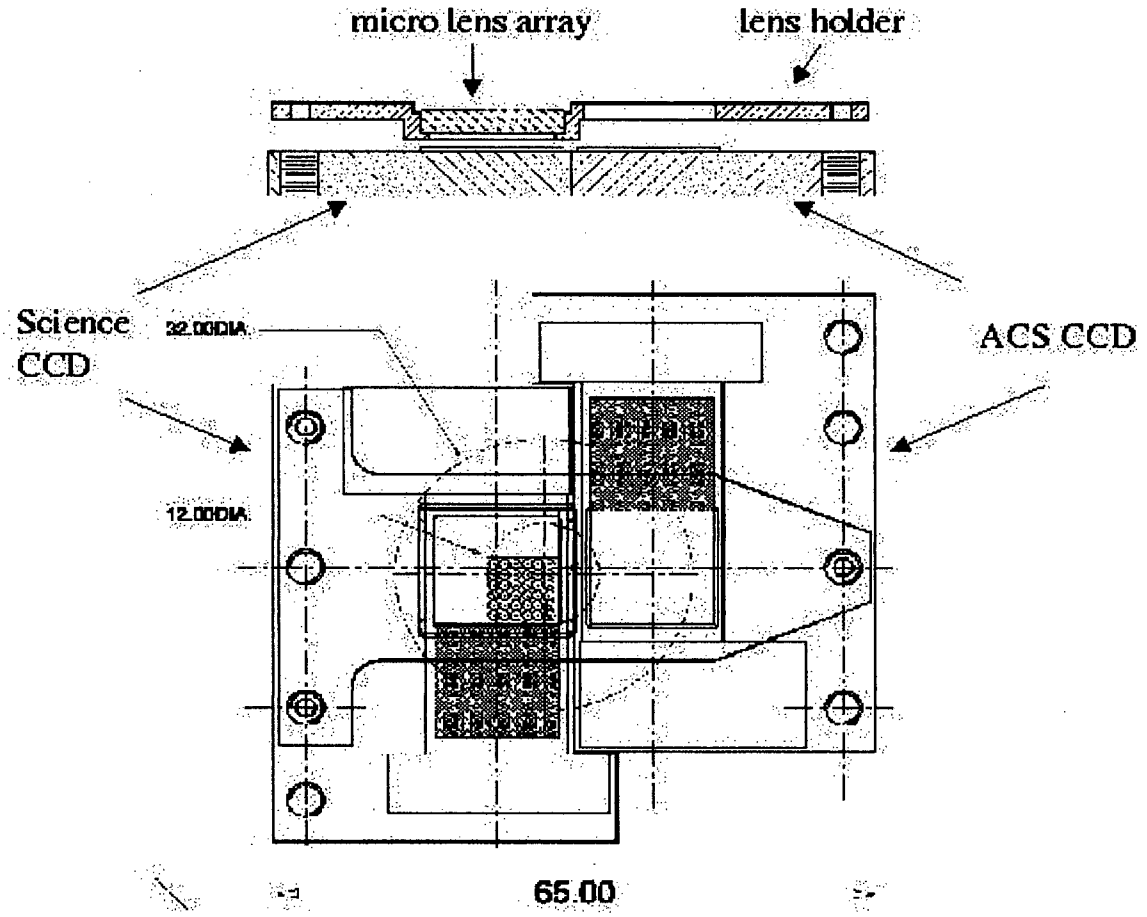

Figure 1.3 Schematic of the MOST focal plane showing Science and ACS CCDs. The dotted line circles represent the optical axis of the telescope. The Fabry microlens array focuses a pupil image of the star onto the lower right hand corner of the science CCD.

1.4 Charge-Coupled Devices (CCDs)

Although they were first developed as memory devices, CCDs have replaced photographic film in virtually every optical and near infra-red astronomical imaging camera, since the silicon lattice that they are made of is naturally light sensitive through the photoelectric effect. Astronomers can manipulate the digital images which are produced by CCDs and subtract off noise sources such as the background from the sky.

The fundamental building block of a CCD is a metal-insulator-semiconductor (MIS) capacitor. The capacitor collects and stores charge packets, and then transfers the charge packet to another capacitor in series when the voltage gating the charge is changed. Hence, the CCD is dubbed a *charge coupled* device. Each MIS capacitor is arranged in a string or row called a serial-shift register, down which charge packets shift. In a 2-D imaging CCD, the serial shift registers are arranged row by row to form a 2-D plate of capacitors, each individually sensitive to light falling on it through the photoelectric effect. The image is projected onto this 2-D plate, and electrons are generated in each capacitor in proportion to the intensity of the light falling on it. Then the voltage-gated channels are manipulated such that a single charge packet from each serial shift register is transferred down the row to a perpendicular serial shift register (Figure 1.4). This perpendicular shift register collects a number of charge packets equal to the number of rows of serial shift registers in the 2-D device and transfers them one by one to a recording device or output amplifier. Once the perpendicular shift register is 'empty', the net charge packet in each of the parallel shift registers is read out.

Charges are generated through the photoelectric effect, but must be stored before they are collected. In the standard operation of a CCD, a positive voltage is applied across the gate of the MIS capacitor, less than the Fermi potential (threshold potential above which electrons can start moving) needed to attract a substantial number of electrons. Electron-hole pairs are generated and pushed away by the buildup of current in the capacitor, towards the edges of the capacitor or column isolation regions. This leaves a region devoid of electron-hole pairs, or a region of *depletion.* As electrons are generated they collect in the depletion region. To trap electrons in the center of the

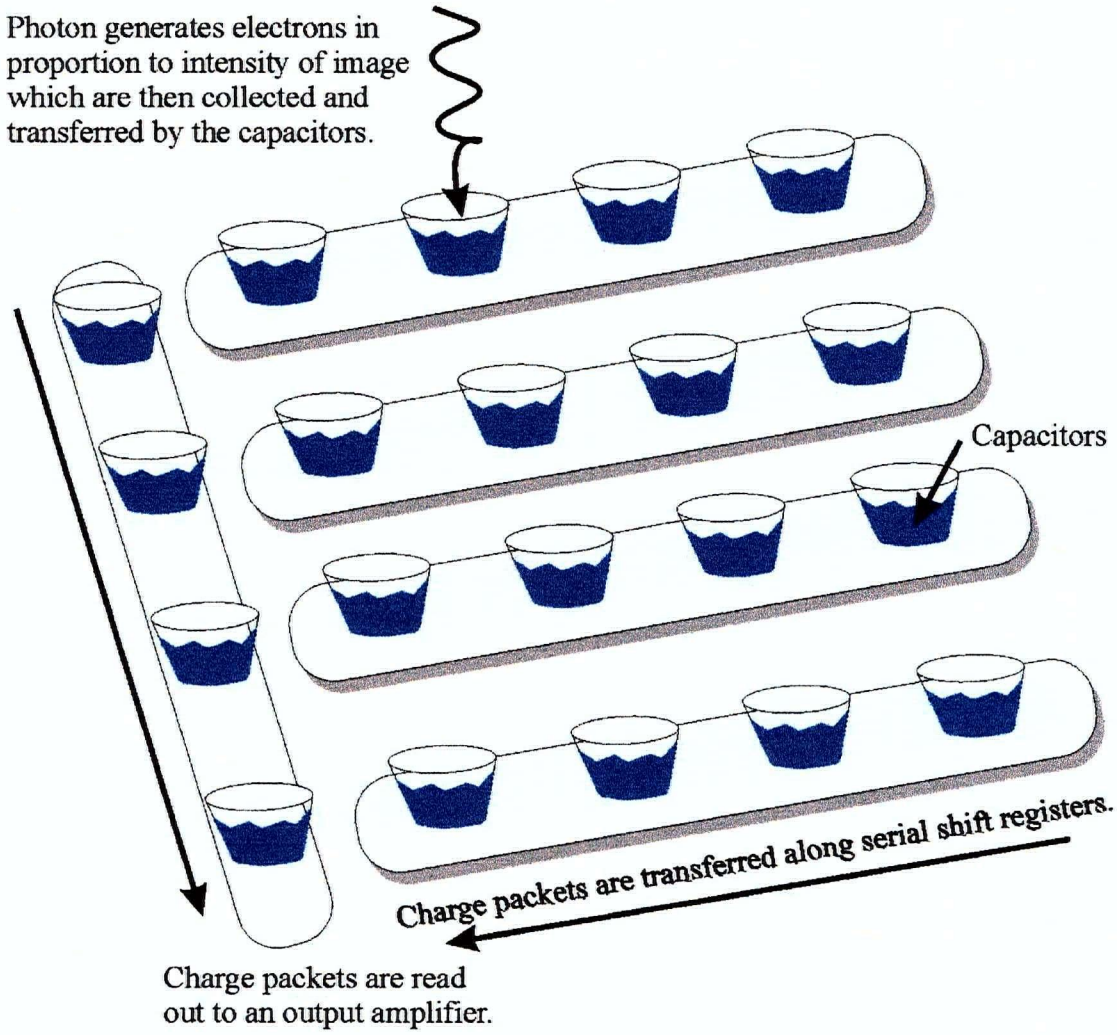

Figure 1.4 Schematic of CCD function. Buckets of water are representative of capacitors collecting charge. The perpendicular serial shift register is responsible for reading out the rest of the 2D array to the output amplifier in order to record the image. (After Hardy, 1997)

capacitor, or pixel, the capacitor has three polysilicon gates, or electrodes supplying voltage through the capacitor, as illustrated by Figure 1.5. The middle electrode is biased such that the potential well created underneath the surface has a minimum in the central region of the pixel, where the electrons gather. Channel stops on the sides of the pixel and the collection of electron hole pairs at the perimeter of the CCD further acts as barriers, trapping the electrons in the center of the pixel. For a more detailed history and description of CCDs, see Hardy (1997).

The precision of CCDs makes them an ideal detector for the MOST microsatellite. Tests in demonstration of the functionality of the Kepler mission by Jenkins et al. (1996) showed that a back-illuminated Reticon CCD was capable of detecting planetary transits, a signal that is only about 80 ppm of the target stars brightness (once calibrated for the effects of motion). In fact, the tests showed that the CCD was shot noise limited and capable of detecting a signal at a level of 3 ppm. The MOST CCD is manufactured by Marconi, and is slightly different from the Reticon CCD in dimension and sensitivity. However, numerical simulations of the MOST photometer by Kuschnig show that stellar oscillation signals will be detected (Matthews & Kuschnig 2000a). In observations of a 4th magnitude star, the noise level of ~1 ppm will be dominantly due to photon shot noise (>70%), a reduced duty cycle (>7%, Section 4.3), and stellar granulation noise (~5%). A solar oscillation spectrum will be detected with 99% confidence at 4.1 ppm. Table 1 shows the results of the numerical simulations for stars of varying magnitude.

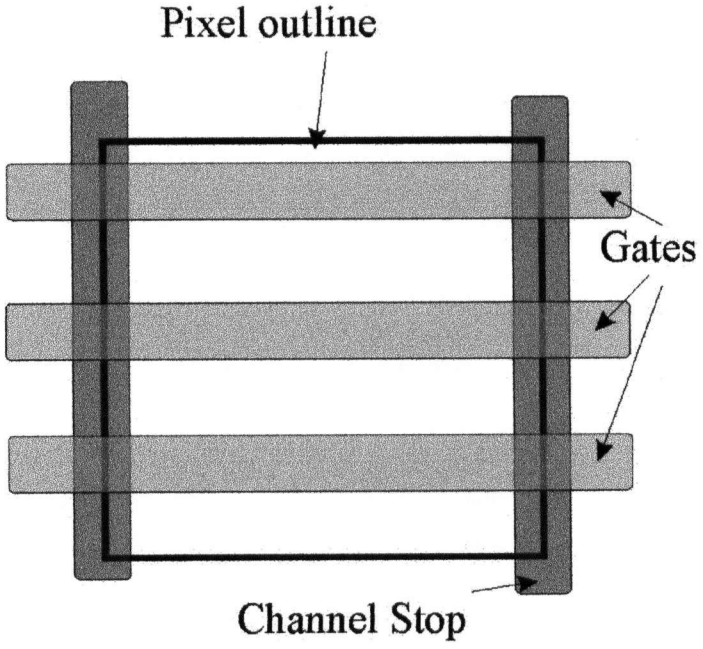

Figure 1.5 Top view of CCD pixel, showing three gates.

Target star magnitude (V)	exposure time (s)	data rate #/min	noise level (ppm)	signal detection limit (ppm) (99%)	time base (days)
0.4	1	10	0.72	2.6	10
1.2	2	10	0.72	2.6	10
3	12	5	1.02	3.7	10
4	30	2	1.14	4.1	20
6	60	1	1.92	6.9	40

Table 1.1 Noise level and detection limits at a 99% confidence level based on numerical simulations of the MOST microsatellite (after Matthews & Kuschnig 2000a).

1.4.1 The MOST CCD

MOST will use two identical CCDs in the focal plane; the devices are custom packaged version of the 47-20 type built by Marconi (formerly EEV Ltd.). CCD specifications of the science grade MOST CCDs are listed in Table 1.2 (Further information on the off-the-shelf model of CCD47-20 is in Appendix F).

Noise at 150 KHz	6.7 rms e^-
Mean Dark Signal at -30°C	16.3 e^-/pixel/minute
Peak Signal	119 k e^-/pixel
Serial CTE	0.999996 - 1.000002
Parallel CTE	0.999998 - 0.999997
Quantum Efficiency	
at 400 nm	44.8%
at 500 nm	83.0%
at 650 nm	90.2%
Pixels	1024 x 1024
Pixel Size	13 x 13 μm
Peak charge storage	120,000 e^-/pixel

Table 1.2 Description of CCD47-20 and results from testing of the MOST science grade CCD.

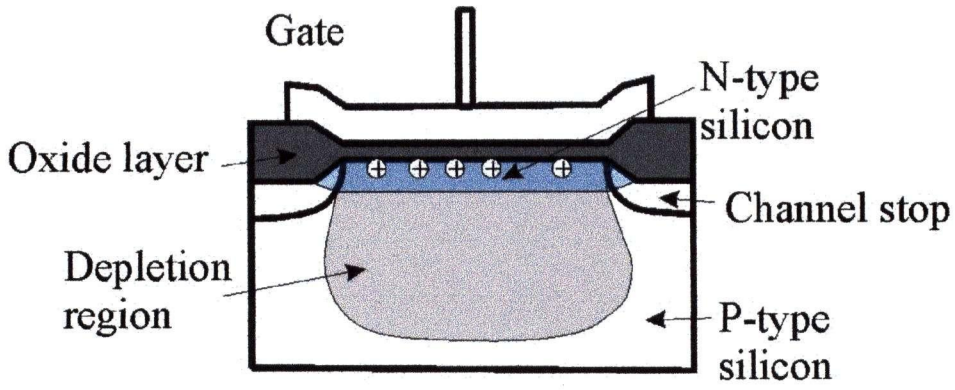

Figure 1.6 Schematic of typical buried channel CCD, in inverted mode. In an inverted mode, electron hole pairs accumulate at the silicon oxide interface layer.

CCD47-20 is a 1024 x 1024, back illuminated device, with pixels 13 μm wide. The CCD structure is based on a p-type, epitaxial layer of silicon about 10-20 microns thick, covered by an insulating layer of silicon dioxide about 1000 Angstroms thick. This structure is sandwiched between the plates of a MIS (Metal Insulated Semiconductor) capacitor (Figure 1.6). The CCD47-20 device is back-illuminated in order to increase quantum efficiency (QE), a measure of the rate at which an electron is produced by incoming photon. That is, in order to prevent photons from being stopped by the insulating oxide layer and not penetrating into the p-silicon where the photoelectric effect occurs and signal is generated, the CCD is basically flipped over and the p-silicon substrate is etched or thinned. The p-silicon is then directly illuminated so that photons generate electrons to be immediately collected. Thus, back-illuminated devices generate a greater signal (i.e. higher QE).

CCD47-20 is operated in an inverted mode (IMO) and utilizes MPP (Multi-Pin-Phased) technology in order to reduce dark current. In an inverted mode, the silicon-to-silicon-dioxide interface is held in inversion (the potential in the gate high and electron-hole pairs accumulate). If the voltage across the electrode is less than about -6 V, the bias on the electrode is sufficiently negative as to attract electron-hole pairs to the oxide interface surface. Then the surface is said to be *inverted*, and the layer containing the electron hole pairs is called the *inversion layer.* As the holes flood this layer, they fill the interface states, blocking electrons from the interface region and trapping them in the buried channels. This also serves to reduce the pathway for electrons excited thermally

from moving from the valence band to the conduction band, reducing or eliminating dark current (Section 6.1.1). However, if the entire pixel is operated in inversion, then the electrons are no longer confined to their pixel. To overcome this, an implant is placed below one of the electrodes. The implant alters the potential well in the device such that electrons can not penetrate through the region underneath that electrode. Thus, a potential barrier is set up by the implant along one side of the pixel, trapping the charge inside. With this device architecture, dark current is significantly suppressed, and charge packets are effectively stored in a single pixel for a specified integration time.

The silicon-silicon dioxide interface is a poor place to store and/or transfer charge because of a high density of trapping states, or potential wells which tend to house electrons or electron-hole pairs for extended periods of time. The trapping states simply arise from a disruption in the silicon lattice structure. Thus, CCDs usually store and transfer charge within the p-type silicon layer. In order to force the electrons to depth in the structure, the p surface is coated with a silicon lattice rich in n-type impurities, or an n-type silicon layer. The n-type silicon is doped such that it is positively biased with respect to the p-type layer. Hence, electrons are collected and transferred in the p-type layer, removed from the silicon-silicon dioxide interface. Thus, this type of device is called a *buried channel device.*

The CCD is the most sensitive component of the MOST telescope to the orbital environment.

Chapter 2: The Theory behind Space Weather

2.1 History

The aurorae borealis gave scientists the first important clues about charged particle motion in the Earth's magnetic field. In fact, "cosmic" radiation was first detected by Birkeland in 1895 in a vacuum chamber experiment designed to study the aurorae borealis (Van Allen 1983). However, it was another 10 years before it was recognised that the source of ionising energy was extraterrestrial, when it was observed that the amount of ionization in the chambers rose with increasing altitude (c.f. Klecker 1996).

Building on Birkeland's work, and motivated to show that the aurorae are generated by charged electrons and ions trapped in the geomagnetosphere, Størmer explored the theory of charged particle interactions with a dipole magnetic field. He showed that there are two dynamical regions in a dipole magnetic field, one that is unbounded and accepts charged particles from infinity, and another that is bounded and traps charged particles indefinitely, a *radiation belt* (Figure 2.1). The two regions have no overlap in the ideal Størmerian case (Van Allen 1983). Although Størmer was

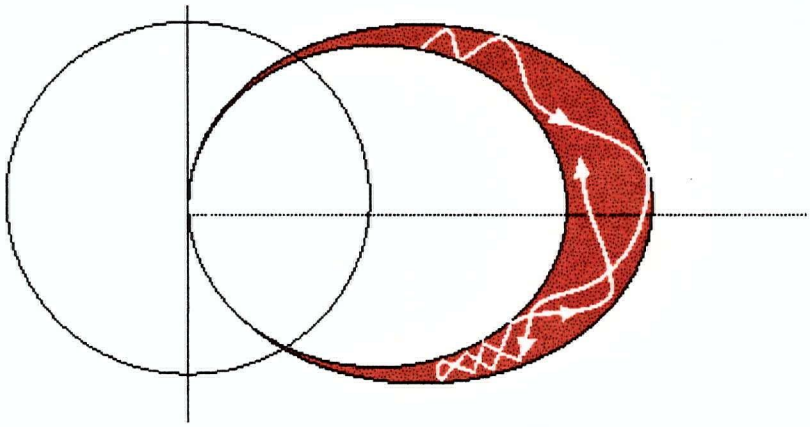

Figure 2.1 Meridian projection of a trapped charged particle (after Van Allen 1983).

unsuccessful in proving that the aurorae were indeed caused by trapped electrons or ions, these advances laid the theoretical framework for magnetospheric particle motion.

In the 1930's a group of researchers, including Arthur Compton, Robert Millikan, William Pickering, Willmot Hess, and others, collected ionisation chamber and Geiger counter measurements at various altitudes using balloon-borne instruments. The evidence showed that the radiation emanated from the Sun and had a particulate nature. In 1936 Hess was given the Nobel Prize for his discovery of 'galactic cosmic rays', which we now know to be particles as well.

Although the balloon-borne measurements showed increasing cosmic ray radiation up to 30 km, it was unclear how to extrapolate the results to even higher altitudes. It was this problem which inspired an early US Rocketry program to investigate high altitude phenomenon, paving the way for the first American artificial satellites to investigate geophysical parameters of the earth. The high-altitude measurements of very early satellites such as Explorer I and III led to the discovery of the "Van Allen" radiation belts of the Earth, much as Størmer had predicted (Van Allen 1959). Explorer discovered two radiation belts, and inner and an outer belt, separated by a *slot* region (Figure 2.2).

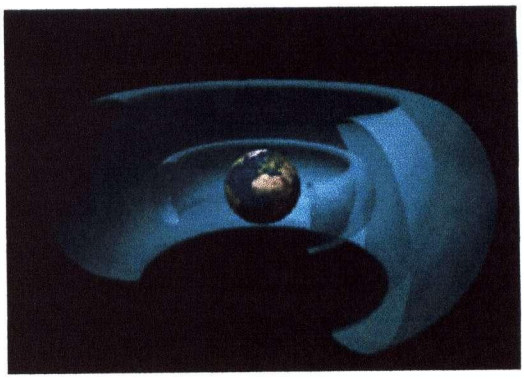

Figure 2.2 Artists conception of the Van Allen radiation belts. Inner and outer radiation belts are both shown.

2.2 Charged Particle Motion in a Magnetic Field

The fundamental motion of a charged particle in a magnetic field is described by the Lorentz equation:

$$\vec{F} = \frac{d\vec{p}}{dt} = q(\vec{v} \times \vec{B} + \vec{E}) \tag{2.1}$$

where F is the force on a charged particle due to a magnetic field, p is the momentum of the particle, q is the charge on the particle, v is the velocity of the particle, B is the magnetic field strength, and E is the electric field strength. The momentum p of a charged particle given by:

$$\vec{p} = m\vec{v} + q\vec{A} \tag{2.2}$$

where A is the vector potential of the magnetic field. For temporally uniform magnetic fields with simple geometry, the solution to equation (2.1) is easily integratable. However, for the magnetic field of the Earth, direct integration is not possible. Instead, the solution must be restricted to regions of space which have approximately uniform and simple magnetic fields where a direct solution is feasable. Models of the radiation environment are usually semi-empirical (i.e. they utilise a combination of theoretical interpretation with experimental data to make predictions).

Three basic motions describe the trajectory of a trapped charged particle (Figure 2.3). First, in the absence of electric fields, it is trivial to show the parallel velocity (i.e. velocity along magnetic field lines) is constant, and the magnitude of the perpendicular velocity is constant but with changing direction. Thus, the particle sweeps out a helical pathway around magnetic field lines with gyroradius ρ (radius of the circular component of motion) defined by equating the centripetal force to the magnetic force:

$$\rho = \frac{mv}{Bq} \tag{2.3}$$

Second, the particle will drift along magnetic field line until it reaches an area of higher magnetic field intensity where it is mirrored or 'bounced' in the opposite direction. And third, inhomogeneities in the Earth's magnetic field cause a slow westward drift of protons, and eastward drift of electrons (due to the opposite charge on each particle, the forces due to the inhomogeneities are in opposing directions). These three motions, discussed below in terms of *adiabatic invariants*, confine trapped particles to drift shells.

2.2.1 Adiabatic Invariants

In order to model charged particle motion around the Earth, three parameters are calculated which quantify the three different types of motion. In any mechanical system with periodic motion where the changes in the forces along the paths of motion are slow, it is possible to calculate values which remain constant over the path when integrated over chosen periodic orbits. These are known as *adiabatic invariants*. The three adiabatic invariants are found by integrating over one gyration orbit, one bounce period, and one periodic trajectory respectively.

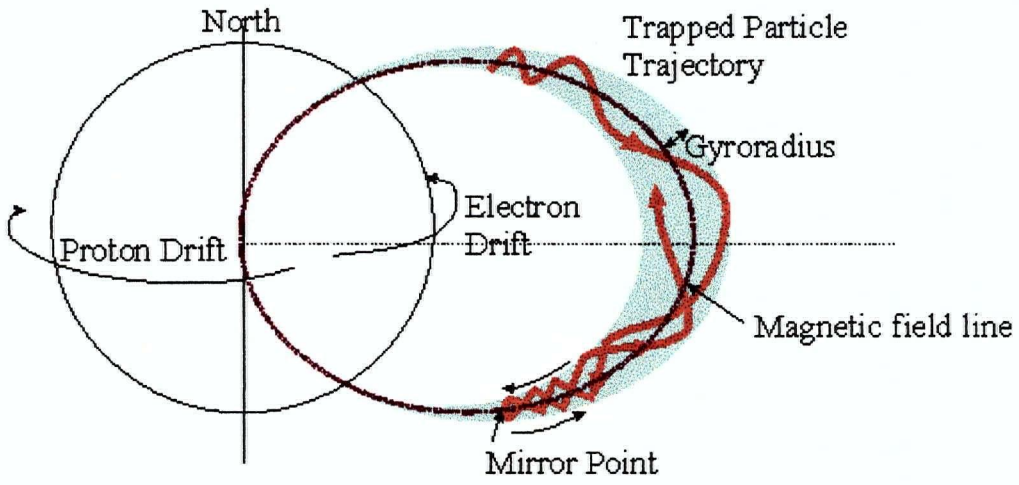

Figure 2.3 Schematic of charged particle motion in the geomagnetic field depicting the three motions of gyration, bouncing, and drift. (After Hess 1968)

The first adiabatic invariant is given by the following surface integral over the gyroperiod and along the helical particle trajectory:

$$J_1 = \oint (\vec{p} + q\vec{A})dl$$

$$= \frac{\pi p^2}{qB} \tag{2.4}$$

$$\propto \frac{p_\perp^2}{2mB} = \mu. \tag{2.5}$$

$p_\perp$ is the perpendicular component of the momentum vector. J_1, or μ, is called the magnetic moment, and determines the bounce motion of trapped particles in the models. The magnetic force on a charged particle is perpendicular to the field line direction. Thus, the magnetic force in a region of higher magnetic field strength serves to impart momentum to the particle perpendicular to the field (i.e., to $p_\perp$). Therefore, the particle's perpendicular momentum sqaured to magnetic field ratio is constant. However, in a quiescent field (a field that is temporally stable) total momentum is still conserved, so the parallel momentum of the particle drops to zero. The point where the parallel momentum is zero is defined as the mirror point (B_m), because the particle is then reflected out of the region of higher magnetic intensity and 'mirrors' its motion to the other magnetic pole. B_m for a particle at any point along its trajectory can be found by considering the pitch (α) of the particle.

$$\tan(\alpha) = \frac{v_\perp}{v_\parallel} \tag{2.6}$$

As the particle moves to higher magnetic intensity, the pitch of the particle will increase to 90°. Thus, B_m can be found if the pitch and magnetic field is known for any other point along the particle's path, and by using the first adiabatic invariant as follows:

$$\frac{p_\perp^2}{B} = \frac{p^2 \sin^2(\alpha)}{B} \propto J_1 \tag{2.7}$$

$$B_m = \frac{B}{\sin^2(\alpha)} \tag{2.8}$$

The first adiabatic invariant also relates to the gyroradius. Substituting equation (2.2) in (2.5) yields:

$$\rho = \frac{2m_o J_1}{qv_\perp} \tag{2.9}$$

Thus, stronger magnetic fields trap particles with a higher perpendicular momentum and smaller gyroradius.

The first adiabatic invariant introduces a second periodic motion of the particle, the bounce period (time it takes for the particle to go from a mirror point in the north to a mirron point in the south). By integrating over the bounce period and along *ds (*the surface defined by the field line) the second adiabatic invariant is found. It is equivalent to the integral of the parallel momentum over a field line between the two mirror points, $\pm B_m$, and defined by:

$$J_2 = \oint (\vec{p} + q\vec{A}) \cdot ds \tag{2.10}$$

$$= \int_{-B_m}^{B_m} p_\parallel \, ds. \tag{2.11}$$

The second adiabatic invariant, also called the integral invariant (I), defines drift shells in the assymetric geomagnetic field. As particles mirror back and forth, they can drift along lines of constant magnetic field strength, or drift in longitude in the direction specified by their charge.

When magnetic field strength increases with time (as in a geomagnetic storm), higher magnetic field strengths increase the momentum of the trapped particles. The mirror points rise to higher elevations in order to keep the integral invariant constant. Conversely, when the magnetic field strength decreases, the particles will mirror at points closer to the Earth, and may be removed from the radiation belts if the mirror point is low enough to include significant atmosphere.

The third adiabatic invariant J_3 is found by integrating over a third fundamental period of motion, the time it takes for the particle to drift around the earth in the drift shells defined by J_2. J_3 is given by:

$$J_3 = \oint (\vec{p} + q\vec{A}) dl$$
$$= q \oint \vec{B} \cdot d\vec{S} = q\Phi \qquad (2.12)$$

where *dl* is the the path along the drift shell, *dS* is an element of the surface enclosed by the drift path and Φ is the constant magnetic flux enclosed by the drift path. As long as the geomagnetosphere is stable, particles will return to the starting point of their drift path. This adiabatic invariant is not conserved during magnetic storms.

2.2.2 B and L coordinates

With such a complicated pattern of motion and so many degrees of freedom in the variables of the trapped particles (species, energy, pitch, altitude, latitude and longitude), it has proven advantageous to parameterize the species position.The most popular scheme is based on McIlwain's dipole shell parameter L (McIlwain 1961). L describes the position of the trapped particle in terms of the scalar magnetic field strength (B), and integral adiabatic invariant (I). If two particles have the same B and I values, they experience the same forces from the magnetic field and are constrained to the same drift shell about the earth. Hence, L is written as a function of B and I (equation 2.13) and describes the shells that particles are confined to by labelling each shell with a unique number.

$$L^3 = \frac{M}{B} F\left(\frac{I^3 B}{M}\right) \qquad (2.13)$$

The function *F* is approximated numerically for the complex magnetic field of the Earth (McIlwain 1961), and M is the dipole moment of the Earth's magnetic field (M = 8.06 x 10^{25} gauss cm^3). The position of a particle is derived explicitly by knowing both B and L for the particle.

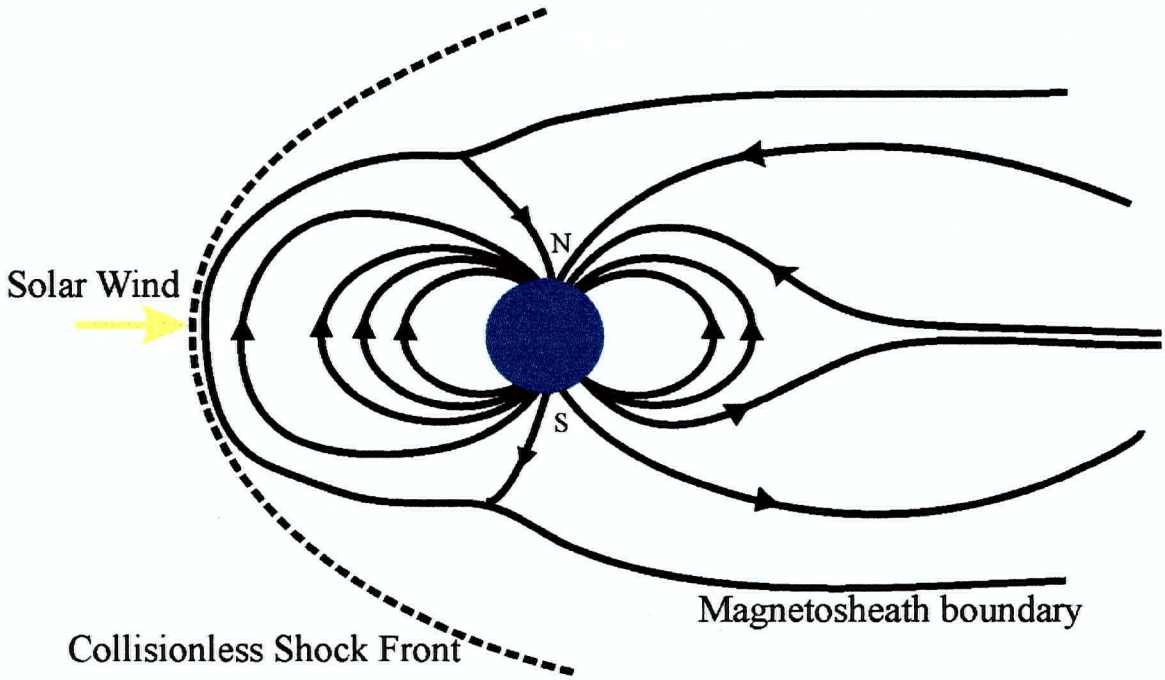

Figure 2.4 Schematic of the Earth's geomagnetosphere. (After Hess 1968)

2.3 The Geomagnetosphere

The boundary of the Earth's magnetosphere (called the *magnetopause*) is formed where the Earth's magnetic field meets and interacts with the solar wind (Figure 2.4). As the charged particles of the solar plasma bombard the Earth's magnetic field at the magnetopause, 99.9% of the particles are deflected around the Earth (Barth 1997). The leading edge of the Earth's magnetic field is compressed against the collisionless shock of the solar wind, and the streaming particles sweep the magnetic field lines of the Earth outwards from the sun, significantly distorting the magnetic field from the simple dipole configuration set by the geodynamo.

The outer magnetic field and transition region between the two areas has a complicated and dynamic structure due to external magnetic field interactions with the solar wind. Luckily, since the MOST microsatellite will be in LEO, it is not necessary in this work to face the challenge of choosing a model to represent the external field.

Within approximately 5 Earth radii, the magnetosphere is shielded from the upsetting effects of the solar wind and is much more stable. This inner region is dominated by the magnetic field originating from the core dynamo within the Earth. The

current field is most simply described by a dipole with magnetic moment offset from the rotational axis of the Earth by ~11^0, although the field is only quasi-dipolar (with about 10% of the field energy in higher order configurations). Field strengths range from a few nanoteslas (nT) at high altitudes to 50,000 nT at low altitudes and high latitude.

The Earth's inner magnetic field is neither spatially nor temporally stable. The field strength is decreasing at an approximate rate of 6% every 100 years, equivalent to 20 nT reduction in the magnetic moment per year (Barth 1997). This is a substantial change, but small compared to the instability of the outer magnetosphere where periodic geomagnetic storms upset the field lines on a much shorter time scale.

Since the inner magnetic field is non-static and changes in the field are currently unpredictable, static models are employed with updates released every 5 years by an International Association of Geomagnetism and Aeronomy (IAGA) working group to reflect changing conditions noted by experimental data (e.g., Mandea et al. 2000). The standard reference models are based on a spherical harmonic expansion of the geomagnetic potential in the form:

$$V = a\sum_{n=1}^{N}\sum_{m=0}^{n}(a/r)^{n+1}\left[g_n^m \cos(m\phi + h_n^m \sin(m\phi)\right]P_n^m \cos(\theta) \qquad (2.14)$$

where V is the geomagnetic potential, g_n^m and h_n^m are model coefficients, a is the mean radius of the earth (6371.2 km), r is the radial distance from the center of the Earth, ϕ is the east longitude, θ is the geocentric colatitude, and $P_n^m \cos(\theta)$ is the associated Legendre function of degree n and order m. The International Geomagnetic Reference Field (IGRF) model provides a set of coefficients g_n^m and h_n^m for experimental data based on a static magnetic field in a given epoch (Mandea et al. 2000). Thus, there now a set of 'definitive' reference fields (DRGF45, DRGF50, DRGF55, DRGF60, DRGF65, DRGF70, DRGF75, DRGF80, DRGF85) for which the data is definitive only in that no more can be collected because we can not travel back in time. Field models for the times between the reference epochs can be linearly interpolated from the existing data. Appendix B and Figure 3.3 shows the resulting B values for the MOST baseline orbit.

2.3.1 The South Atlantic Anomaly (SAA)

The offset of the magnetic dipole and the presence of higher order terms in the spherical harmonic representation of the magnetic field causes the Van Allen radiation belts to be asymmetric about the Earth (Figure 2.5). The belts extend to much lower altitudes over a large region centered on the South Pacific, called the South Atlantic Anomaly (SAA). The SAA is the most significant feature of radiation environment in LEO.

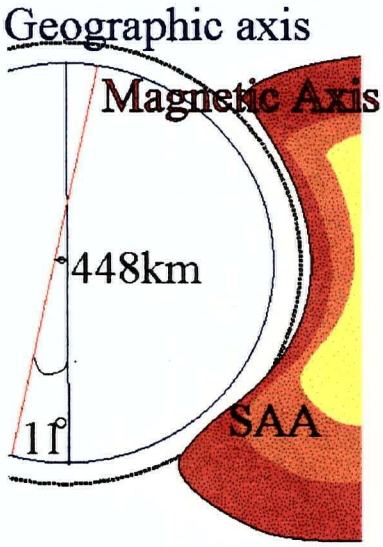

Figure 2.5 Schematic slice through the Earth showing the offset in magnetic axis and resulting South Atlantic Anomaly (SAA).

The SAA is a dip in the field strength of the Earth's magnetic field over the South Atlantic Ocean off of the coast of Brazil. This is due to the physical offset of the magnetic axis of the dipole moment of the Earth's axis from the geographic axis by 280 miles, as well as the inclination of the axis by ~11°. The magnetic field strength in the SAA drops to below 0.2 Gauss at 800 km, creating a natural funnel for trapped magnetospheric particles.

There has been a (primarily) northwestward 'drift' of the SAA (Dyer et al. 1999). The drift is due to secular decrease in the dipole term of the Earth's magnetic field (Lauriente et al. 1996). The drift is not a motion of the entire magnetic field as a whole, but a change in the location of the broad irregularly shaped centroid of minumum field intensity associated with the SAA, and varies with altitude (Table 2.1). However, the definitive boundaries of

Location	Year	Longitude of Centroid	Latitude of Centroid
Surface	1970	-26.2	-49.9
Surface	1993	-27.4	-54.1
1336 km	1970	-18.8	-45.1
1336 km	1993	-18.7	-50.1

Table 2.1 Location of centroid of minimum of SAA between 1970 and 1993 (Lauriente et al., 1996)

the SAA are known to be different than observed in the past as indicated by recent mappings of the SAA by satellite missions such as the Hubble Space Telescope (HST) and the Far- Ultraviolet Spectroscopic Explorer (FUSE) (Fullerton, private communication 2000).

2.3.2 Geomagnetospheric Shielding

The geomagnetosphere serves as a natural radiation shield for spacecraft in LEO. The degree to which the magnetosphere will be able to stop an incoming particle from entering the trapping regions of the magnetic field will depend on both the momentum and charge of the incoming particle, and its arrival direction. The degree of penetration of any given particle is described by the *magnetic rigidity* of the particle r, and the *cutoff rigidity* (or Störmer rigidity) of the magnetic field r_s.

In a dipole field, the magnetic rigidity (in gigavolts, or GV) is a property of the particle's energy E, atomic mass A (in amu), and charge z:

$$r = \frac{A}{z}\sqrt{E^2 + 2M_0E} \tag{2.15}$$

M_o is equal to 931 MeV. Intuitively, it is easy to see that if the particle's ratio of mass to charge is low, then it will be deflected more easily. Electrons have the lowest mass to charge ratio, followed by protons. Thus, for a given energy, heavy ions will penetrate the geomagnetic field the furthest, and electrons will be deflected the most. However, if the particle has sufficiently high energy it will still penetrate the shield as high energy particles have high magnetic rigidity.

Störmer described *cutoff* rigidity in his early work on the aurorae for a simple dipole magnetic field (Barth, 1997). Although the case is oversimplified, it is a good starting point. Using geomagnetic latitude λ, zenith angle ε, and azimuthal angle from the magnetic north pole ϕ to describe arrival direction of the particle, the cuttoff rigidity r_s (in GV) is given by:

$$r_s = \frac{M}{R^2}\left[\frac{\cos^4\lambda}{(1+\sqrt{1-\sin\varepsilon\sin\phi\cos^3\lambda})^2}\right] \tag{2.16}$$

where M is the magnetic dipole moment of the field, and R is the distance from the dipole center of the Earth in Earth radii. If the magnetic rigidity of the particle (equation 2.15) is less than the cutoff rigidity of the geomagnetic field, then the particle will be deflected away from the Earth. Again, intuitively it's clear that a stronger magnetic field will deflect more particles. Less obviously, equation (2.16) demonstrates the rigidity decreases with increasing geomagnetic latitude. It is for this reason that charged particles from large solar events are better able to penetrate into southern and northern geographic latitudes to cause the aurorae. In reality, the dipole approximation is not sufficient to calculate cutoff rigidities for the Earth's magnetic field, and more complicated models are used.

2.3.3 Geomagnetic Storms

The geomagnetosphere is non-static, with long term secular variations due to the geodynamo but much larger rapid variations due to the solar wind. Solar-modulated changes in the Earth's magnetic field are dubbed magnetic storms.

Solar wind variations are due primarily to solar flares and coronal mass ejections (CMEs). CMEs are large eruptions from the chromosphere of the sun that eject up to 1 billion metric tons of material at speeds averaging 400-700 km/s (Zirin 1988), but as high as 2000 km/s (Alpert 2000). They stem from an imbalance in magnetohydrostatic equilibrium in the sun, where magnetic field loops and arches become tangled in an increasing magnetic field background. The magnetic structures expand and act like pistons on the coronal plasma producing flows and shock waves (Stepanova & Kosovichev 2000). The shock front hits the magnetopause of the earth about 2 days later, dragging the magnetic field lines of the Earth and compressing the front end of the magnetosphere. In observations made by Lui et al. (2000), the magnetopause was compressed to within geostationary orbits.

While CME's increase the velocity of the solar wind, solar flares increase the density of the solar wind. Flares are created in the solar photosphere (interior to the chromosphere) during magnetic breaking (when magnetic field lines of the sun are twisted, break open, and re-connect in a lower energy configuration). The energy from magnetic breaking increases the energy of particles in the solar wind. While flares may

upset radio communications and are an important modulator to atmospheric drag, CMEs have a higher correlation with large geomagnetic disturbances. CMEs and flares occur simultaneously during the largest solar events.

The intensity of the geomagnetic storm depends on the orientation and strength of the CME. There were on average 0.9 CMEs per day during the 1974 solar maximum, and 0.74 per day during the subsequent solar minimum in 1980, but only as many as ~70% of these are associated with interplanetary shock fronts (Zirin 1988). The actual number of CMEs decreases as the solar cycle decreases, but the fraction of those creating interplanetary shock fronts reaches a maximum immediately following solar maximum (Lindsay et al. 1995). Fortunately, most of CMEs are directed into empty space and not towards Earth. The largest geomagnetic storms are from a direct, face-on impact of a CME (Lui 2000). Furthermore, since CMEs are made of charged particles and are not electrically neutral, each CME has a different magnetic orientation. If it is a southward orientation, then the magnetic field of the CME is more easily coupled to the magnetic field of the earth and a very large disturbance results (Barth, 1997). Thus, geomagnetic storms are very hard to predict. Even with early warning detections of CMEs by orbiting spacecraft, the intensity of the storm cannot be known in advance.

Satellites in geostationary or high-altitude orbits are most heavily influenced by geomagnetic storms. However, it is during such storms that particles are injected into the inner radiation belts. Thus, geomagnetic storms for a LEO are associated with a small increase in charged particle bombardment due to a decrease in cutoff rigidity (i.e., an increase in geomagnetic transmission function, section 3.1.3).

2.4 Charged Particle Populations

This description of charged particle motion has thus far neglected to consider in any detail the original sources of the charged particles. There are four populations of charged particles that can interact with a spacecraft: (a) residual magnetospheric trapped particles, (b) solar energetic particles (SEP), (c) Galactic cosmic rays (GCRs), and (d) an anomalous cosmic ray (ACR) component. The main properties distinguishing the populations are summarized in Table 2.2. The Sun turns out to be the most important factor, both as a source and as a modulator of these populations.

Properties of the Charged Particle Populations	(a) Magnetospheric Particles	(b) Solar Energetic Particles (CMEs)	(c) Galactic Cosmic Rays	(d) Anomalous Cosmic Rays
Energy Range	0.04 ~300 MeV (protons); .04 ~ 7 MeV (electrons)	varies, large events >430MeV	no limit, up to 100s GeV/n	up to 100 MeV/n
Composition	protons and electrons	dominated by protons, coronal abundance of heavy ions	83% protons, 13 % He ions, 3% electrons, and 1% heavier nuclei	enriched in elements with large 1st ionisation potential (H, N, O, Ne)
Charge state of heavy ions	N/A	Intermediately charged heavy ions	Fully charged heavy ions	Singly charged heavy ions
Solar Cycle Modulation	Protons increase during solar max, electrons decrease during solar max	Increase number of events during solar max, increase number of CMEs which cause geomagnetic storms in declining phase	Increase during solar max	Increase during solar max
Models	AP8/AE8	JPL91, CREME	CREME	CREME

Table 2.2 Comparison of trapped particle populations.

2.4.1 Magnetospheric Particles

The magnetospheric particles are considered as a separate population because of their long lifetime. Observations of a new proton belt formed in the wake of a very large solar flare in March 1991 showed that particles were trapped anywhere from 8 months to 2 years (Dyer et al. 1996). This discussion will concentrate on the dynamics of magnetospheric particles due to violation of adiabatic invariants (section 2.2.1), i.e., how particles can seep into and out of the radiation belts.

Without a source of replenishment, trapped charged particles in the radiation belts would eventually ionise molecular species in the upper atmosphere and be removed from the magnetic field of the earth. Conversely, without the sink of the upper atmosphere, trapped particle abundance would increase continually as charged particles from the solar wind gradually leak into the trapping regions of the field. Hence, the static flux of particles at a given energy represents an equilibrium between four competing processes: particle loss, infusion, acceleration (an increase in energy of the particle), and diffusion.

Trapped magnetospheric particles are infused into the radiation belts from the solar wind, Galactic cosmic radiation, and/or from cosmic ray albedo neutron decay (CRAND) (Gasser 1990). In the inner zone, CRAND turns out to be the dominant source of trapped particles. As cosmic rays hit the upper atmosphere, high-energy neutrons are produced. The neutron subsequently decays after a half-life of 630s into a proton and electron, which remain in the trapped in the radiation belts unless the particle trajectory and energy is such that they can be carried out of the magnetosphere. Trapped particles also diffuse from the outer magnetosphere into the inner trapping regions during periods of magnetic storms.

Particle acceleration is not a well-understood phenomenon. The reason that acceleration is cited as an important process in the distribution of magnetospheric particles is that an unstable radiation belt in between the inner and outer radiation belts was observed in 1991 by the CRRES satellite (Beaujean et al. 1996). Within this new radiation belt, electrons with energies exceeding 10 MeV and protons with energies exceeding 50 MeV were detected (Walt 1996). Some process must be responsible for accelerating the trapped particles to higher energies, probably linked to geomagnetic storms since a large CME impacted the Earth just prior to formation of the new radiation belts.

Diffusion is probably the most important of the four controlling processes as it is directly tied to the others. Trapped particle diffusion must be cast in a different form than the standard diffusion equation (e.g., gas diffusing down a column) because the particles have three normal motions (gyration, bounce, and drift). Instead, a Fokker-Planck prescription is adopted. In a Fokker-Planck derivation, diffusion is described in terms of the rate of change in co-ordinates of the particles (Walt 1994). It is useful because the

choice of co-ordinates is arbitrary. Choice of co-ordinates, in general, involves the adiabatic invariants as they reduce the dimensionality of the problem from six dimensions to three.

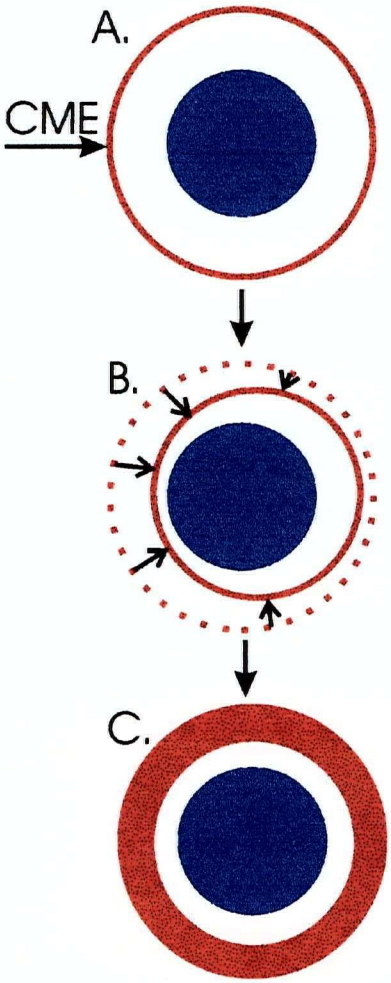

Figure 2.6 Schematic diagram of radial diffusion in response to a compressed magnetic field. A.) Shell of particles prior to impact with CME. B.) The dotted line represents the position of the old shell and the solid line represents the position after magnetic field compression. C.) Following magnetic relaxation, the particles spread in velocity into a more diffuse shell. (After Walt 1994)

Radial diffusion is particularly important in the inner radiation belts as it governs the transfer of particles from the outer zone to the inner zone. Since radial diffusion describes motion from one drift shell to another, it makes sense that it is related to fluctuations in the third adiabatic invariant ($J_3 = q\Phi$; equation 2.12) found by integrating over a drift period. In order for J_3 to be violated, changes in the magnetic field or electric potential fields must occur over time periods much more rapid than the drift period. Drift periods range from about 1 second to 1 day (Walt 1994), so this type of diffusion occurs in a variety of scales. The most common mechanism for violating the third invariant is a geomagnetic storm (see section 2.3.2). As an illustration of radial diffusion, consider a concentric shell of equatorial trapped particles in the Earth's magnetic field as shown in figure 2.6a. Now consider a CME shock front striking that shell of particles. The shock front compresses the magnetic field towards the earth, most noticeably along on the shock front itself. In response to this alteration of the magnetic field, particles move towards the Earth (Figure 2.6b), changing the value of Φ, and conserving the other two adiabatic invariants, μ and J_2. Once the CME has dissipated, the particles drift along constant μ, J_2, and Φ and gradually follow the relaxing magnetic field back to their original positions. This causes the

particles to spread into diffuse bands depicted in 2.6c. Although this scenario is highly idealized, the mechanism for transporting trapped particles into the inner trapping region is essentially the same.

Pitch angle diffusion also plays a major role in the transport of electrons out of the radiation belts. It is caused by the interaction of electrons with particles in the Earth's atmosphere, or by interactions with electromagnetic waves. The latter mechanism of loss is important only in the outer magnetosphere where interactions between the magnetosphere and the solar wind create high-energy electro-magnetic waves. However, in the inner magnetosphere, atmospheric particles frequently collide with trapped particles. Individual interactions with electrons do not significantly alter the path of the electron, but cumulative scattering with atmospheric particles causes a statistical change in the pitch angles. This random process can either send the electrons deeper into the atmosphere where they are essentially removed from the radiation belts, or to higher altitudes (Walt 1994).

Scattering is not applicable to protons or heavier ions because of their substantial mass. However, the atmosphere is still the primary sink for trapped protons. As high-energy protons traverse the atmosphere, inelastic nuclear collisions effectively reduce their energy and slow them down. A 100 MeV proton cools to about 100 keV after traversing 8.6 gm/cm^2, while a 1 MeV proton cools after only "seeing" 0.003 gm/cm^2 of oxygen. Below 100 keV, protons are lost in charge exchange reactions with atomic hydrogen (Hess 1968). This process is even more efficient at a lower mirror point or in the case of atmospheric inflation.

2.4.2 Solar Energetic Particles

CMEs were discussed in section 2.3.2 in the context of geomagnetic disturbances. But since a CME is a large mass of charged particles, solar energetic particles (SEP) are considered as a separate population within the radiation environment.

Until the mid-90's, SEPs were thought to originate from solar flares, as there is correlation between flare events and geomagnetic storms. Gosling (1993) dispels this notion as the 'solar flare' myth and points to CMEs as the real hazard in the radiation environment.

There are now two types of solar events described in the literature: *gradual* and *impulsive*, named for the duration of x-ray bursts associated with the events. The impulsive events are typically associated with solar flares and are accompanied by an increase in particle flux. Typically, the impulsive events have an enhancement in heavy ions, and are dominated by electrons. Their duration is on average a few hours long (Klecker 1996).

The gradual events are strongly associated with CMEs. The CME particle population is very similar to that of the solar coronal abundance, and is much more proton rich than the impulsive event (Klecker 1996). The events last several days. Since the CME events are also associated with geomagnetic disturbances, their effects are more severe than the impulsive events. Charged particles in the ejection can diffuse into the inner radiation belts during the period of the storm. Hence, even spacecraft in a LEO that are substantially shielded by the geomagnetosphere are susceptible to these larger events. Luckily, there are only about 10 per year during solar maximum (Barth 1997).

2.4.3 Galactic Cosmic Radiation

It was Galactic Cosmic Radiation (GCR) that Hess detected in his early balloon-borne experiments. It is definitely extraterrestrial in nature (as he originally proposed) and is now thought to emanate from outside the Solar System, though there is still considerable debate as to the source of the radiation (Cronin et al. 1997). Casting suspicion on an interplanetary source, GCR elemental abundance pattern is equal (to first order) to that found in the Solar System (Tribble et al. 1999). However, it has isotropic arrival directions, and thus, probably penetrates through all of interstellar space. Furthermore, the energy spectrum extends to very high energies (>100 GeV/nucleon) and it is hard to find a source to accelerate particles to such high energies within the Solar System. If GCR is indeed galactic, it must travel through ~7 g/cm^2 of interstellar space; thus, the heavy ion population in the GCR is thought to be fully ionized (c.f. Barth 1997).

The majority of experiments conducted to study the GCR are in "near-Earth interplanetary space", such as experiments flown on board the space shuttle (Badhwar 1996). For example, the University of Chicago's Cosmic Ray Telescope was flown on IMP-8 (in LEO) from 1976-1996 to provide complete coverage of the GCR spectra over

a full solar activity cycle. Voyager has also detected both GCR and ACR in its interplanetary travel (Reames 1999). In fact, a decrease in GCR with distance from the Sun is noted (Barth 1997).

The major difference between GCR and the solar wind is the energies of the particles; GCR has an extremely high upper energy limit. The energy range is tens of MeV/n to hundreds of GeV/nucleon. Hence, this component has high magnetic rigidity and penetrates deep into the magnetosphere. Cosmic rays detected by astronomers using ground-based telescopes are from the GCR population.

The total flux of GCR is significantly lower than magnetospheric particles. Still, GCR is an extremely important charged particle population because of the high energies of some of the ions, and because of their ease in depositing that energy into microelectronics and other sensitive onboard spacecraft components.

2.4.4 The Anomalous Component of Galactic Cosmic Radiation

The Anomalous Component of Radiation (ACR) also comes from outside our Solar System. However, its elemental composition and charge is different from GCR. All elements with a large first ionisation potential (H, N, O, Ne) show a marked increase in abundance over the GCR (Klecker, 1996). The charges on the heavy ions are also different from both GCR and the solar wind. ACR is singly ionised while GCR is fully charged and solar wind is intermediately charged.

Due to its properties, ACR is thought to be the result of recycling of GCR by the sun. GCR diffuses into the heliosphere in the Sun where it is singly ionised by UV radiation and interactions with charged solar winds. Then it is accelerated in the heliosphere or at the outer termination shock and released back into space.

This population has even higher magnetic rigidities than GCR due to its low charge to momentum ratio. Beaujean et al. (1996) have detected the ACR as low as L = 1.4 - 1.6 (about 400 km altitude at the equator) in the SAA.

2.5 Solar Cycle Modulation

Not one of the charged particle populations is unaffected by the influence of the solar cycle. Schwabe announced the discovery of a solar 'sunspot' cycle in 1849 when he noticed a gradual rise and fall in the number of sunspots over time, as is shown for data since 1750 in figure 2.7 (c.f. Zirin 1983). Sunspots are optically dark areas of the Sun associated with magnetic flux ropes entering and exiting the solar photosphere, and hence appear in pairs or groups. The polarity of each of the individual spots can be observed through the Zeeman effect (Hale made such observations in 1912). Each pair in a group of sunspots has opposing polarity (Zirin 1983). Continuous measurement of the polarity of the sunspots over the course of the noted 11 year cycle showed that consecutive cycles demonstrated a polarity reversal. Hence, the 11-year solar cycle is actually is sub-cycle of the sun's 22-year magnetic polarity reversal period.

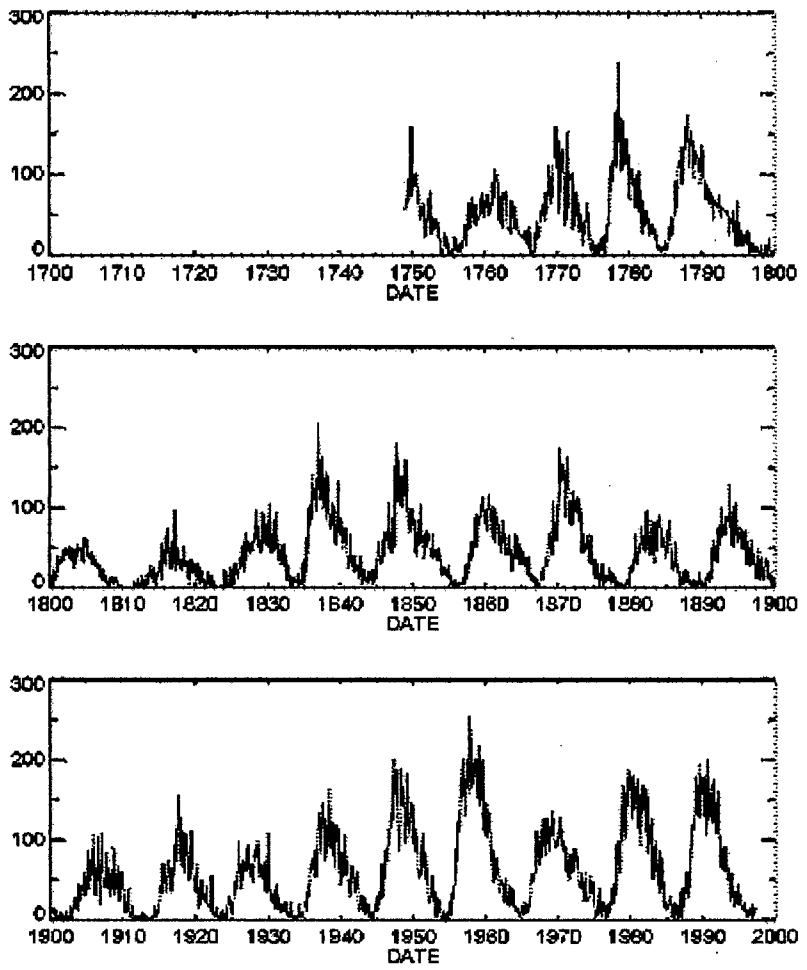

Figure 2.7 Sunspot number as a function of date, clearly showing an 11 year periodic solar activity cycle. (Plot is courtesy of David Hathaway, NASA MSFC)

Although the colloquial quoted solar activity period is 11 years, the actual duration of the cycles lasts anywhere from 9-13 years with an average of 11.5 years over the past 40 years (Barth 1997). Hence, the cycle is usually best described in terms of a 7 year maximum, interrupted by a 4-year minimum. The duration of solar maxima differs significantly from cycle to cycle and no means of predicting the duration has been found.

Solar cycle activity has opposite effects on electrons and protons. During solar maximum, the solar wind is denser and more particles ionise the Earth's ionosphere. This

leads to a slight, but noticeable expansion of the atmosphere (which creates greater atmospheric drag on orbiting satellites!). Thus, the loss of trapped protons through atmospheric collisions is increased during solar maximum. Peak proton fluxes occur 1 to 2 years following solar maximum and the degree of variation ranges from 5-50% between solar min and solar max depending on L value (Huston et al. 1998). While the loss of electrons from the inner belts also increases relative to solar minimum due to atmospheric expansion, the injection of electrons from the denser solar wind (specifically denser in electrons generated by flares) also occurs at a significantly higher rate. Thus, the trapped electron population increases during maximum solar activity.

Since the solar wind is stronger during solar maximum, GCR is deflected out of the Solar System more readily. Hence, solar maximum also sees a reduction in both the GCR and ACR populations. GCR is decreased by a factor of three at high latitudes due to solar modulation (Dyer 1999). The ACR population is reduced more, by a factor of 100 during solar minimum (Klecker 1996).

However, SEP flux increases. Solar maximum marks the peak number of impulsive and gradual events. There are up to 1000 impulsive events per year during solar maximum and only a few during solar minimum (Klecker 1996). There are only about 10 gradual events during solar maximum (usually in the declining phase) and there is no evidence for one occurring during solar minimum (although it might happen in the future). Since SEP events cause geomagnetic storms, geomagnetic activity highly coupled to the solar cycle.

Currently, the Sun is currently entering solar maximum. SOHO has seen an increase in CME events. Current sunspot number and predicted sunspot number for the next 7 years are shown in Figure 2.8.

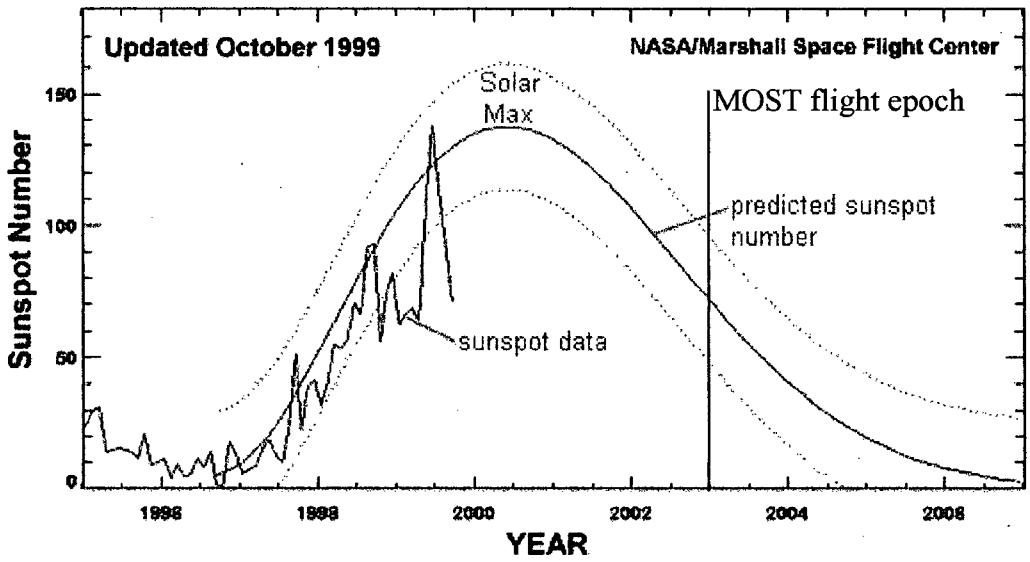

Figure 2.8 Recent sunspot data and the 'forecast' of the solar activity cycle for the next decade. (http://science.nasa.gov/newhome/headlines/ast14oct99_1.htm)

Chapter 3: Modeling the Radiation Environment

3.1 Approach

The standard approach to modeling the space radiation environment is outlined in Figure 3.1. This approach is recommended by the Radiation Physics Office (RPO), a division of the NASA Goddard Space Flight Center (GSFC) amongst others (http://radhome.gsfc.nasa.gov/radhome/rpo.htm, LaBel 1996). The first step is to determine the appropriate orbital parameters for the mission such that its scientific goals can be met. The orbital environment for the baseline parameters is evaluated using a suite of numerical programs, each designed to calculate a very specific component of the radiation environment or other environmental effect, based on the theoretical framework developed in Chapter 2. This chapter presents a description of the numerical models incorporated in SPACE RADIATION 4.00*. Chapter 4 presents the radiation environment of the MOST microsatellite and interpretation of the environmental effects on the MOST microsatellite design.

---

* SPACE RADIATION 4.00 provided courtesy of Alfred Ng, Canadian Space Agency

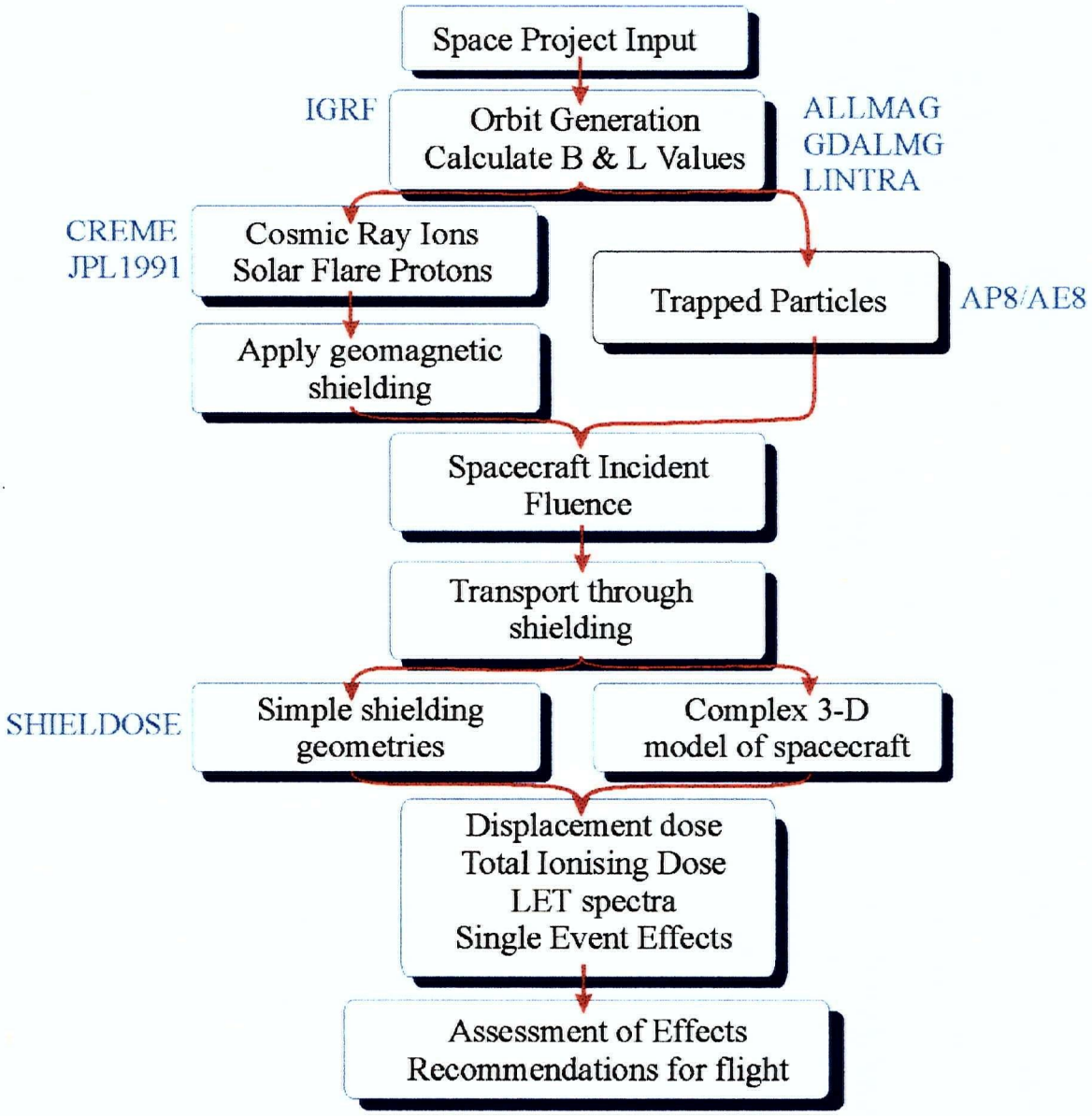

Figure 3.1 Schematic of approach to modeling radiation environment for the MOST microsatellite. Routines for specific calculations are indicated in light blue.

3.2 AP8/AE8 Trapped Particle Models

The most widely used models for evaluating the trapped particle environments are AE8 and AP8 for electrons and protons respectively. These models were developed by James Vette in a joint program sponsored by NASA and the US Air Force (USAF), and in co-operation with various university teams and corporations with data on the trapped particle radiation environment (Vette 1956). The first models (AE1 and AP1) were released in the early 60's, but included only data from solar minimum and thus were not practical for modeling the worst case environments a satellite would face*. The currently used versions of AE8 and AP8 (released in 1983 and 1976) incorporate data from 43 satellites and are applicable to both the maximum and minimum states of solar activity. In 1976, funding for further measurements was reduced so the models that spacecraft builders rely on today are based on data from 1958-1968 (Panasyuk 1996).

The models are empirical models for static conditions. Based on data from the above-mentioned period, the flux of particles of a given energy and L value are known everywhere along the geomagnetic equator. B and L values for a chosen magnetic field are extrapolated from the spherical expansion coefficients of the geomagnetic potential by a suite of three integrated programs developed by Al Vampola (Vampola 1996): ALLMAG, GDALMG, and LINTRA (Figure 3.3, Appendix B). The ratio of the geomagnetic field strength to that at the geomagnetic equator, B/B_o, is calculated for the orbital trajectory specified. Then, from the geomagnetic equatorial flux values, the geomagnetic flux values for trapped protons and electrons are interpolated into B/B_o and L space along the orbital trajectory, and integrated over mission lifetime to produce proton or electron fluence spectra.

In these models, the data from over 90 experiments was normalized to the 1976 standard in geomagnetospheric field models developed by Jensen and Cain (GSFC-12/66

---

* Intermediate stages of the models also include results from an artificially created electron belt from the Starfish program of high atmosphere nuclear weapon testing.

during solar maximum, and Jensen and Cain 1960 (JC60) for solar minimum) in order to calibrate the data. Thus, many authors suggest that more current reference magnetic field models should not be used with AE8 and AP8 (Heynderickx et al., 1996, Panasyuk, 1996, Barth 1997, Huston et al., 1998). This recommendation was explored by testing different field models for the MOST baseline orbit. Results are presented in Section 4.2. AP8 and AE8 also include positional information, parameterized in McIlwain's B and L values (McIlwain 1961).

3.3 Geomagnetic Shielding models

SPACE RADIATION calculates a geomagnetic transmission function based on the Störmerian ideal dipole theory (see Section 2.3). Numerical integration of particles along their trajectories in an IGRF gives isorigidity contours for the vertical cutoff, i.e. independent of azimuth and zenith angle (Shea and Smart, 1983). These results are extended to omnidirectional flux by assuming a Störmerian dipole field (Barth, 1997). The resulting function describes the fraction of particles which can penetrate the Earth's magnetic field, or the fraction of particles with magnetic rigidity exceeding the cutoff rigidity, as a function of cutoff rigidity for each point along the orbital trajectory. Also included in the calculation is the effect of the Earth's shadow. As particles stream from the sun towards the Earth, the dark side of the Earth is not only protected from the radiation by the Earth's magnetic field, but also by the Earth itself. Thus, the cutoff rigidity is asymmetric around the Earth if the Earth is considered as an obstacle. During a storm, the magnetic rigidty drops off. A larger fraction of low energy particles are transmitted through the geomagnetospheric shielding. High energy particles are attenuated by the same amount in both cases since the magnetic rigidity of a high energy particle is always greater than the cutoff rigidity.

3.4 CREME

Cosmic Ray Effects on Micro-Electronics (CREME) was developed by James Adams and others for the Nation Research Laboratories (NRL) in the United States and released in 1983 (Tylka et al. 1996). It was the first comprehensive numerical code to calculate heavier charged particle populations in the near-Earth environment and assess

their impact on spacecraft electronics. As it is integrated into the Space Radiation software, CREME is used to calculate the following charged particle spectra behind geomagnetic and spacecraft shielding:

(a) galactic cosmic ray population energy spectra;

(b) anomalous component energy spectra;

(c) and solar energetic particle events spectra.

Like AP8 and AE8, CREME is semi-empirical. It utilises measured differential flux values for different charged heavy species (H - Ni) and fits the measurements as a function of energy and a sinusoidal solar modulation parameter. The output is the integral or differential flux of particles inside the spacecraft at the sensitive electronic component being studied. The differential flux is the fraction of energetic particles in a given energy range (E+dE) divided by the energy bin size (dE). The integral of the differential flux yields the number of particles above a given energy (E), the integral flux.

CREME also evaluates ACR (the very penetrating singly ionised component). Since this component comes from the recycling through the sun, only elements with large first ionisation potentials (He, N, O, and Ne) are present in this type of radiation.

3.5 Solar Energetic Particles

CREME includes four models to describe large solar energetic particle (SEP) events stemming from CMEs. An alternate model, JPL 1991, was also employed in this study (Feynmann 1993).

The most energetic of the flare models are the 'Composite Worst Case Scenario' (CWCS) and the 1972 model which is modeled after observations of a very large Solar Energetic Particle (SEP) event which occurred in August of 1972 (AUG72). Since the high-energy channel (>60 MeV) observations of the 1972 event were unreliable due to an excessively high electron background associated with the event (Majewski et al., 1995), the composite worst case scenario has an added high-energy tail. At the time, this was done in order to create a 'worst case' SEP which had a 99% confidence level (CL) that the flux did not exceed a given value. Another very large flare event was observed in greater detail in October 1989, and did not show the high-energy tail of the CWCS, although

peak proton flux did exceed the 1972 peak proton flux by a factor of 2. Thus, the CWCS is not a useful worst-case scenario model.

The AUG72 event was actually a succession of 4 rapid CMEs of 'normal' character. It accounted for 84% of the proton fluence of high-energy particles that year (King 1974). This led to the early classification of 'anomalously large' events, and 'ordinary' events by King (1974). However, Feynman et al. (1990) reviewed solar event databases and concluded that there is an incredible range of energy spectra associated with CMEs, forming a continuum in energy from large to small. Thus, there is no such thing as a 'typical' SEP and spacecraft must be ready for the worst.

Tylka et al. (1997) suggest that the two most energetic events included with CREME are unrealistically severe. Indeed the high-energy tail of the CWCS is unrealistic in that only three flare events observed to date have its energy distribution. However, since a larger SEP than the AUG72 event was observed in 1989, it is appropriate to consider that event as the 'worst-case' model for the MOST microsatellite. No other worst case models are incorporated into Space Radiation 4.0.

The other three solar flare models are significantly more realistic; they are representative of average SEP events during solar max. The 90% worst case CREME model is a scaled down version of the August 1972 event, while the ordinary model is meant to reflect an average energy spectrum of many flares. The JPL model approaches SEP events with a slightly different perspective. Instead of isolating single events, the JPL model attempts to statistically predict the long term proton, Helium, and heavy ion doses for a given mission, within a given confidence level (Cl, or level of confidence that the solar proton flux will not exceed the model values) (Feynmann et al. 1993). The JPL 1991 model was used in this study as the standard, realistic solar proton model. Over the course of a 1-year mission, the CL for JPL91 is 97%. However, the other 4 solar proton models were also evaluated to allow for one large event during the MOST mission. The dose resulting from one large SEP event over one day exceeds the yearly doses resulting from using the JPL91 model.

3.6 Uncertainties

Due to a poor understanding of the solar activity cycle, and the limited predictive powers of large solar flares, CME's and hence, geomagnetic events, evaluating the uncertainty in the above models is challenging. Until accurate predictions are made as to the timing, severity, and duration of large solar events, the accuracy of the individual models will be orders of magnitude better than the accuracy in predicting the number of large SEP events a satellite will face. Hence, the spacecraft designer is forced to take a pessimistic view, consider the 'worst-case' scenario, and ensure that the satellite can withstand it (and then cross her fingers that it won't actually happen!).

However, the existing models have been in use for a sufficient amount of time to compare predicted dose to measured dose. Gussenhoven and Mullen (1993) indicate 'good' agreement between the AP8/AE8 models and orbit to orbit doses as measured by the Combined Release and Radiation Effects Satellite (CRRES). However, they note that predicted flux of high-energy electrons (1-5MeV) from AE8 can be up to 2 orders of magnitude too high.

On the other hand, comparisons made by Huston et al. (1998) with data from the TIROS/NOAA low altitude polar orbiting spacecraft indicate that AP8MIN and AP8MAX *under-predict* the dose experience by a factor of 1.7-2.0 consistently over 2 solar cycles.

Favorable agreement between AP8MIN and data on board the Advanced Photovoltaic and Electronics Experiment Spacecraft (APEX) (in a highly eccentric 70° inclination orbit) as well as with results flown on board PoSAT-1 (in a sun-synchronous polar orbit very similar to the MOST baseline orbit) has been found (Watson et al 1998).The predictions from AP8MIN over-predict the APEX dose rates by 10%, The primary factor in the disagreement between the models and the observed doses is most likely an overestimation of low energy protons. However, the models under-predict the dose rates with PoSAT, the lower altitude satellite, by 40% (Dyer et al. 1998). Thus, though the colloquial statement regarding the uncertainty in the AP8 models is that they over-predict the environment, in the low altitude MOST baseline orbit (Section 4.1), they most likely under-predict the actual environment by a factor of about 2.

According to the authors of the CREME code, the uncertainty in the CREME spectra ranges from 2-5 depending on the energy per nucleon (c.f. Badhwar and O'Neill 1996). Recent comparisons of CREME with newer experimental data and exercises associated with the development of a new version of CREME (CREME96) have shown that the errors in the original model are on the order of 40%. The errors arise mainly from the assumption that the solar activity cycle is sinusoidal (Tylka et al. 1997). The solar polarity reversal is not a sinusoid, and so current models (CREME96) have incorporated a more realistic solar modulation factor developed by Nymmik (1996). Comparison with UoSAT-3 which also was flown in the same orbit as the MOST baseline orbit shows that CREME fails to predict an elevated level of high latitude cosmic rays during solar minimum (Dyer et al. 1999). Since MOST is scheduled to launch during an active solar phase when this elevation in cosmic rays is not an observed phenomenon, CREME is satisfactory for modeling the MOST radiation environment.

The Solar Anomalous and Magnetospheric Particle Explorer (SAMPEX) satellite has brought to light an overestimation in the CREME predictions of the ACR (Tylka et al, 1997). The actual spectra drop off much more rapidly at the higher energy end than predicted by the models. So even though the singly ionised particles are more penetrating than their higher charged counterparts, they have relatively low energies and are therefore more easily attenuated by shielding. Tylka estimates that no particle from the ACR will penetrate 50 mils of Al shielding. The update to CREME goes as far as to exclude the ACR as having any effect on microelectronics. Indeed, the flux presented by ACR in Chapter 4 is an order of magnitude less than the GCR flux and thus, even though the model is a known overestimation, the uncertainty associated with it is negligible compared to the uncertainty in the trapped proton and electron models.

Since the primary component of radiation in the MOST baseline orbit is made up of trapped protons and electrons in the SAA, the updated version of CREME was not employed in this study. Although CREME96 is more accurate than its predecessor CREME, it is not integrated into Space Radiation 4.0. Since the accuracy differences are negligible compared to the uncertainties in the primary particle population, it was not considered necessary to evaluate the GCR or ACR with greater accuracy than that afforded by CREME.

Chapter 4: Choosing a Baseline Orbit

As outlined in Figure 3.1, the spacecraft engineer must supply a baseline orbit to be evaluated in a radiation analysis. Choosing a baseline orbit can be complicated as a number of factors not related to the radiation environment arise. This Chapter investigates some effects the MOST microsatellite will face in the baseline orbit established in the first phase of mission design.

4.1 The MOST Baseline Orbit

MOST is best suited to a low-Earth orbit (LEO) where the radiation environment is not harsh, such as a low altitude geo-synchronous orbit, or a polar orbit. The MOST science team chose a polar sun-synchronous orbit with an 800 km altitude because (a) it allows stars to remain in sight of the telescope for an extended period of time (Section 4.3), (b) minimises scattered light contributions (Section 4.6), and (c) it is the baseline orbit for Radarsat 2 (satellites hitching a ride to space can't be too picky about where they end up). The Local Time of Ascending Node (LTAN) for the baseline orbit is 6:00 p.m., so that the satellite always remains above the terminator of the Earth. This type of dawn-dusk orbit described further in Section 4.5 is also favored by Earth monitoring missions as it provides good relief in images. The advantage for MOST is that it significantly reduces scattered light as a photometric noise source.

One side of the satellite will remain pointed in the general direction of the sun, constantly shielding the other side of the satellite, while the telescope will stay pointed at a fixed spot in the sky in the opposite direction of the sun. Over the course of a year, the beam the telescope views on the sky sweeps out 360° in Right Ascension, so the continuous viewing zone (CVZ) for the satellite is a strip along the celestial equator. The ground tracks span the whole Earth, so there is sufficient communication time with planned ground stations in Vancouver and Toronto (Canada) and Vienna (Austria). However, the satellite will graze the Van Allen radiation belts in the SAA during 18% of the orbital passes.

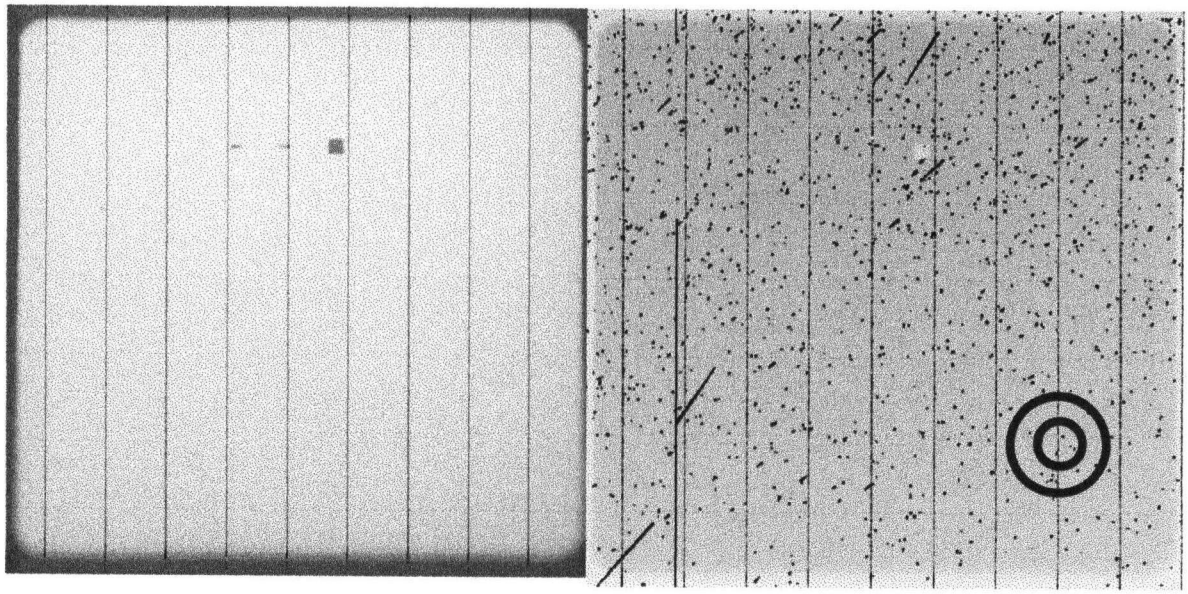

Figure 4.1 Data from the FUSE guide camera comparing regions (a) outside the SAA, and (b) inside the SAA. Over-plotted is the MOST 'donut' shaped pupil image drawn to scale. Each pixel that is dark in the second frame is a lit pixel, and the lines are tracks where charged particles have hit with a high grazing angle and thus penetrated across many pixels in the direction of their path through the device. (Courtesy of Tim Hardy, DAO.)

4.2 Cosmic Ray hits

Although also caused by high-energy particles in LEO, cosmic ray hits do not permanently damage any onboard space components. When an energetic charged particle from any of the four populations of particles described in Section 2.4 hits the CCD, it can ionise one of the Si atoms, releasing an electron and leaving an electron hole pair. The electrons are collected by the electric fields of the device and incorporated as signal. Thus, pixels hit by an incoming particle become "lit" with abnormally high signal compared to the background signal. The Far Ultra-Violet Spectroscopic Explorer (FUSE) is orbiting the Earth currently, sending data taken from both inside the SAA and from the quiescent regions outside the SAA. Figure 4.1, two data frames from the FUSE Fine Error Sensor (FES) which uses a CCD detector, illustrates the number of lit pixels due to crossing the SAA.

The spurious signals created by cosmic ray hits inside the SAA will be treated during data reduction. The majority of the radiation flux is centralised in the SAA, but charged particles will still hit the detector outside this region at a much lower rate. Thus,

the data reduction scheme employed by MOST must consider removing 'lit' pixels due to cosmic ray hits, or tolerating them. There are two options for cosmic ray removal, both employed by ground based astronomers:

(a) remove the pixel completely from the data set, or

b) assign a value to the lit pixel that is an average of the surrounding pixels.

Since cosmic ray hits occur over a very short time scale, they can be unambiguously detected if the signal from a lit pixel is high one integration, and then a reasonable value in the next sequential integration.

4.3 The Continuous Viewing Zone (CVZ)

The MOST orbit is designed such that the optical axis of the telescope is steerable within a cone centered in the anti-solar direction with a diameter of 27.3° (set by the orbit, Figure 4.2). As the Earth revolves around the sun, this projection will sweep out a path along the sky, much like the searchlight of a lighthouse beam. As the beam sweeps across the sky, the microsatellite will point at stellar targets which fall inside its area. Depending on the location of the star inside the CVZ, if it transverses the CVZ at a higher point than at the equator of the projection, it will have a shorter dwell time in the CVZ. For example, Procyon is visible in the CVZ for 7.9 weeks, whereas Gam Leo A is only visible for 4.2 weeks. See Appendix C for the dwell time of the MOST primary targets as a function of orbital parameters.

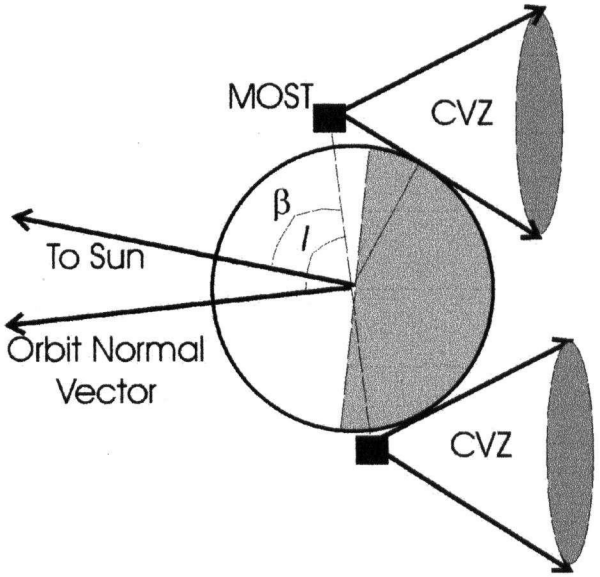

Figure 4.2 Schematic of the MOST baseline orbit showing Continuous Viewing Zone (CVZ), Orbit Normal Vector (ONV), Inclination angle (*I*), and Beta Angle (β).

The diameter of the CVZ is a function of orbital inclination and altitude. If MOST is put into a higher altitude orbit, the diameter of the CVZ will increase as the limiting

boundary of the cone created by the limb of the Earth is at a larger angle. Figure 4.3 shows the MOST targets on the sky with the limits of the MOST CVZ for different inclinations also projected. A higher inclination, higher altitude orbit favours more targets.

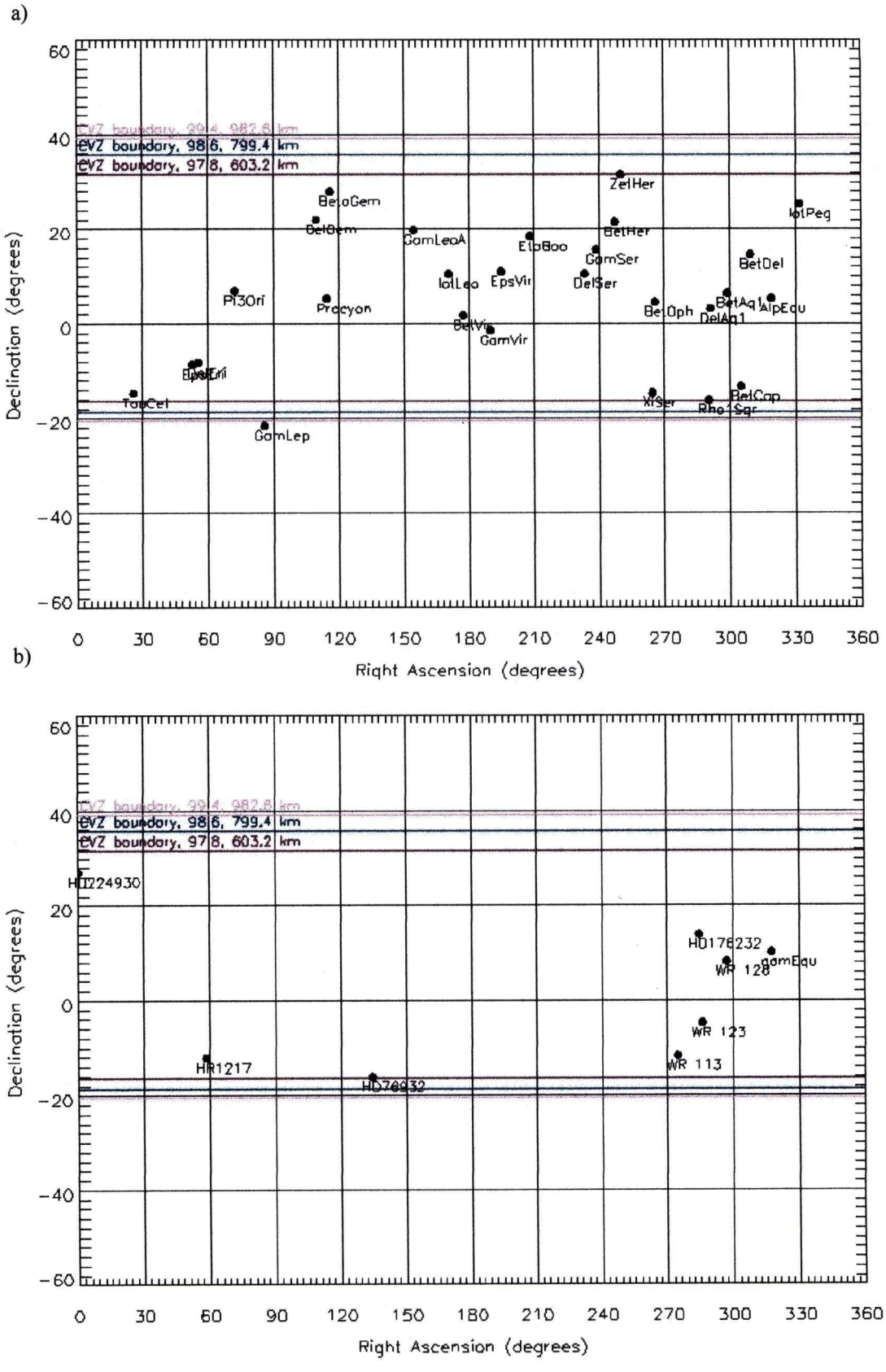

Figure 4.3 MOST targets and limits of CVZ as a function of orbital inclination/altitude projected on the sky for a) the expanded MOST solar type targets, and b) other targets.

4.4 The MOST Duty Cycle

The duty cycle is defined as the amount of time that a telescope can continually stare at a stellar object. In order to perform asteroseismology successfully, a very high duty cycle is essential. In fact, a limited duty cycle is one of the strong limitations of performing asteroseismology from the ground. Consortiums have formed in an attempt to network telescopes all over the Earth into a simultaneous observing campaign called the Whole Earth Telescope, WET.

The CVZ is designed to allow objects to fall into the boresights of the MOST microsatellite for an extended, *uninterrupted* period of time. In asteroseismic data analysis, Fourier time sequence analysis is performed. It is a powerful method of detecting regularities in the signal from the star. However, it is also a very powerful way of detecting anything else in the data set which has a repetitive pattern, such as regular gaps of data. In a perfect world, where the photometric time series is complete, the Fourier analysis of a single frequency would return the single frequency alone. However, for a reduction of the duty cycle of 10%, side-lobes to the primary signal are created, as illustrated by Figure 4.4. These side lobes are aliases or ghost signals of the primary frequency. For comparison, the spectral window from a single-ground based sight is also presented. It is clear that the signal due to an oscillating star is a challenge to extract from a ground based data set.

While MOST passes through the SAA, the number of cosmic ray hits and proton induced SEEs will be high, and possibly too high to allow one to utilise data taken during the passage. Thus, there may be small gaps in the MOST data set corresponding to times when MOST is in the SAA. In a worst-case scenario with no shielding at all, MOST would loose data from the immediate boundaries of the SAA. Thus, the duty cycle would be about 82% complete (that is, MOST would lose 18% of its data due to the SAA). More realistically, MOST will still be able to take good data throughout the SAA where particle flux is relatively low. Since the pupil image for the science data set only ~6400 pixels, the actual number of lit pixels expected in the science data in the densest part of the SAA is not expected to be significant. The limiting factor to accumulating data through the SAA may be the attitude control system (ACS) performance, although with appropriate thresholding, the algorithm for guiding should be sufficient to allow guiding

through the SAA. Thus, a 90% duty cycle is the minimum expected. Simulations of the photometric performance of MOST with an 80% duty cycle by Kuschnig have shown that the photometric precision requirements can still be met (Kuschnig et al. 1999).

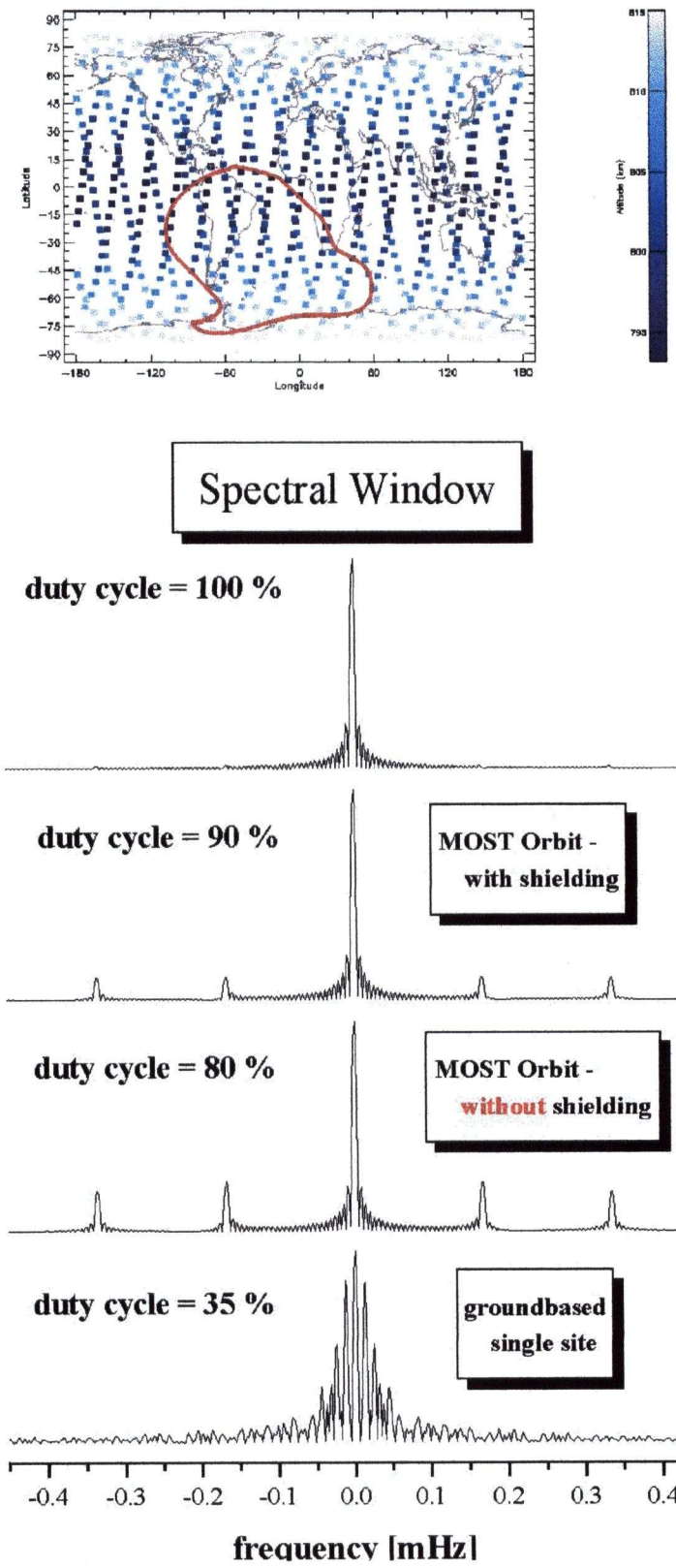

Figure 4.4 The spectral window for the MOST microsatellite, based on the approximate SAA location shown in the top inset. (a) shows an ideal spectral window for a complete data set, (b) for a duty cycle with a loss of 10% in completeness due to passages through the SAA, (c) for a duty cycle 20% incomplete, and (d) for a typical ground based sight that can only observe during the night (Courtesy of Kuschnig, 2000).

4.5 Eclipse Season

The baseline orbit has a Local Time of Ascending Node (LTAN, the time at which the satellite crosses from the Southern Hemisphere of the Earth to the Northern) of 6 p.m. Thus, the satellite will always remain above the terminator of the Earth (where the sunlit portion of the Earth meets the dark portion) (Figure 4.2). MOST will peer out over the dark limb of the Earth for the majority of the orbit. This is equivalent to an orbit with LTAN of 6 a.m., except the satellite crosses from the Southern to Northern hemisphere at dawn as opposed to dusk. Thus, these orbits are referred to as dawn-dusk orbits.

During winter and summer eclipse seasons when the Sun is at its most extreme inclination relative to the Earth's equator, the plane of MOST's orbit will be the furthest from the terminator (whether it is in a dawn or a dusk orbit). For a maximum of 17 minutes (17% of the orbit, including umbral and penumbral portions of the eclipse) at the summer solstice MOST will be eclipsed by the Earth, cutting off direct power supply from MOST's solar arrays and forcing the satellite to rely on its batteries. Additionally, many satellites are very sensitive to temperature gradients. As they are shadowed from the sun and the temperature drops, they may experience "thermal snap", a flexure of the mechanical structure. Since MOST is so small, thermal flexure should not be significant. However, the attitude control system will be more sensitive to this phenomenon as optical focus may become slightly distorted.

Figure 4.5 shows the duration of individual eclipses for the MOST baseline orbit from October 2001 through January 2004. Since power is reduced, MOST may not be able to function in normal operating mode. Eclipse season would be most appropriately spent performing testing and engineering operations.

Lunar eclipses, also shown in Figure 4.5 have moderate to long duration. However, since there is not very many consecutive eclipses (repeated over many orbits) relative to the number of consecutive eclipses during the eclipse season, power levels should not be significantly affected.

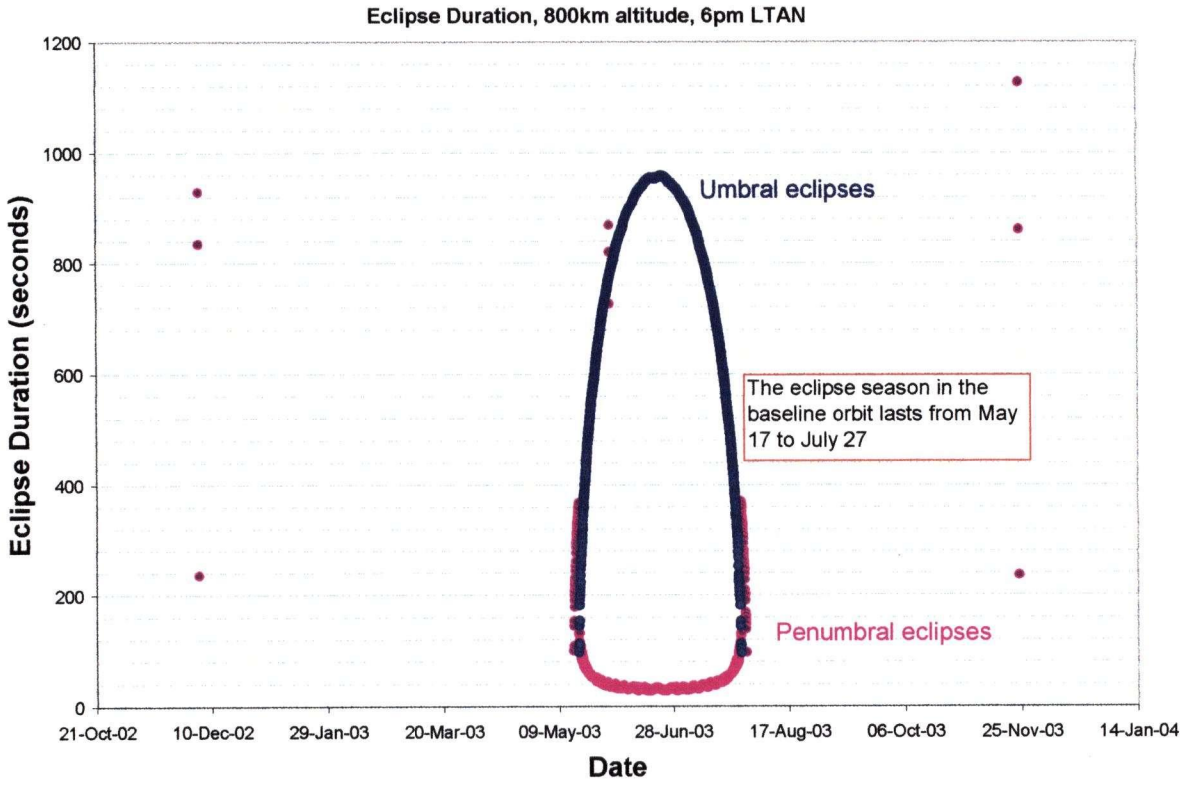

Figure 4.5 Eclipse duration for the MOST baseline orbit. The central, darkest region of the eclipse is the umbra, while the penumbra is the less shadowed outer portion of the eclipse. Eclipses outside the eclipse season are caused by the moon's shadow.

The LTAN of the orbit determines when the eclipse season will occur. As shown in Figure 4.5, for a LTAN of 6 p.m., the eclipse season is centered on the summer solstice. For a LTAN of 6 am, the eclipse season is offset by 6 months to be centered around the winter solstice. A noon/midnight orbit would have its eclipse season at the vernal or spring equinox.

4.6 Stray Light Effects

At the opposite point of the orbit where MOST is eclipsed from the Sun by the Earth, MOST will be forced to peer out over the sunlit limb of the Earth and scattered light signal will increase.

Experience from the star-sensor aboard the failed WIRE mission, also in a polar sun-synchronous orbit (inclination 97°, altitude 470 x 540 km), shows that the contribution of signal from peering over the bright limb of the Earth is substantial. Figure 4.6 shows a brief sequence of data taken by WIRE with a gap due to occultation by the Earth. The increase in integrated signal immediately before the occultation corresponds directly to the time when the star-sensor observes over the sun-lit limb of the Earth. Data processing procedures used by Busazi in an attempt to detect oscillations in the Altair

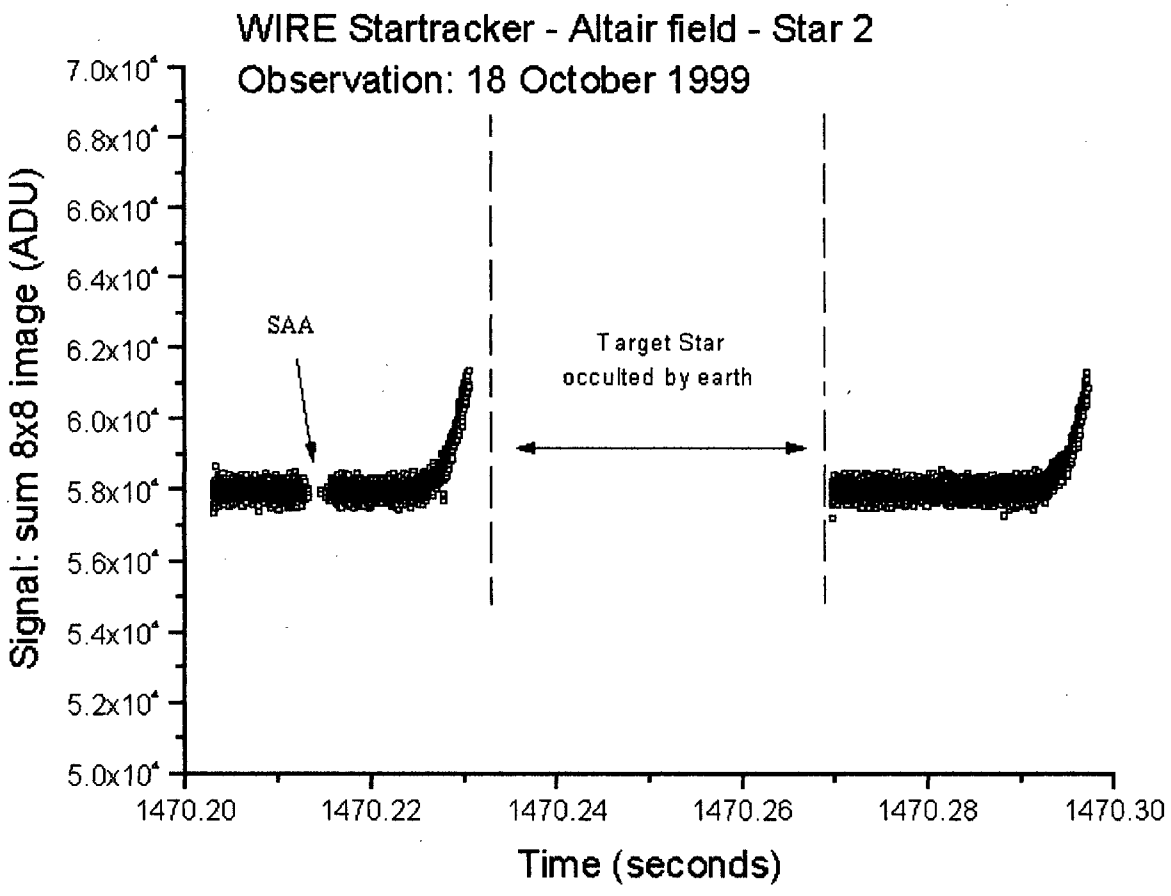

Figure 4.6 Light curve taken by the star-sensor onboard the WIRE satellite showing a dramatic increase in signal prior to occultation by the Earth when the satellite peers out over the bright limb of the Earth. (Figure courtesy of Kuschnig, Data courtesy of Busazi.)

light curve discards any data taken prior to an occultation (Kuschnig, personal communication).

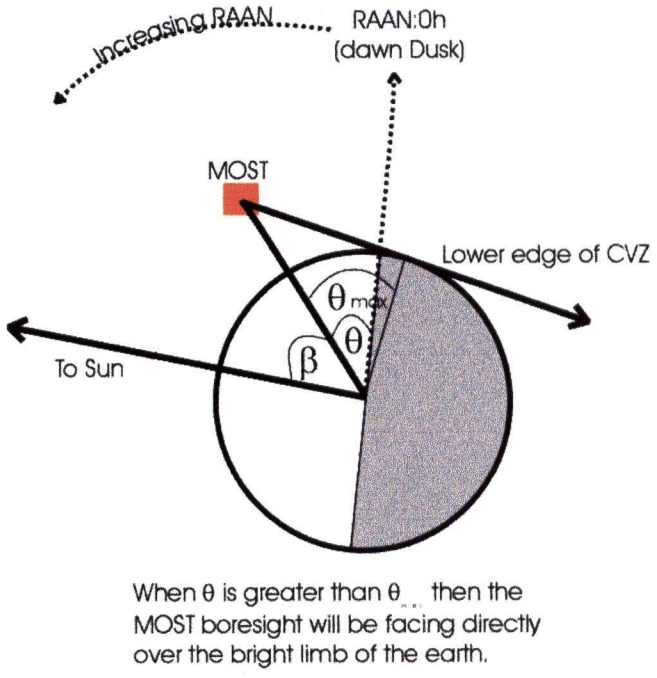

Figure 4.7 Schematic of MOST orbiting the Earth viewed looking down on the North Pole. Changing the LTAN of the orbit causes MOST to peer out over the sunlit limb of the Earth, increasing photometric noise due to scattered light. Note that Right Ascension of Ascending Node (RAAN) is the same as LTAN measured in degrees of right ascension as opposed to local time.

Orbits with varying LTANs have been considered, especially since not every satellite makes it into their optimum orbit upon launch. Increasing the LTAN from dawn/dusk to noon/midnight causes the satellite orbit the Earth along a fixed plane relative to the Earth separated by a larger angle θ from the plane of the terminator (Figure 4.7). In orbits with LTAN approaching noon or midnight, the photometric noise due to scattered light from the Earth increases dramatically. A complicating factor in estimating the amount of scattered light from the limb of the Earth is the albedo of the Earth is not constant. Hence, MOST should be in an orbit where θ is less than θ_{max} (the angle between the intersection point of the lower most bore-sight of the CVZ and the orbital plane) in order to reduce scattered light contributions. Granted, many of MOST's targets do not fall directly along this lower bore-sight (Figure 4.3). But since sunlight is directed outwards and will reflect off the atmosphere or interplanetary particles back towards the telescope, a conservative observation would only be made in the upper half of the CVZ for such an orbit.

Figure 4.8 shows θ for three differing orbits, from the baseline dawn-dusk orbit through to an orbit with LTAN 7 p.m.. 8 p.m., and LTAN 9 p.m. Even for a dawn-dusk orbit, θ exceeds θ_{max} in the summer season (eclipse season). The amount of time during

the year that the satellite will stare out over a sunlit limb of the earth is very sensitive to the LTAN. If the LTAN is later than 8 p.m. (or conversely earlier than 4 p.m.) then the satellite will always stare out over the bright portion of the earth. In all non dawn-dusk orbits, MOST will need greater power supplies than are currently budgeted. Thus, it is imperative that MOST go into a dawn-dusk polar orbit (LTAN either 6 a.m. or 6 p.m.).

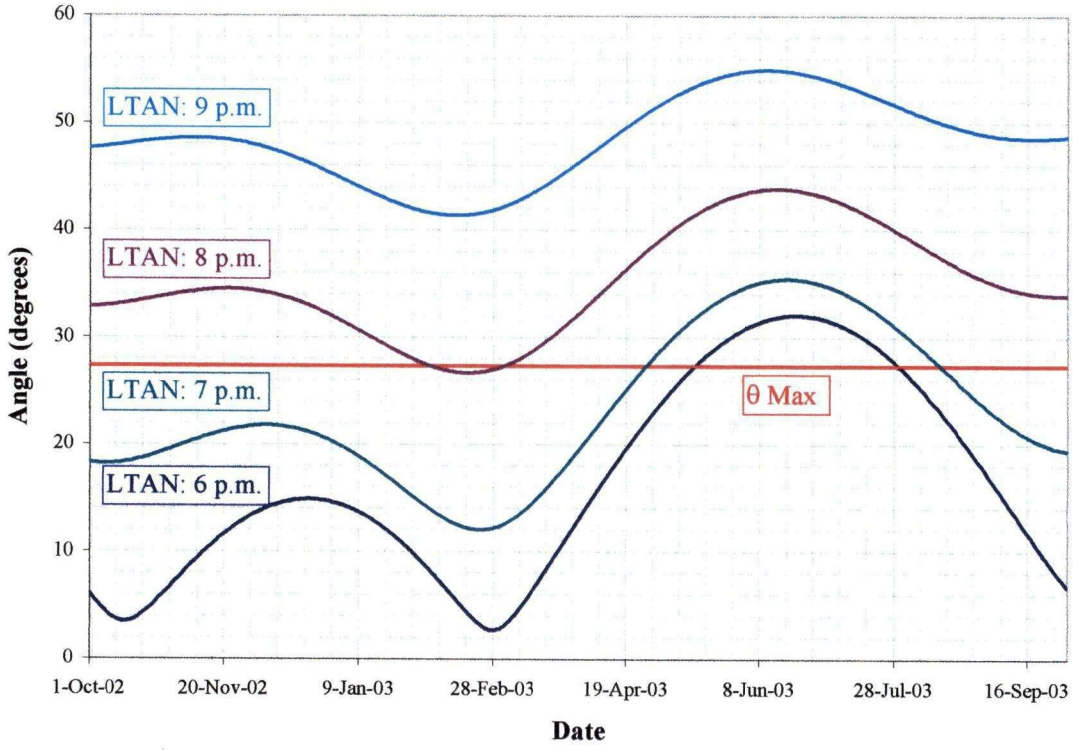

Figure 4.8 θ as a function of LTAN over the course of a year for the MOST baseline orbit (800 km). The amount of time that θ exceeds θ_{max} increases greatly as the orbit deviates from a dawn dusk orbit.

Heliosynchronous orbits are stable over a range of altitudes where the inclination of a heliosynchronous orbit is a function of the altitude (See Appendix B for inclination vs. altitude of heliosynchronous orbits). θ is not strongly dependent on altitude of the orbit since inclination only changes slightly as a function of altitude. However, θ_{max} does change significantly with altitude (θ_{max} is 23.93°, 27.31°, and 30.18° at 600 km, 800 km, and 1000 km respectively). Figure 4.9 shows the maximum allowable value of the LTAN (defined as $\theta > \theta_{max}$) for a 600 km, 800 km, and 1000 km sun-synchronous orbit on

January 1, 2002. Since θ changes with the seasons, these maximum allowable LTANs will be closer to noon/midnight over spring and fall equinoxes and dawn/dusk during winter and summer solstices. As per Figure 4.9, even in a dawn-dusk orbit, there is a season in which θ exceeds θ_{max}.

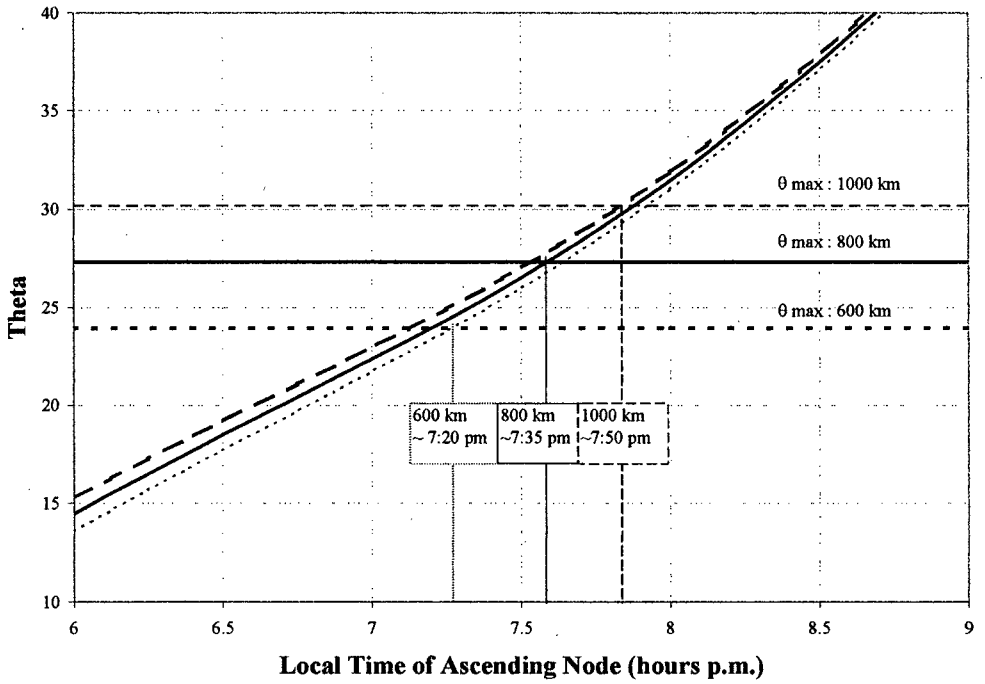

Figure 4.9 Maximum allowable values of the LTAN for heliosynchronous orbits with 600 (short dash) 800 (solid), and 1000 km (long dash) altitude on January 1, 2002.

Chapter 5: The Weather Forecast for the MOST microsatellite

Now that a baseline orbit is established and it is clear that the orbital environment outside of the radiation environment is tolerable within MOST mission parameters, it is essential to determine the radiation environment of the orbit to ensure the satellite design can tolerate its impact. This chapter outlines the steps used to establish the radiation environment for the MOST microsatellite based on the approach detailed in Chapter 3.

5.1 The geomagnetic field

As per Figure 3.1, the next step in evaluating the radiation environment of the MOST microsatellite is to calculate the geomagnetic field (Section 3.1.2) to be used in AP8 and AE8. Figure 5.1 shows geomagnetic field strength for the MOST microsatellite baseline orbit based on the IGRF2000 field extrapolated to a flight epoch of 2002.

Due to the suggestion that only the Jensen and Cain models should be used with

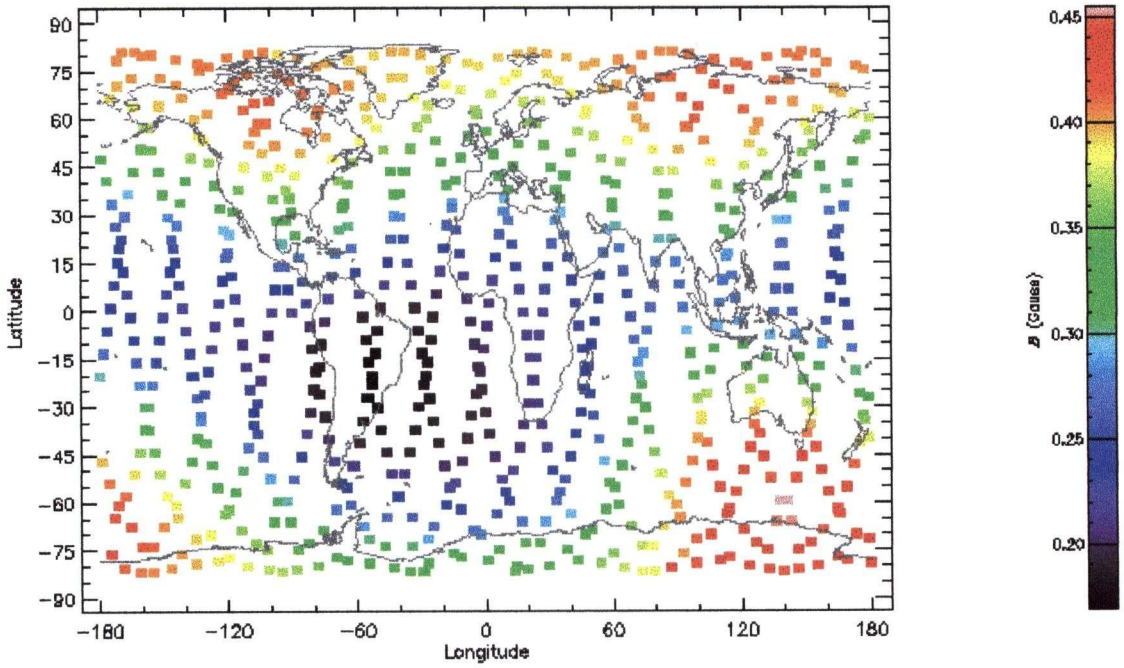

Figure 5.1 Magnetic field strength for the MOST baseline orbit (flight epoch 2002) clearly showing the depression in magnetic field strength associated with the SAA (Section 2.3.1).

AP8 and AE8 (Section 3.3), other geomagnetic field models were applied to see if any noticeable difference in proton or electron flux resulted. Models comparing the proton environments using GSFC-12/66 and the International Geomagnetic Reference Field (IGRF, see Section 2.3) showed nearly identical solar max trapped proton spectra (Figure 5.2). Hence, for solar maximum, the updated geomagnetic field models were employed as recommended from the authors of SPACE RADIATION 4.0. The Jensen and Cain solar minimum model JC60 was not accessible with the Space Radiation package and hence, variations due to the choice of magnetic field model during solar minimum were not investigated.

Additionally, IGRF2000 was imported into Space Radiation. IGRF2000, the most recently published of the reference field models, contains time derivates of the magnetic field so that secular variations can be included and the field can be exptrapolated to the MOST flight epoch of 2002. Thus, it is the most current representation of the Earth's magnetic field and the most realistic to use in modelling. Hence, the IGRF supplied and recommended by the Space Radiation software package were used and compared to the newly published IGRF2000. Although the model coefficients have changed between epochs, the overal strength of the inner magnetic field has remained constant. Thus, trapped proton spectra are identical for the newer and older versions of IGRF. However, scaling IGRF to the epoch of flight expected for the MOST microsatellite (2002) shows a minor increase in trapped proton spectra, related to the expected increase in solar protons injected from the current phase of solar maximum (see Figure 4.10). Dyer et al. (1998) note that despite the recommendations against using updated field models, using the newer field models did predict the correct number of passes of the STS-81 mission through the SAA. However, the definitive boundaries of the are still non-static and may require re-evaluation prior to the launch of the MOST mission.

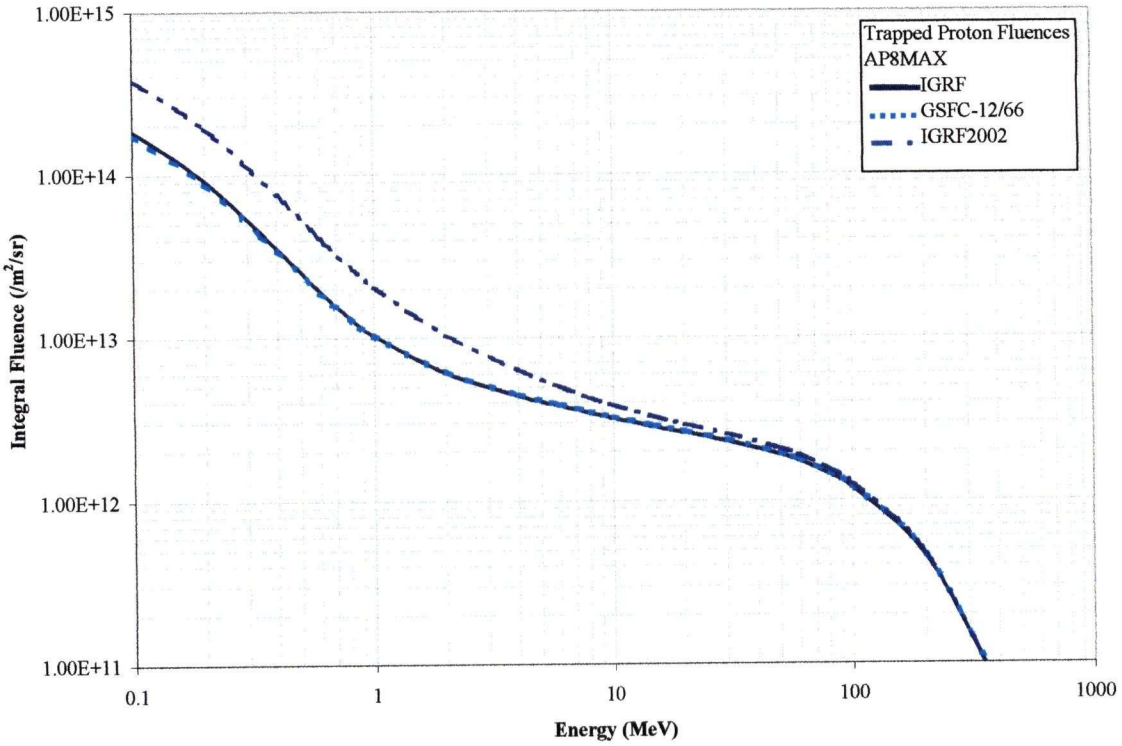

Figure 5.2 Trapped proton spectra for AP8MAX used with three different magnetic field models: IGRF, GSFC-12/66, and IGRF extrapolated to the MOST flight epoch of 2002. There is no noticeable difference between IGRF and GSFC-12/66. However, the flight epoch spectrum has slightly higher proton fluence due to solar modulation of the trapped proton population.

The Far Ultra-Violet Spectroscopic Explorer (FUSE) satellite, an internationally funded space satellite explorering the ultra-violet universe, spent extensive time mapping out the boundaries of the SAA during the first year of its mission (Alex Fullerton, personal communication 2000). Hence, MOST should take advantage of their experience and utilise the map generated by their team to predict when the satellite will enter the SAA to reject data which may be corrupted due to cosmic ray hits or malfunction of the Attitude Control System (ACS). Data taken during the passage through the SAA could be analysed and compared with the predictions from this study to further evaluate the validity of the models.

5.2 Geomagnetic Shielding

MOST will orbit at a relatively low altitude, where the geomagnetosphere will shield the satellite from much interplanetary radiation. The geomagnetic transmission function (Section 3.3), with and without the Earth's shadow, for the MOST baseline orbit is shown in Figure 5.3. Also shown is the case for a stormy magnetosphere disrupted by a large CME.

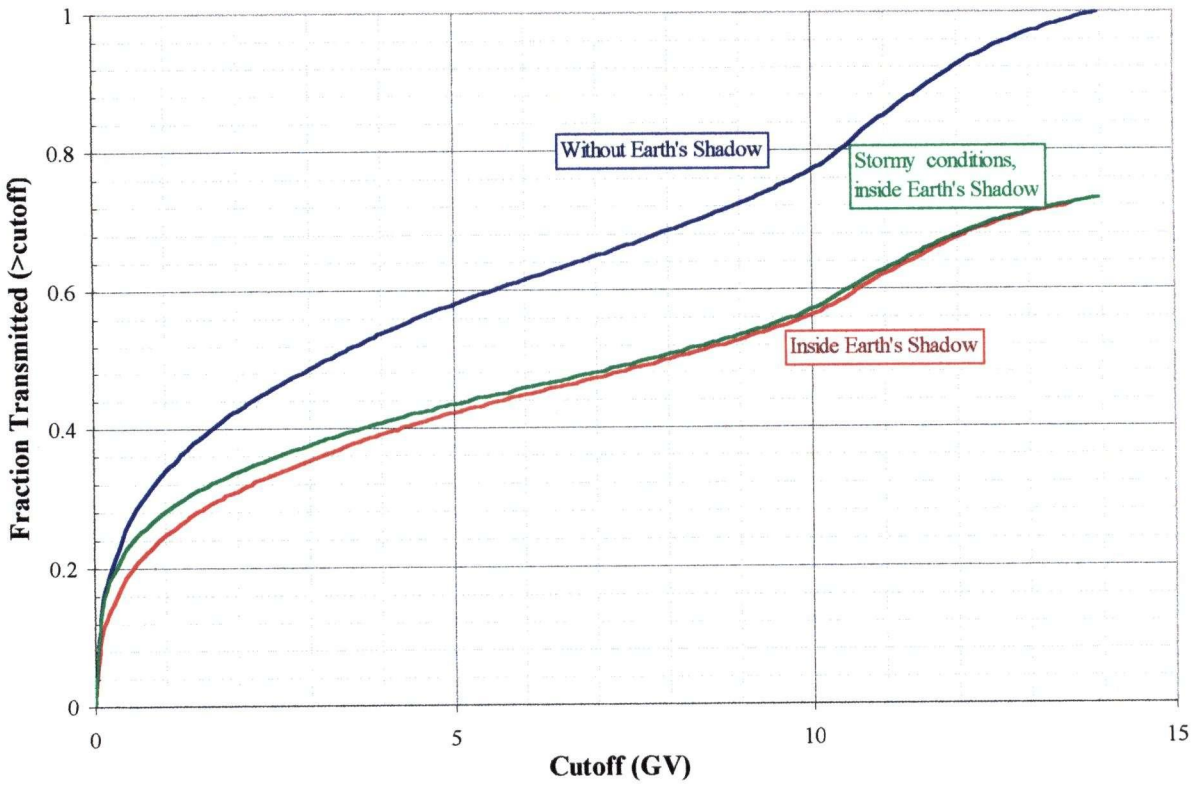

Figure 5.3 Geomagnetic transmission function for the MOST baseline orbit, for normal magnetospheric conditions (no storm).

5.3 Trapped Protons and Electrons

Along with solar energetic particles, the trapped proton and electron populations are the most significant in the MOST baseline orbit. AP8 and AE8 models (Section 3.2) were used to evaluate particle fluence over a specified mission lifetime. For the MOST microsatellite, it is possible to complete all primary science objectives within minimum mission lifetime (one year). Thus, the fluence levels presented here are an orbit-integrated flux (particle per unit area per year) over the baseline year long mission.

Figure 5.4 shows the integral fluence of trapped protons and electrons for the MOST baseline orbit for both solar maximum and solar minimum (minimum mission duration of 1 year). Since the trapped magnetospheric population is inside the magnetosphere, no geomagnetic shielding is applied. The proton flux varies by about a

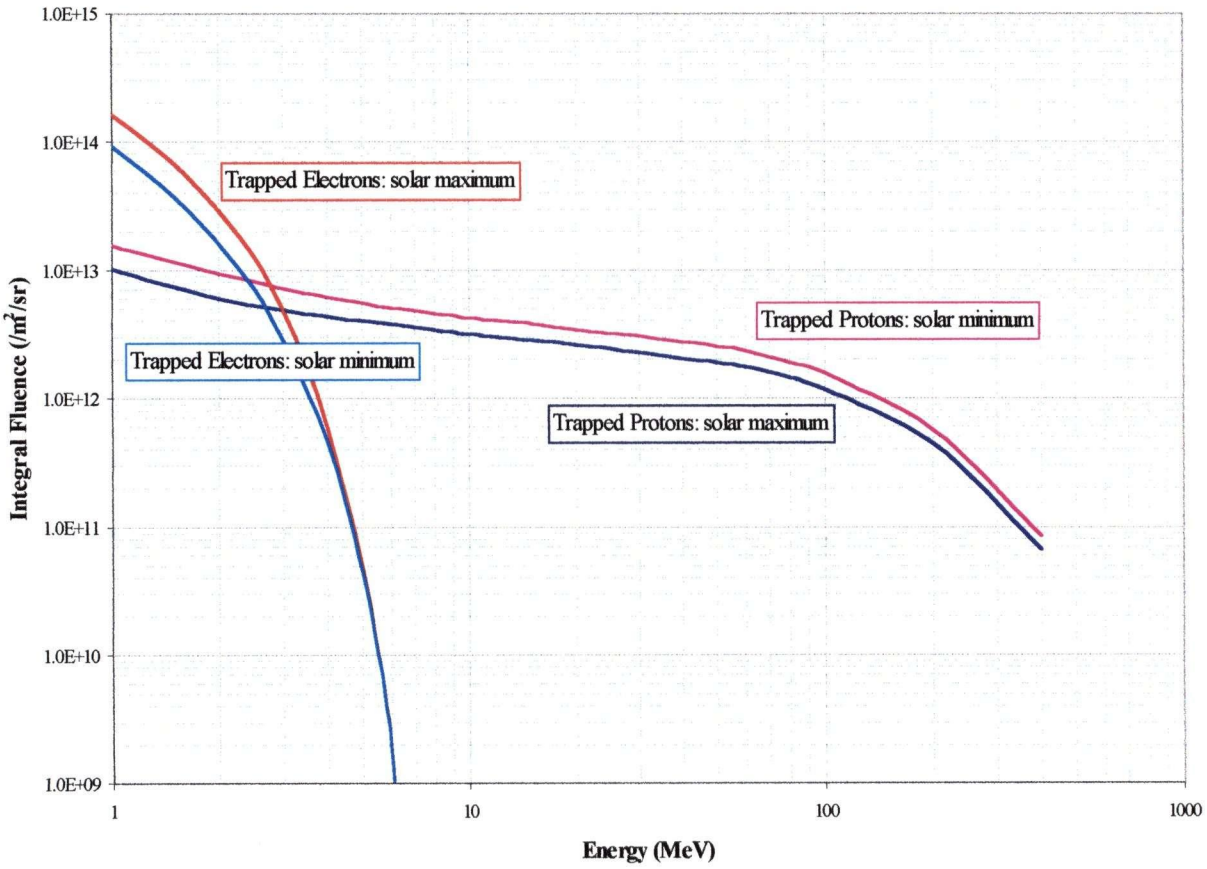

Figure 5.4 Proton and electron fluence over MOST minimum mission lifetime.

factor of 2 between solar maximum and solar minimum. Higher fluence during solar minimum are expected due to atmospheric expansion (Section 2.5). Since higher energy particles are also more penetrating to the shielding of spacecraft, the high-energy proton populations are the most important to consider.

Appendix D contains maps showing the particle environments for 0.1 MeV, 10 MeV, and 300 MeV protons as well as 1 MeV, and 5 MeV electrons respectively. The most dominant feature is the SAA, as expected. Lower energy particles, especially the lower energy electrons, are also found to occupy bands in high latitudes. At high or low latitudes, trapped magnetospheric particles in the outer radiation belts can reach low altitudes. These 'horns' are much less stable than the SAA as they are associated with the outer magnetosphere of the Earth and dynamically interact with the solar wind and associated magnetic fields. Hence uncertainties in the fluence of those particles are higher than estimated here. Since they are low-energy particles and won't be able to penetrate spacecraft shielding, a more comprehensive treatment of the uncertainty of the fluence for this population was not undertaken.

5.4 Galactic Cosmic Radiation

The Galactic Cosmic Radiation component was calculated using CREME (Section 3.4). Integral and differential flux spectra for the MOST microsatellite due to GCR during solar maximum and minimum under normal geomagnetospheric conditions with a 3-D shielding representation of the cavity in which the charged coupled device (CCD) resides applied (Section 1.3.1 & 5.7) are shown in Figures 5.5 and 5.6 respectively.

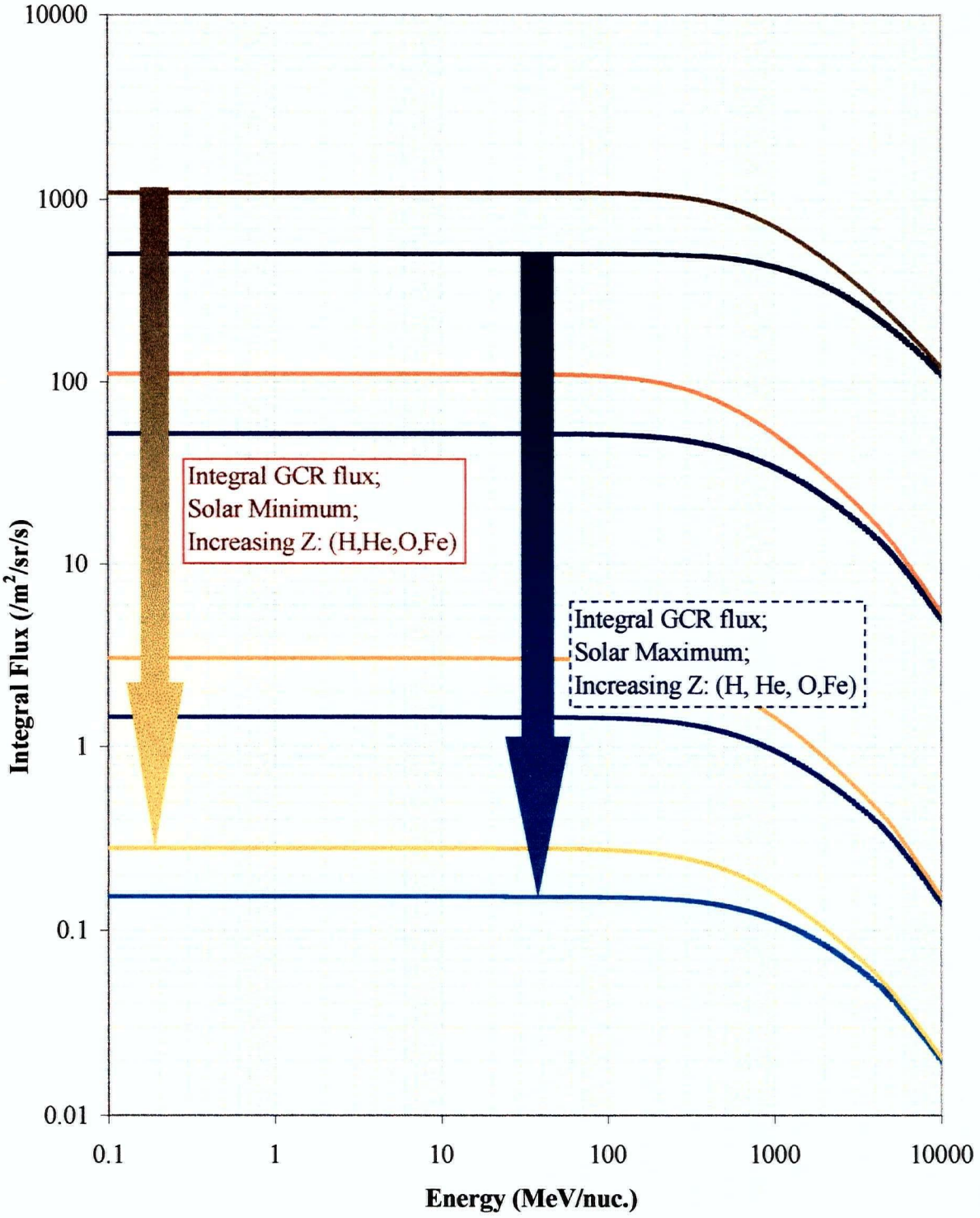

Figure 5.5 Integral flux energy spectrum of GCR expected to hit the CCD detector.

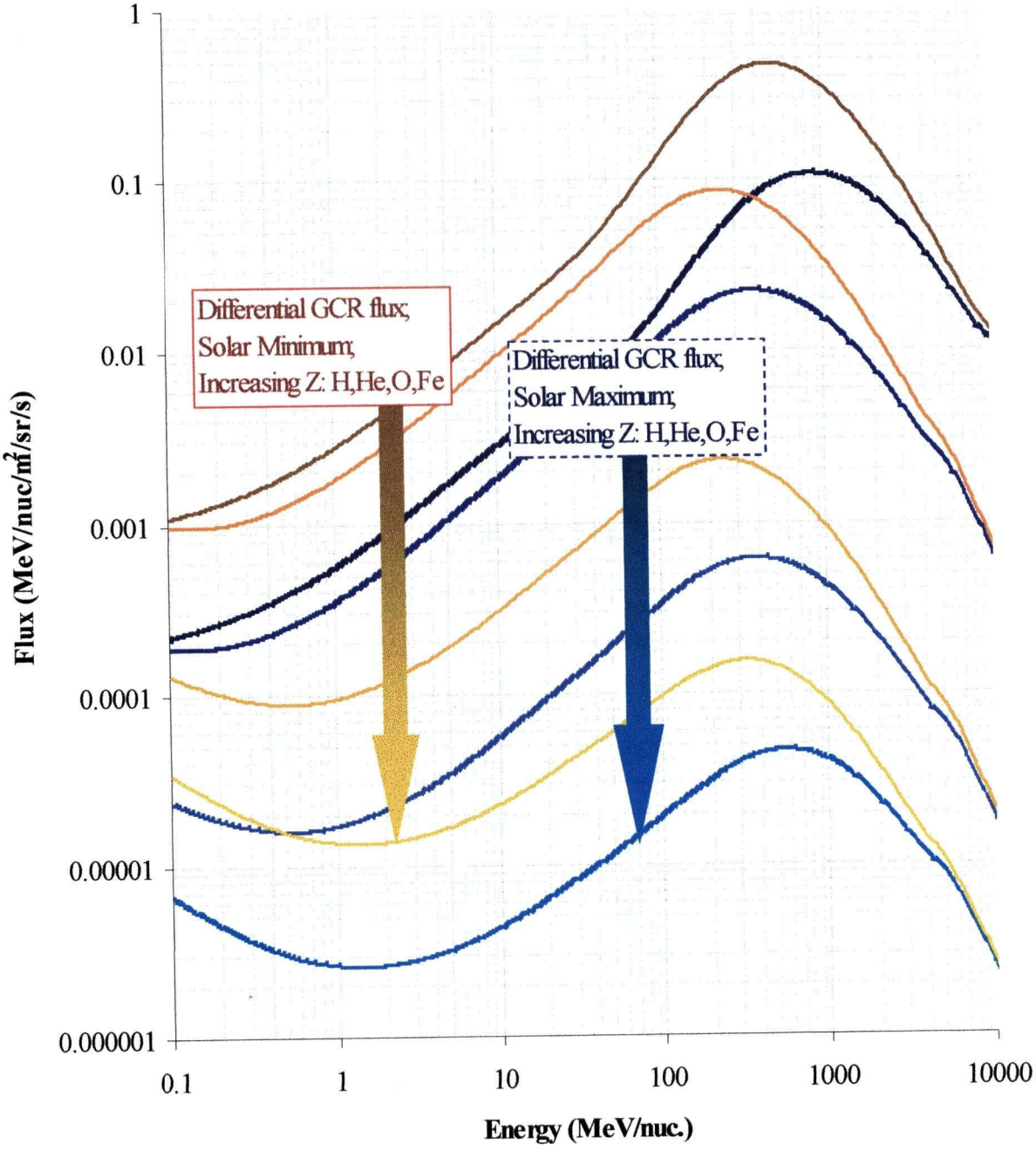

Figure 5.6 Differential flux of GCR penetrating behind a 3-D shielding geometry. This is the GCR flux expected to hit the CCD detector.

The 1 MeV integral flux due to GCR inside the MOST spacecraft is about $1000/(m^2\ sr\ s)$, yielding a one year fluence of $2.14 \times 10^{10}\ /m^2/sr$. Compared to the proton fluence inside the spacecraft ($\sim 2 \times 10^{12}$ for 1 MeV protons; Section 5.3) the GCR is about 2 orders of magnitude lower than the trapped proton flux. Thus, the cumulative ionising dose due to GCR will be negligible compared to the populations trapped in the Van Allen Radiation belts. However, since the GCR ions are much heavier, they create more Single Event Upsets (SEUs, Section 6.2) than the proton population.

5.5 Anomalous Cosmic Radiation

The integral and differential flux due to ACR as predicted by CREME, propagated through the Earth's geomagnetosphere and 5mm of Al cylindrical shielding (Section 5.7), are shown in Figure 5.7. These spectra scale to larger fluxes with less shielding and vice versa for additional shielding. The larger first ionisation potential of N relative to O results in the flux of N in the ACR being slightly higher than that of O.

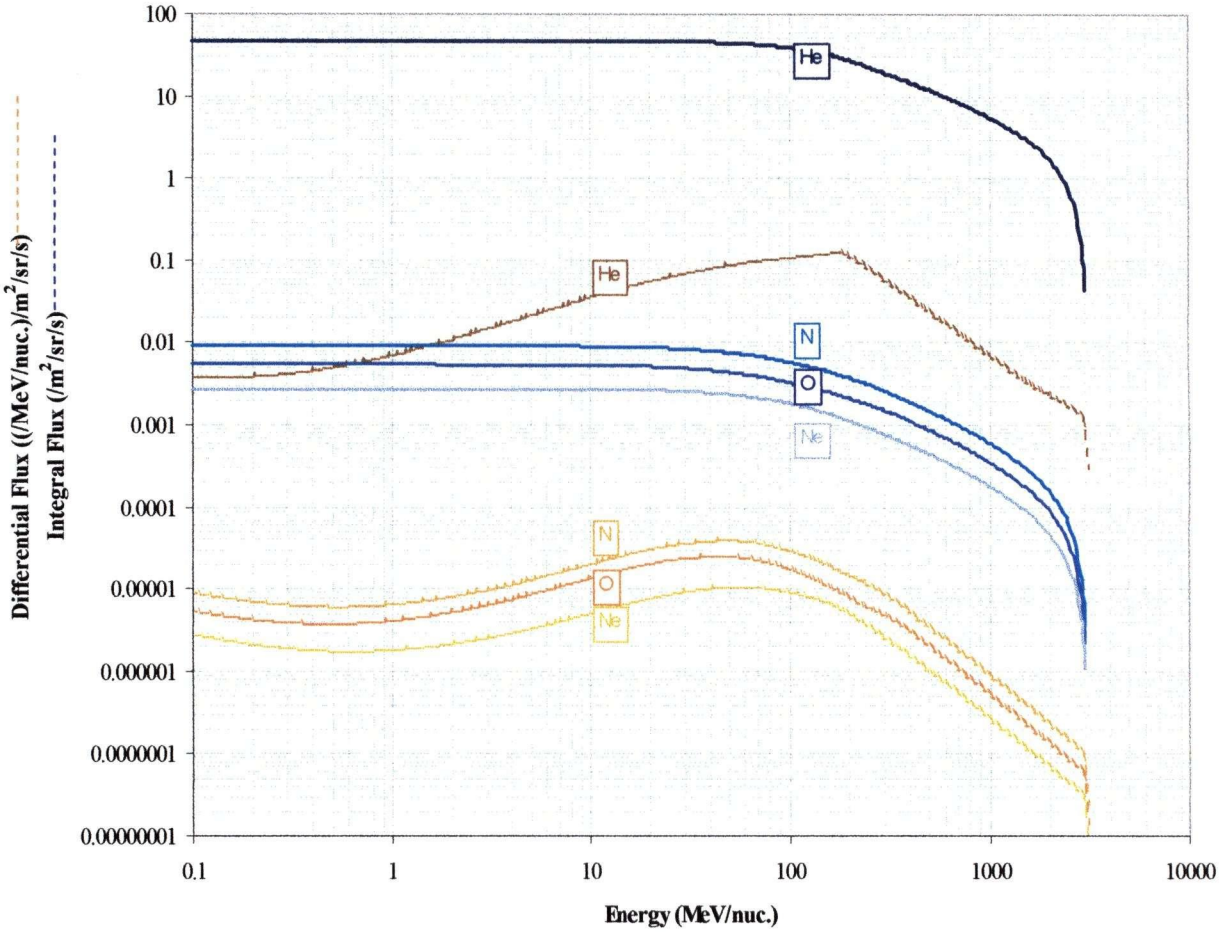

Figure 5.7 Integral and differential flux energy spectra of ACR.

5.6 Solar Energetic Particles

The energy spectra associated with the 5 different SEP events described in Section 3.5 are shown in Figure 5.8, again with geomagnetospheric and 5mm of Al cylindrical spacecraft shielding (Section 5.7) applied. The JPL 1991 is the most reliable and statistically accurate model. However, it represents data averaged over a 5-year time frame. Since MOST is being launched during the decline of solar maximum, it is more likely that a large SEP event will occur.

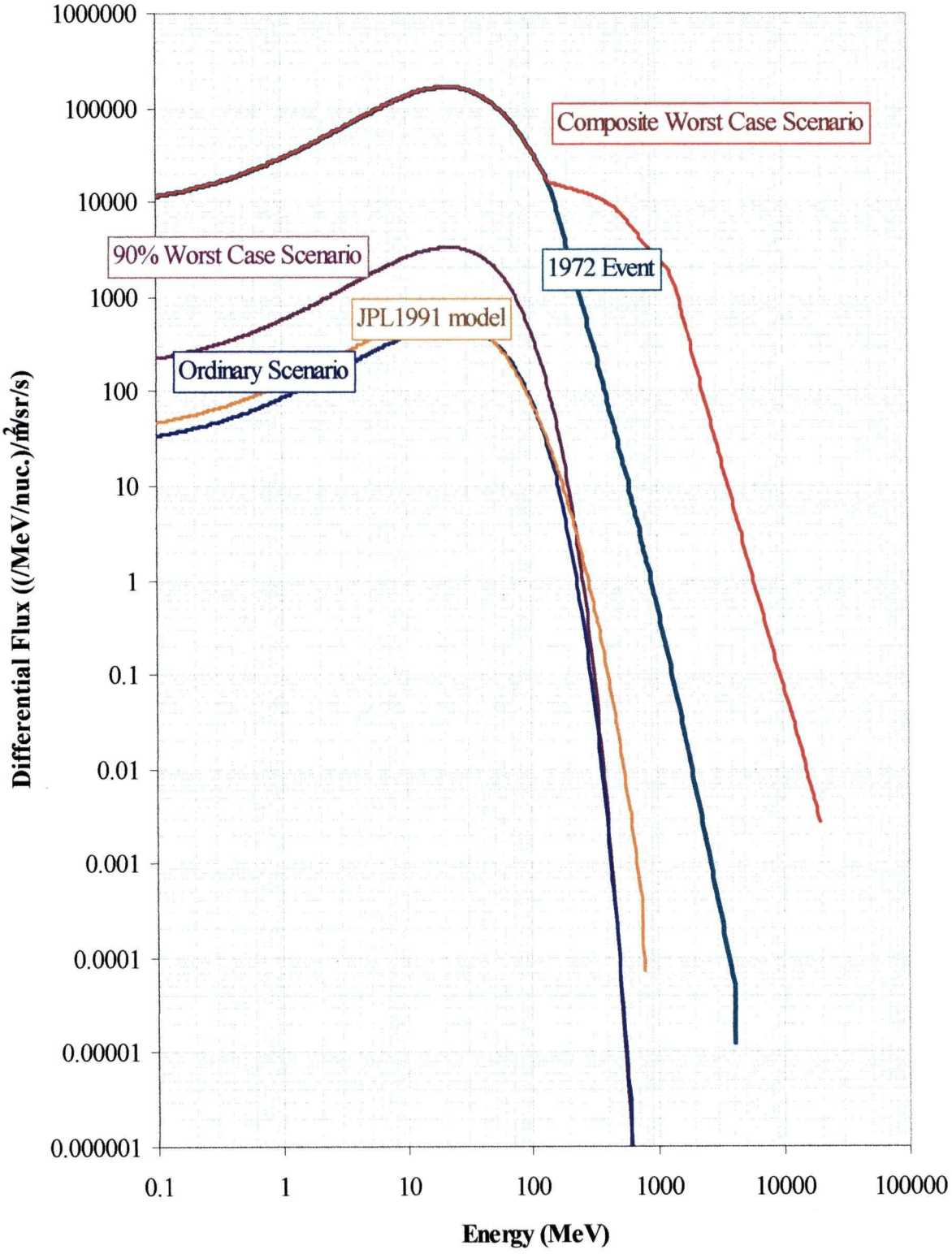

Figure 5.8 Differential energy spectra of SEP events.

5.7 Satellite Shielding

Referring back to Figure 3.1 and the approach to modeling the radiation environment, the next step in the radiation analysis for the MOST microsatellite is apparent. The contributions due to galactic cosmic rays, solar protons and magnetospheric particles all contribute to the spacecraft incident fluence. However, shielding stops many of the incident particles from interacting with spacecraft sensitive components. Thus, the shielding of the MOST design must now be considered.

Simple Shielding Geometry

The first step in the radiation analysis is an assessment of the radiation environment behind standard simple shielding models. The three models for simple shielding included with the SHIELDOSE-2 code developed by Al Vampola (1996) are (1) a finite Al slab, (2) a semi-infinite Al slab, and (3) an Al sphere. The results for the SHIELDOSE-2 calculations for the MOST baseline orbit are shown in Figure 5.9. Included is the dose vs. depth profiles for trapped protons and electrons from AP8/AE8 during solar maximum, as well as solar protons from the JPL91 model contributing to the total dose inside an Al sphere. Included in the electron dose is brehmstrahlung emission. Since the dose vs. depth curves of the simple shielding geometry analysis level off, the advantages of thicker shielding start to decline, especially as thicker shielding quickly adds mass to the satellite. Thus, in balancing shielding vs. less mass, the optimal shielding thickness appears to be around 5 mm from Figure 5.9 (additional shielding dose not reduce over all dose significantly). A critical dose for MOST is on the order of 10 krad in Si (one rad is equivalent to 100 ergs of energy absorbed by 1 gram of material), so the minimum amount of shielding needed is conservatively estimated as 3 mm. However, since preliminary estimates of minimum shielding thickness were 10 mm (Matthews, 1997), the revised minimum estimate of 5 mm of Al shielding is sufficient to ensure the duration of the mission for just less than 10 years, as well as reduces overall mass of the instrument.

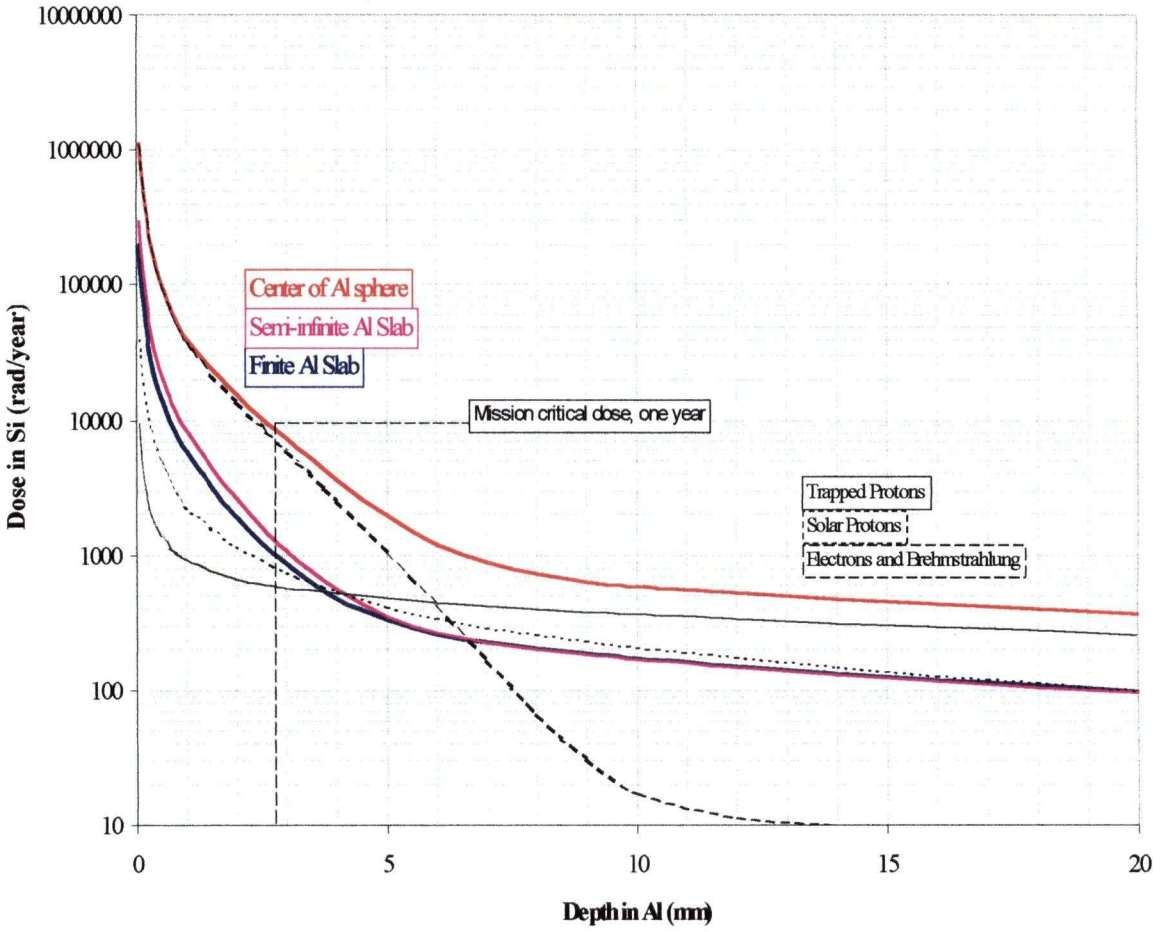

Figure 5.9 Dose vs. Depth curve for simple shielding geometry based on SHIELDOSE-2. The red line is for a 4 Pi Al Spherical shield, the pink for an infinite Al slab, and the blue for a finite Al slab. Also shown are contributions from trapped protons, JPL91 SEP, and trapped electrons for the Al spherical shielding case.

3-D Shielding Models

Of course, the MOST satellite is neither a sphere nor a plane slab. Once the design was significantly mature (incorporating preliminary shielding recommendations), a more detailed shielding model was generated using SPACE RADIATION 4.0. An engineering schematic of the MOST satellite is shown in Figure 5.10, along with a schematic of the 3-D cylindrical model used to generate the cumulative doses of the MOST mission. The telescope structure itself, approximately an 8-mm thick cylinder of INVAR (a steel alloy) acts as shielding. The most sensitive component within the satellite structure is the Charged Coupled Device (CCD) which sits about 3/4 of the way towards the back of the telescope. Immediately surrounding the CCD is the camera housing, another cylinder about 2 mm thick and made of Ti.

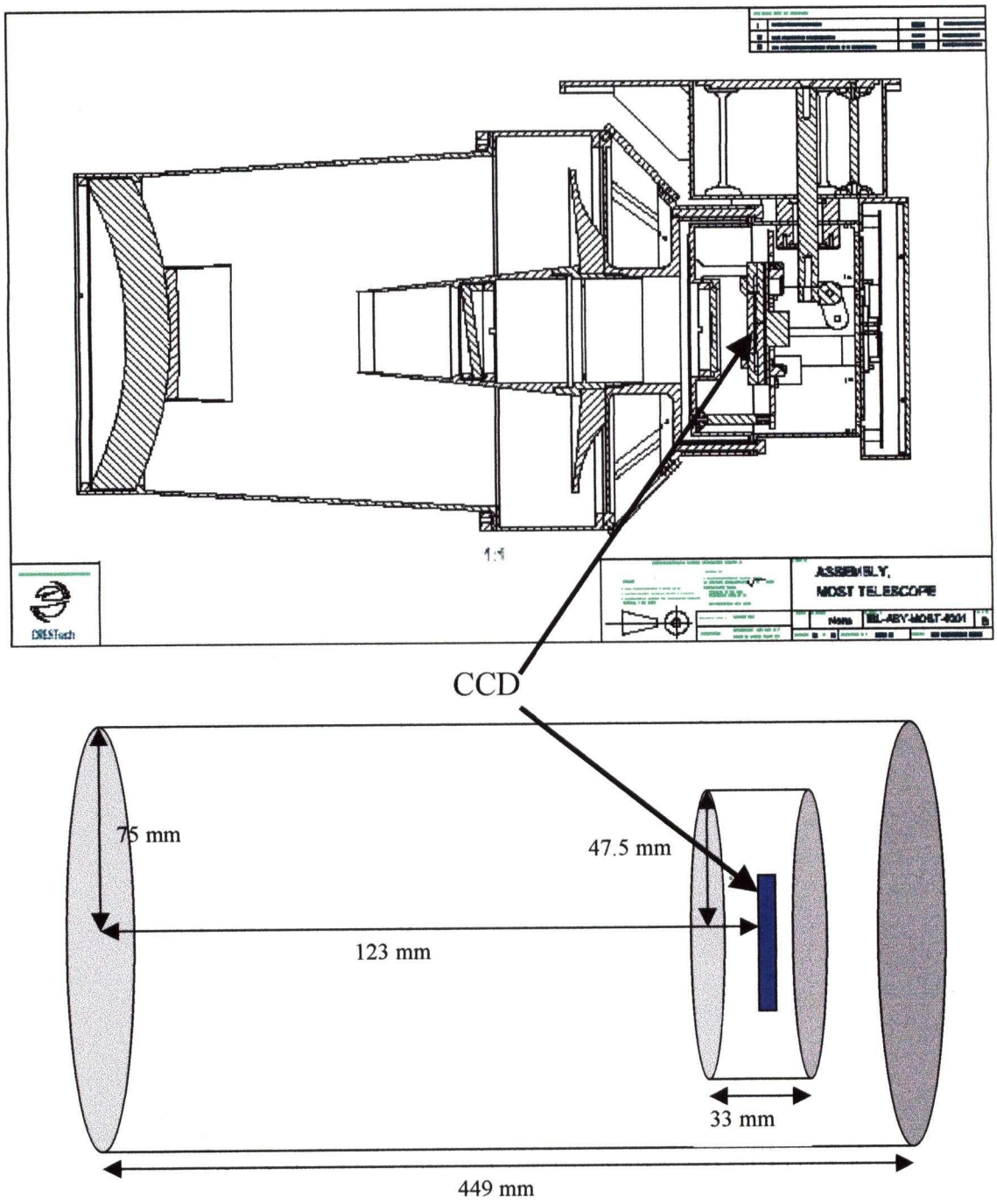

Figure 5.10 Engineering schematic of the preliminary MOST satellite design (top) and schematic of 3-D shielding geometry used to represent satellite shielding. The outer casing is representative of the telescope tube, and the inner casing is representative of the camera housing.

Aluminum (or Al equivalent) shielding removes low-energy particles more effectively than high-energy particles. Figure 5.11 illustrates this by comparing the trapped proton integral fluence spectra for a non-shielded, and a shielded case (inside tube 5-mm thick with the MOST telescope dimensions). Recall that integral fluence is the flux integrated over a baseline mission lifetime of one year.

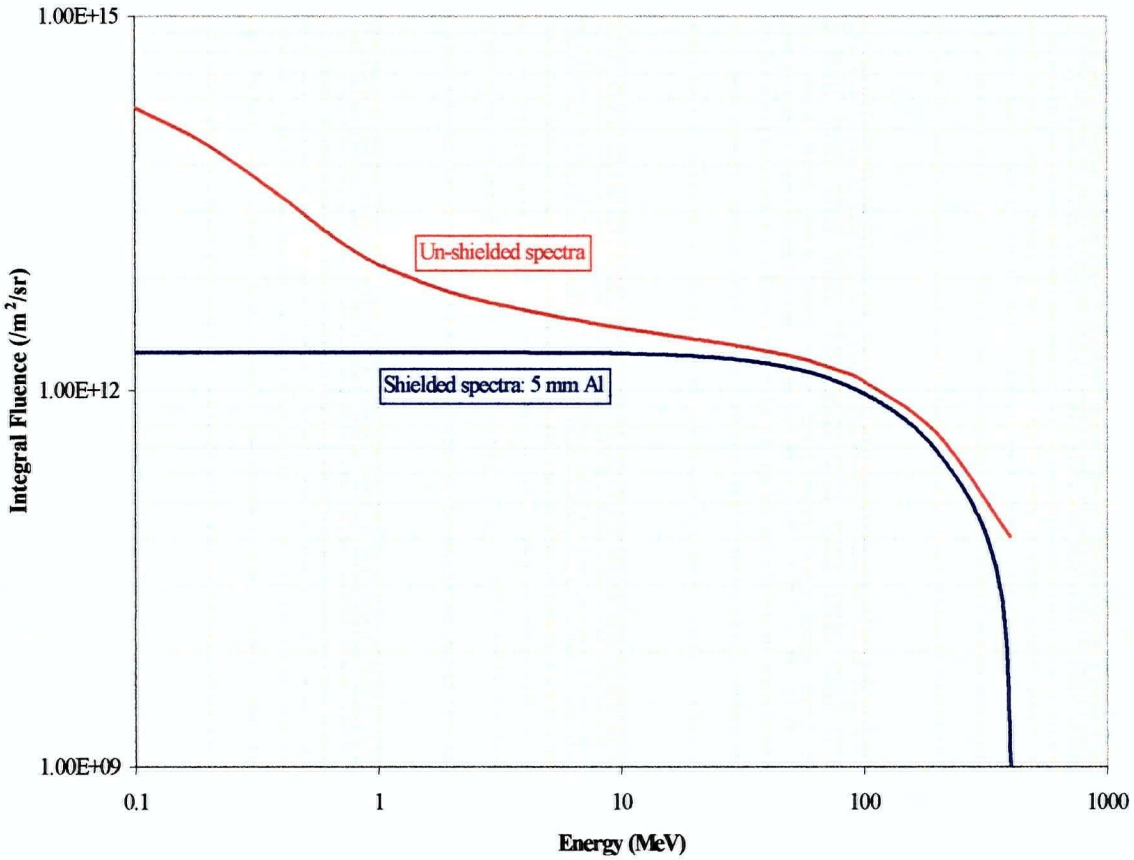

Figure 5.11 Comparison of the integral trapped proton fluence outside the spacecraft, and behind 5 mm of Al cylindrical shielding with the MOST satellite dimensions as shown in

The charged particle must penetrate the shielding with sufficient energy to further penetrate into the sensitive volume of the spacecraft component to do any damage. Thus, the incident spectra are described in terms of the linear energy transfer or LET spectrum (Figure 5.12). LET is a measure of the rate of energy deposition in a sensitive volume of the device per unit path length. It is essentially a description of the ability of the particle

to transfer its energy into crystal lattice of the device, or into ionising one of the atoms. Of course, the LET is dependent on the device structure itself, what it is made of and how easily the bonds between molecules are broken. Since the majority of electronics are based on a Silicon crystal lattice, the LET presented here are for Si detectors. Knowing the LET thresholds of the devices on board the spacecraft allows a direct comparison between the radiation environment and the sensitive components. Figures 5.12 and 5.13 show the LET spectra for trapped protons and SEP (JPL91) respectively during solar maximum for 3 different shielding models. Figure 5.14 shows the LET spectra for GCR. Since the majority of the ions in GCR are heavy ions, the LET is not sensitive to the shielding model.

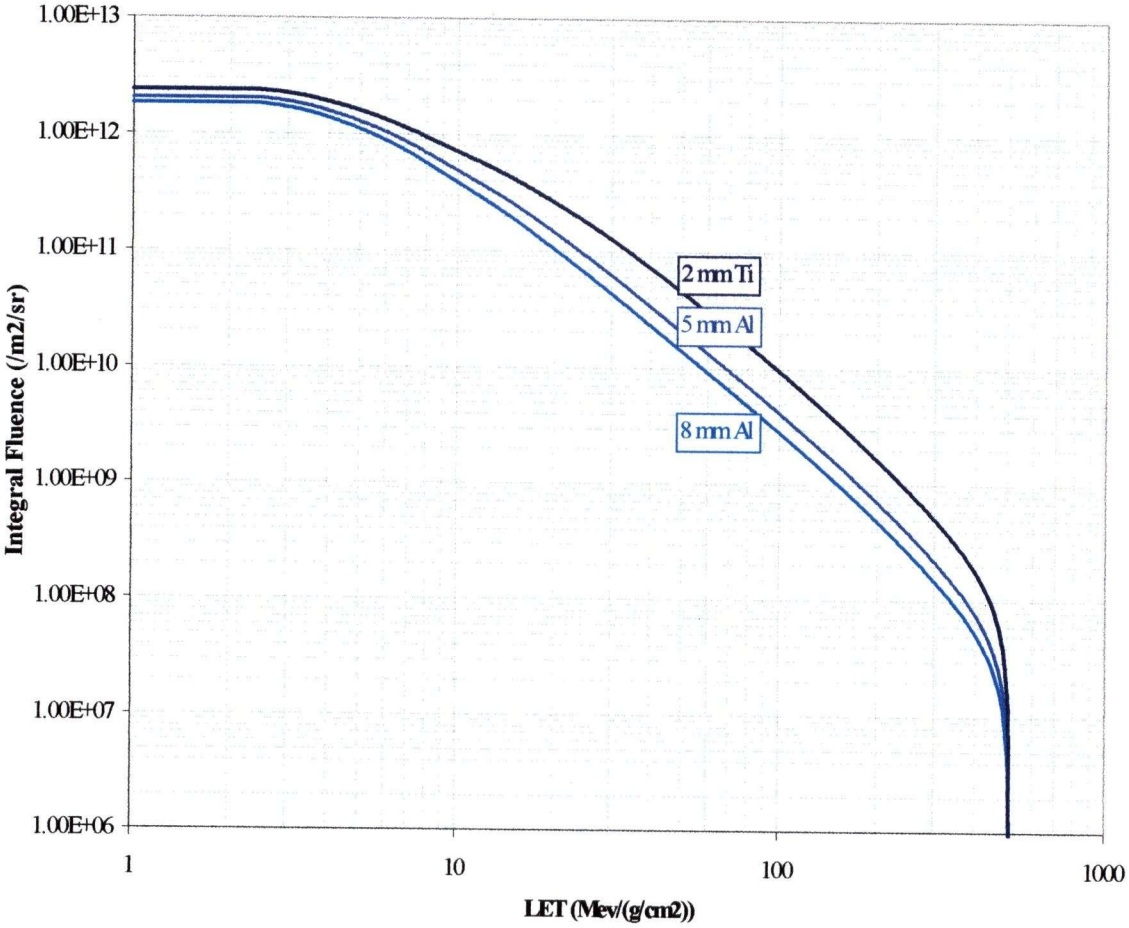

Figure 5.12 LET Spectra of trapped Protons for (a) 2 mm Ti shielding with MOST camera housing dimensions, (b) 5 mm Al shielding with MOST telescope tube dimensions, and (c) 8 mm Al shielding with MOST telescope tube dimensions.

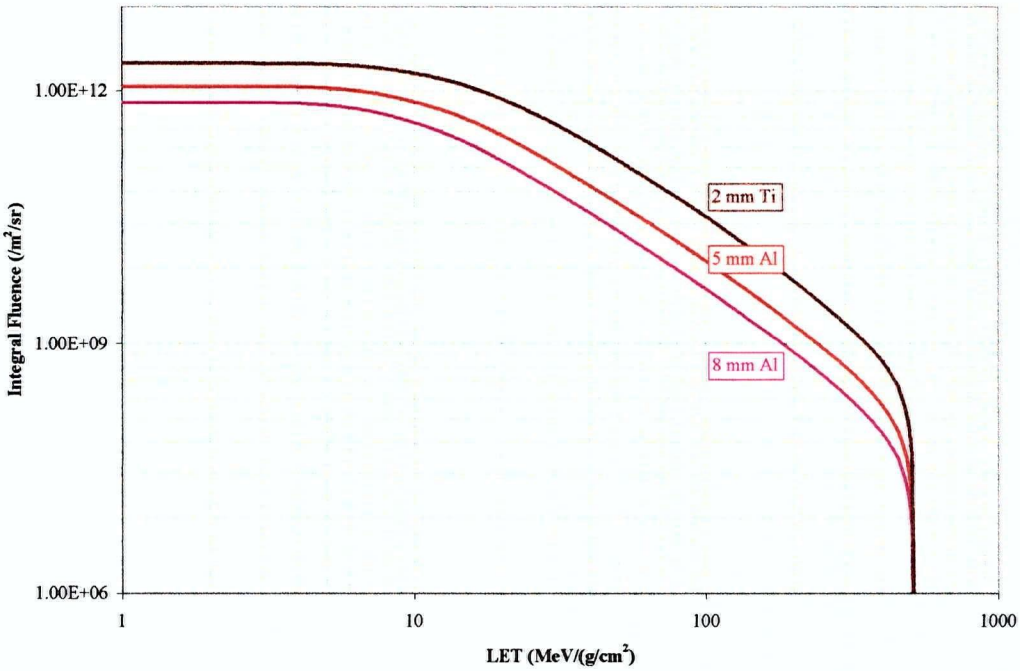

Figure 5.13 LET spectra of solar energetic protons as modeled by JPL91.

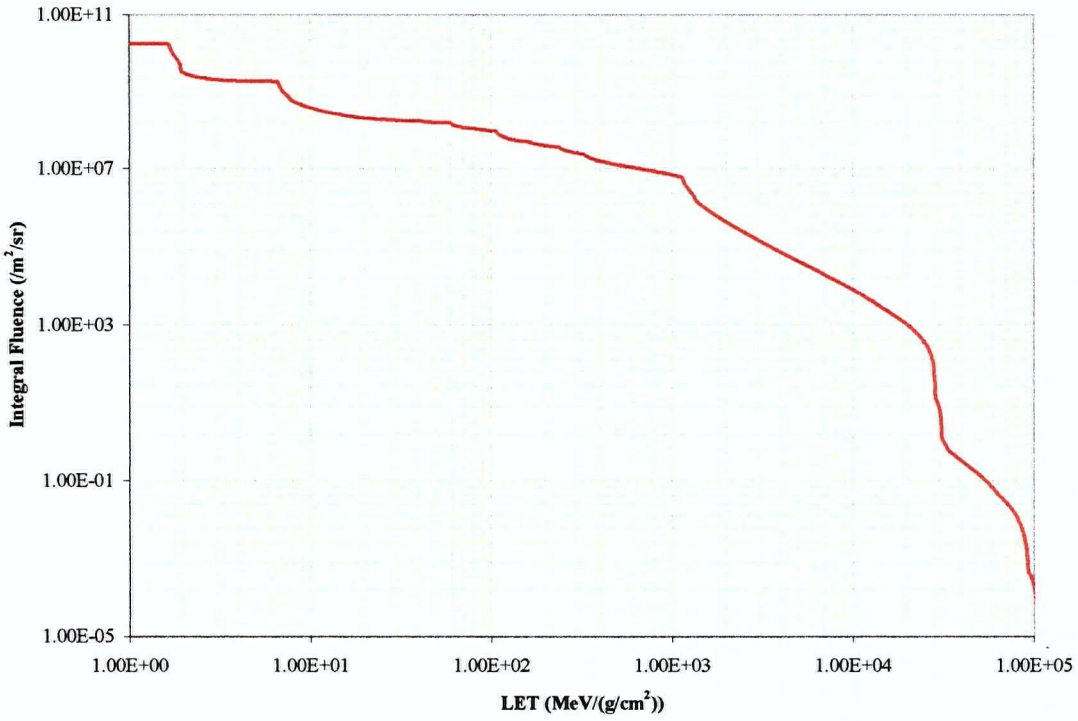

Figure 5.14 LET spectra due to GCR.

5.8 Cumulative doses

Charged particles interact with Silicon based electronics onboard in the satellite in three ways: (a) ionisation, (b) displacement, or (c) SEU (Section 6.2). Whether a proton will cause ionisation damage or displacement damage depends on the incident particle's energy. The LET spectra contain information on whether the particle will damage the electronic device through ionisation or displacement. Hence, there are two cumulative doses to be calculated: ionisation dose and displacement dose. Cumulative and displacement doses are tabulated in Appendix E.

MOST will experience about 1 krad of ionising dose per year. Since only the telescope itself has been considered as shielding, this is a very conservative estimate. The satellite structure itself will contribute additional shielding. If there is a large flare and a large geomagnetic disturbance, then MOST could experience an additional krad ionising dose. Again, according to recent experience, this is a grossly conservative number. The good news is that MOST should be able to withstand even the harshest radiation environment it is likely to encounter in the range of orbits considered for it.

Total displacement damage will be on the order of 0.7 rads in Si, or 7×10^8 1 MeV proton equivalents/cm^2). One rad (Si) is approximately equivalent to a flux of 4×10^7 (energy ~1MeV) ionising particles/cm^2 (Bailey 1996). The effects of the displacement damage as well as the ionising dose are further investigated in Chapter 6.

The uncertainties in the radiation environment models are discussed in Section 3.6. Table 5.1 summarizes the estimated uncertainties in the models. Doses calculated using these models are only as good as the models themselves.

Particle Population	**Model**	**Uncertainty**	**Under/Over-prediction**
Trapped Protons	AP8	1.7-2.0	Under-prediction
Trapped Electrons	AE8	2	Over-prediction
Solar Protons	JPL1991	97% accuracy	Depends on Flare Number
GCR	CREME	2-5	Depends on Solar Max/Min
ACR	CREME		Gross Over-prediction

Table 5.1 Uncertainty in radiation environment models.

5.9 Dose versus Altitude

Although there are many arguments favoring the baseline orbit, there is no guarantee that the MOST microsatellite will end up in its ideal orbit. Thus, the dose as it varies with orbital altitude over a set of sun-synchronous orbits has been evaluated for quiet magnetospheric conditions at solar maximum in the center of an aluminum sphere (as per simple shielding geometry described in Section 5.7). As expected, the dose increases very slightly at higher altitudes as the orbit creeps upward into the heart of the Van Allen Radiation belts. As shown in Figure 5.15 the dose increases by about 50 krad per year per 100 km increase in orbital altitude (with 5 mm of Al shielding).

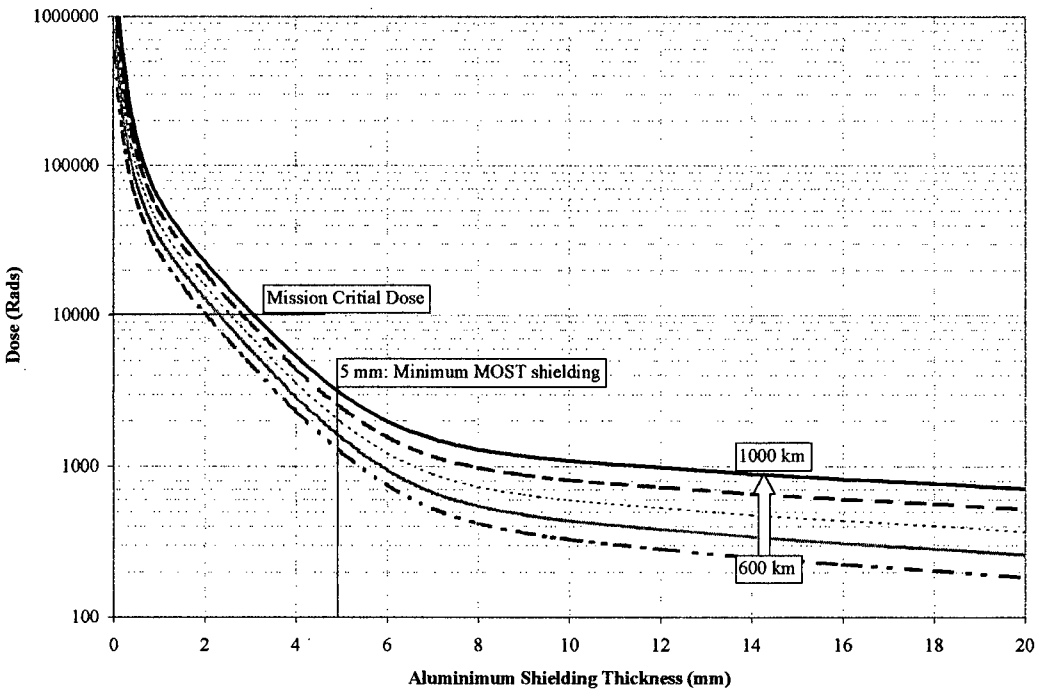

Figure 5.15 Dose at the center of an Aluminum Sphere for heliosynchronous orbits with different altitudes ranging from 600 to 1000 km.

The SAA covers a much larger area at higher altitude, as the orbital plane creeps upward into the heart of the Van Allen Radiation Belts. At 1000 km, energetic particles from both horns will bombard the satellite. Figure 5.16 shows the outline of the SAA at

600 km, 800 km, and 1000 km. Since data collection may be reduced for much of the high energy regions of the SAA, MOST should not consider increasing orbital altitude significantly.

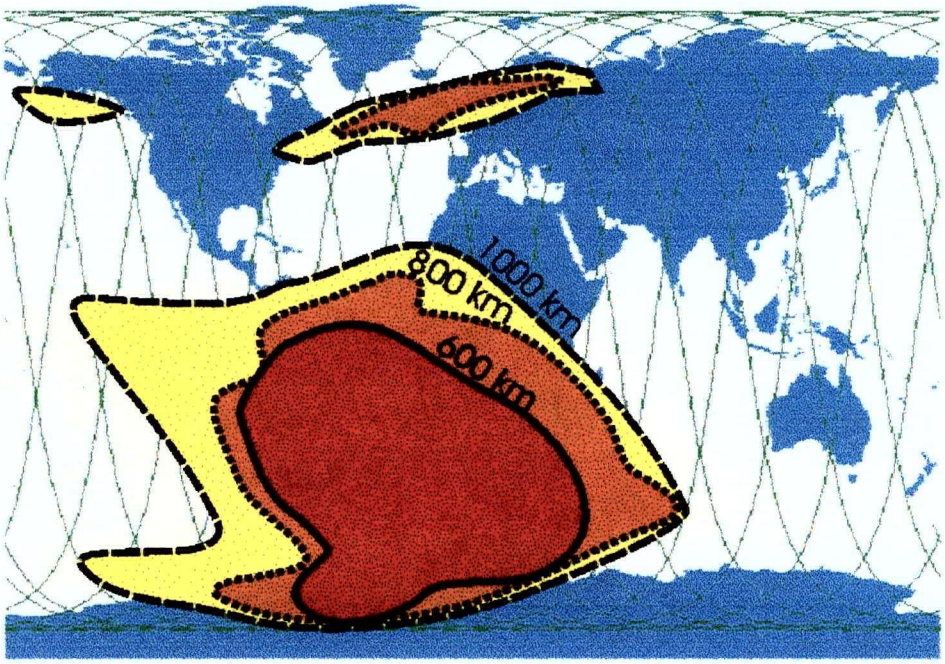

Figure 5.16 Approximate boundary of the SAA at 600, 800, and 1000 km altitude.

Chapter 6: Rain or Shine? Implications of Space Weather on MOST

The primary effects of the radiation environment on the MOST microsatellite are the following:

(a) ionising particles will damage the CCD and electronics (including degradation of charge transfer efficiency (CTE) and localised 'hot' regions of permanently damaged pixels);

(b) high energy particles will alter structure of silica lattice in electronics causing displacement damage;

(c) single event effects (SEEs);

(d) and a reduced duty cycle from a possible loss of observations through the SAA (Section 4.4).

To understand how serious effects (a) - (c) are, it is necessary to examine the CCD detectors to be used on MOST. Appendix F contains the Specification Sheet for the off-the-shelf version of the MOST CCD.

The radiation specification of the CCD (Section 1.4) issued by Marconi is the following:

"Device parameters may begin to change if subject to greater than 10^4 rads. This corresponds to 10^{13} of 15 MeV neutrons/cm^2, 2 x 10^{13} of 1 MeV gamma/cm^2, or 4 x 10^{11} of ionising particles/cm^2." (Marconi 2000)

Marconi conducts many radiation tests of their own CCDs in order to provide their customers with estimates of the change in specification with radiation degradation. Thus, the document prepared by Robbins (2000) on the performance of Marconi CCDs under radiation damage is utilised to evaluate the performance of the MOST CCD in the environment described in Chapter 5.

6.1 CCD Damage

CCD technology has advanced greatly in the past decade in response to demands for better scientific imaging. However, the increase in sensitivity of CCDs has been at the price of an increased sensitivity to radiation damage in space through (1) ionisation damage, and (2) displacement damage.

Ionisation damage, as shown in Figure 6.1, can have two effects on CCDs. If an incoming energetic particle hits the semiconductor lattice, it acts much like an incoming signal photon would, freeing an electron and leaving and electron-hole pair. The electron is freed and an electron-hole pair remains. However, the electron-hole pairs tend to congregate at the oxide-conductor interface, creating a positive charge buildup at the interface. This directly shifts the flat-band potential of the CCD. Mid-gap trapping states are also generated, creating an increase in dark current through thermal 'hopping' of electrons. Deep trapping states also are created, reducing CTE (charge transfer efficiency, Section 6.1.5).

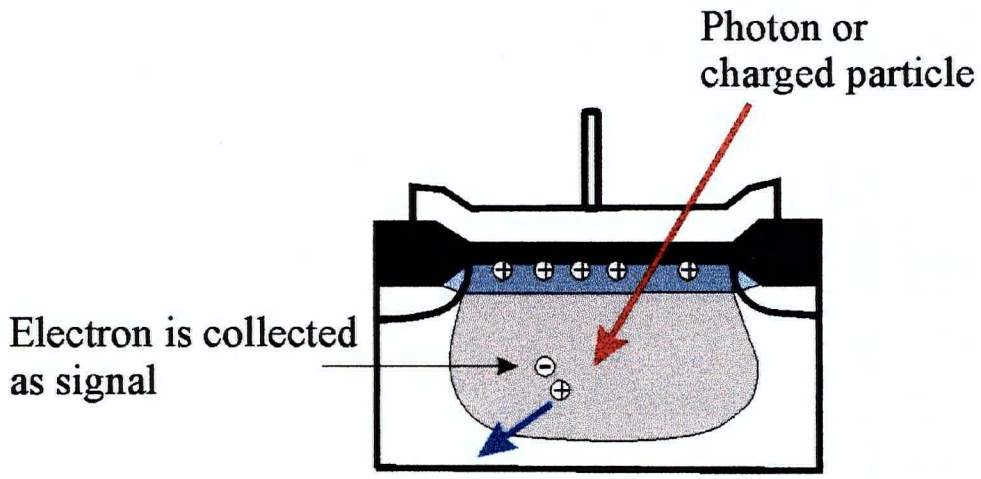

Figure 6.1 Charge generation or ionisation damage occur in the same manner in CCDs.

Ionisation is strongly dependent on the charge of the incoming ion squared, Z^2. Thus, the more abundant, lower Z ions can do as much damage as the less abundant, higher Z particles (Tribble et al. 1999).

Displacement damage (or bulk damage) has more lasting effects on CCDs. An incoming particle (proton or high-energy neutron) strikes the lattice of the semi-conductor and displaces one of the (Si) atoms in the lattice, leaving a vacancy as shown in Figure 6.2. The vacancies tend to congregate together and around impurities in the lattice, creating permanent trapping states within the semi-conductor itself. Shallow trapping states increase dark current and deep trapping states both decrease CTE and increase read noise similarly to ionisation damage. "Hot" pixels, or regions with extreme intensities unrelated to the signal, develop where the vacancies congregate, due to the extreme dark current associated with the mid-gap trapping states.

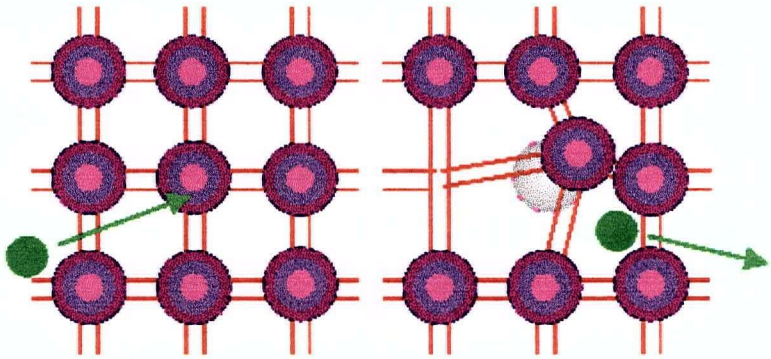

Figure 6.2 An energetic particle strikes a Si atom of the semiconductor lattice and kinks the structure, leaving a vacancy. Vacancies congregate together and about impurities in the crystal lattice. (After Hardy 1997)

Either ionisation damage or bulk damage will induce the following:

(a) Dark current increase due to ionising radiation;

(b) Dark current increase due to bulk damage;

(c) Damaged pixels;

(d) Random telegraph signals;

(e) Flat band voltage shifts;

(f) CTE degradation.

6.1.1 Dark Current

In every CCD, some current is generated even when photons are not incident on the detector. This background signal is called the *dark current*. Since dark current generation creates a random number of electrons per pixel, it is a noise source.

Dark current is primarily a thermal effect. If electrons in the valence band (or in the valence shells of silicon in the crystal lattice) possess enough energy, then they move to the conduction band, i.e., to the inversion layer where they are trapped and then collected as signal. Thus, if an electron in the valence band possesses sufficient thermal energy, it can be attracted to the conduction band without added energy generated by the photoelectric effect or by interactions with a charged particle. The probability of an electron possessing sufficient thermal energy to do this is given by the following formula:

$$P = \frac{1}{1 + e^{(E_c - E_f)/kT}} \tag{6.1}$$

where E_c is the energy of electrons in the conduction band, and E_f is the Fermi energy of the electron. k is the Boltzman constant and T is the operating temperature of the CCD (Hardy 1997). Thus, at lower operating temperatures, dark current is suppressed. This is one of the main reasons to operate the MOST CCD at -40°C. Cooler temperatures would reduce dark current even further, but require a more expensive cryogenic cooling system as opposed to a passive cooling mechanism.

Dark current due to radiation damage can be created by either ionising or bulk damage. Ionising radiation induces enhanced dark current by increasing the interface state density of the depleted surface areas of the device (Robbins 2000). If an incoming

charged particle interacts with a silicon atom at the silicon-silicon dioxide interface (in a non-buried channel device), it can create a mid-gap trapping state, essentially a lower energy pathway for electrons to move about in the silicon lattice. This effectively increases the energy of the valence band electrons, or decreases the effective energy of the conduction band electrons as seen by the valence band electrons. Thermal hopping of electrons increases and the dark current of the detector increases. Since the MOST device is operated under inversion, the majority of this surface generated signal is suppressed. Hence, there are not many radiation tests to compare to. The only absolute measurement has been made by Brunel University, but not on a Marconi device. They found an increase of 1.5 pA/cm^2/ krad (Si), or 15 e$^-$/pix/s/krad (Si) at 30°C. The effect of ionising radiation damage on dark current at -40°C should be negligible (~0.03 e$^-$/pix/min/krad).

Dark signal increases can also be caused by displacement damage. In a similar fashion to the creation of mid-gap trapping states in the case of ionisation damage, bulk damage also results in the formation of a lower energy pathway for electrons. The biggest difference is that the lower energy pathway is now in the bulk structure of the p-type silicon, as opposed to being confined to the interface region. Since the trapping states created by displacement damage are very good at transferring electrons through thermal hopping, the disrupted lattice can essentially be considered a dark current generation center. Bulk damage is independent of bias state. Since the signal generation centers are in the depletion region and not in the surface region, inversion will not suppress this signal.

Tests of a Tektroniks backside illuminated, buried channel device similar to the MOST CCD were made by Hardy (1997). For the device running in MPP mode, the baseline dark current was less than 1 e$^-$/pixel/s (at -40°C). After irradiation with 6.0 x 10^9 3 MeV protons/cm^2, the dark current increased to 2 e$^-$/pixel/s, and after 1.5 x 10^9 3 MeV protons/cm^2, the signal was up to 9 e$^-$/pixel/s, again at -40^{0}C. In a worst case scenario with an extremely large flare event, MOST will see 1.93 x 10^9 1 MeV protons/cm^2. Thus, we can expect a small increase in dark current due to bulk radiation, on the order of 1 e$^-$ /pixel/s.

Both effects are temperature dependent. The ionisation damage increase in dark current varies as $T^3 e^{(-7000/T)}$, whereas the dark current increase due to bulk damage is

$T^2 e^{(-7000/T)}$. Hence, operating at T~-40°C is very important. Temperature stability is also very important to suppress drifts in the dark current.

In summary, since MOST is using a device operating in inversion, most of the dark current is suppressed. The total increase in dark current due to ionisation and bulk damage is on the order of 1 e^-/pixel/s.

6.1.2 Damaged Pixels

Frequently, displacement damage occurs in more than one place in the Si lattice in the same pixel. A high energy particle can bombard the first Si atom in the lattice, be deflected, but continue on its destructive path through the device. Also, if displacement damage occurs in the lattice in a region where there is a very strong electric field applied, then the pixel will show a very high generation rate due to a significant lowering of the potential barrier. Electrons will flood the pixel, making it appear lit. The volume of any pixel in a high field region is extremely small, so this is an unlikely effect (Robbins, private communication).

Marconi estimates that ~0.1% of pixels will display about 31,500 e^-/pixel/s due to damaged pixels after irradiation with 2 krad of 10 MeV equivalent protons. Although this is a very small number of pixels, the MOST data reduction algorithm needs to include a process for identifying pixels which consistently give a signal above a certain threshold, even when there is no light falling on that pixel. The lit pixels can effectively be removed from the data set, thus removing any noise due to the lit pixels.

6.1.3 RTS

Random Telegraph Signaling (RTS) is a more significant type of pixel damage that the MOST data reduction algorithm should be set to monitor. Although it is unclear what causes RTS (it does not appear to be created by nuclear interactions), it is definitely an effect seen in experiments performed on Marconi CCDs and evaluated by Robbins (2000). After significant proton irradiation, single pixels begin to show fluctuations in their signals, shifting from a low signal regime to a high signal regime. The amount of time spent in one regime is not well characterized. However, the average times between the discrete generation states is well defined by the following equation:

$$\frac{1}{\tau} = \mathrm{Re}^{\left(\frac{-E}{kT}\right)} \tag{6.2}$$

where τ is the average time in each state, R is a constant (~10^{13}-10^{14} /s), and E is a constant (0.9 ± 0.1 eV). The average time per state is strongly temperature dependent. At the MOST operating temperature (-40°C), the time constant is on the order of 6 days. About 6% of the pixels will display RTS after one year (i.e. 60,000 pixels will be damaged per 1 krad) and the effect will be enhanced in lit pixels.

Since the time constant for RTS is much longer than the oscillation periods that MOST is searching for in the stellar signal, this effect will not create aliases in the Fourier frequency regions of interest. However, since the actual time duration in each generation state is not well known, there could be photometric noise introduced in the region of interest when a pixel displaying RTS stays in one discrete state for a period of time significantly shorter than its time constant. Thus, the MOST data reduction algorithm needs to include a monitor for this effect, utilising onboard temperature sensor data to keep an accurate value for τ. Pixels displaying an RTS effect should be discarded completely or given values taken from an average of the surrounding pixels.

Although 6% is a large number of total pixels, the data that MOST uses only spans 6400 pixels (0.6% of the total chip). Thus, it is not likely that RTS will result in a major loss of data for MOST.

6.1.4 Flat Band Voltage Shifts

Flat band voltage shifts occur under ionising radiation damage. The lattice of the silicon dioxide insulating layer is not immune to interactions with charged particles. When an ionising particle hits the lattice in the insulting region, the high electric field tends to immediately sweep away any electrons, leaving electron-hole pairs (positive charge). After time, the electron hole pairs accumulate and congregate together. This effectively changes the operating potential of the MIS capacitor, increasing the potential by an amount equal to a flat band voltage shift.

Many experiments have been conducted on Marconi CCDs to investigate flat band voltage shifts. However, the majority of them are done on front illuminated devices. Since the insulating region is buried in a backside illuminated device, comparisons are not valid. However, CCD26, a Marconi backside illuminated device was tested for flat band voltage shifts and an increase of 100 ±20 mV/krad(Si) were found (c.f. Robbins 2000). Thus, MOST will likely experience ~100 mV voltage shift over the course of one year of operation. This may decrease the responsivity of the CCD, but is such a small shift that effects will be negligible over the first year of the mission (Johnson, private communication). If the mission lifetime is extended, the issue of a flat band voltage shift should be revisited.

6.1.5 CTE Degradation

CTE degradation occurs in response to bulk radiation damage. In response to a damaged Si lattice, deep trapping states are created, capable of trapping electrons. With time they congregate together. CTE is defined as the fraction of the signal when transferred from one pixel to the next. Charge Transfer Inefficiency (CTI) is the quantity (1–CTE).

It is known that CTI increases with smaller signals, an effect that is enhanced by radiation damage (Hardy 1997). Since MOST will observe some of the brightest stars in the sky, it is not expected that CTI will be a major obstacle.

Since CTI is a result of displacement damage, it scales with non-ionising energy loss (NIEL), or the amount of energy deposited by a charged particle through any process other than ionisation (usually nuclear interactions). Robbins (2000) confirms that NIEL is a good first approximation. NIEL can be calculated using a model developed by the European Space Research and Technology Center and available online through the Space Environment Information System (SPENVIS, http://www.spenvis.oma.be/spenvis/). For the MOST baseline orbit, NIEL in Silicon as a function of spherical Al shielding is shown in Figure 6.3.

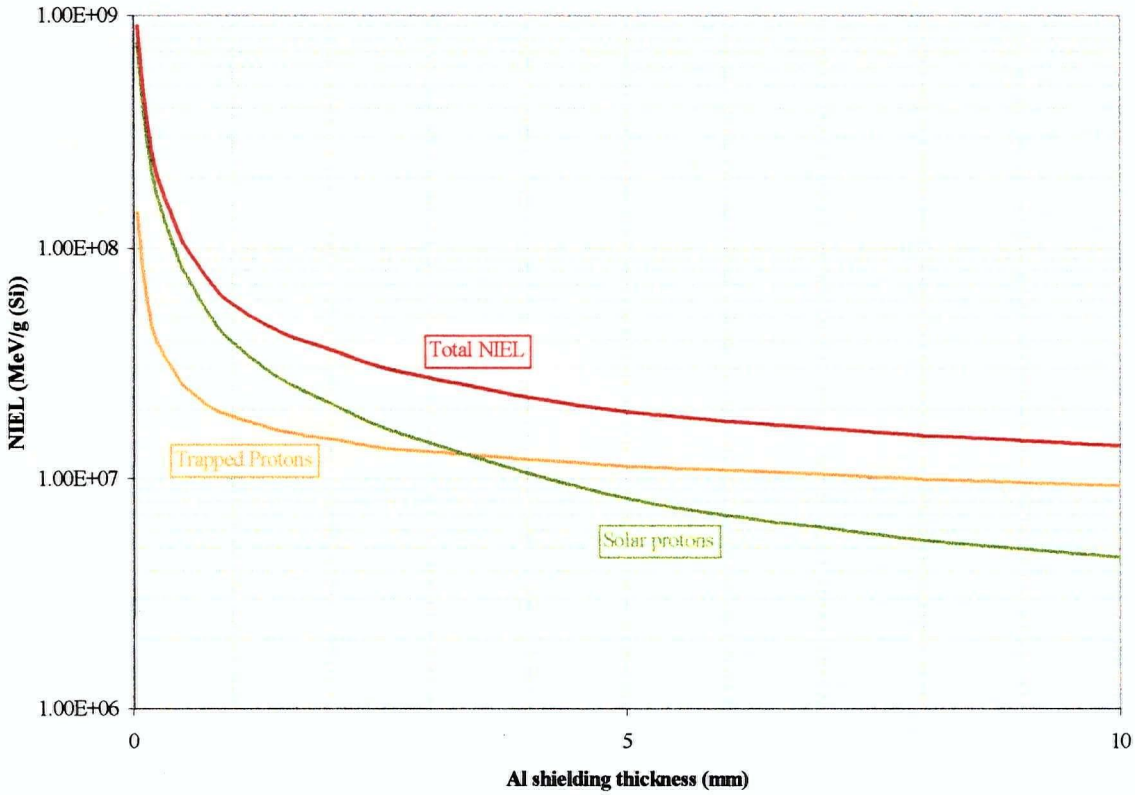

Figure 6.3 Non-ionising energy loss as a function of spherical Aluminum shielding thickness.

The scaling factor used to estimate CTI from NIEL is usually determined experimentally. Since radiation testing of the CCDs was not done as part of this analysis, an arbitrary scaling constant of 1×10^{-11} g(Si)/MeV was chosen based on Dale (1993). It is probably an overestimate of the actual factor and hence, the results presented here are expected to be an overestimation of the actual CTI. The scaling factor can be refined if radiation testing is ever performed on the MOST CCDs.

For 5 mm of spherical Al shielding, the NIEL is 1.97×10^{7} MeV/g(Si), and the relative degradation in CTE over the course of a 1 year mission in the MOST baseline orbit is 1.97×10^{-4}. Thus, after one year, the lowest measured CTE of the MOST science grade CCD will be degraded to 0.999799%.

6.1.6 Implications for the Photometric Error Budget

In summary, the following 'worst case' scenario may occur to the MOST CCD during the first year of operations:

a) Dark current increases to ~ 16 e^-/pixel/s;
b) RTS/Damaged pixels remove ~6% of pixels from functioning;
c) CTE is degraded to 99.999799%;
d) and Reduction of duty cycle to 80% (Section 4.4).

Kuschnig (2000) has incorporated these values into numerical simulations of the MOST microsatellite. Even after radiation damage combined with all other noise sources, the simulations show that MOST will be able to observe oscillations on the order of a few ppm (Kuschnig, private communication 2000).

6.2 Single Event Effects (SEEs)

SEEs differ from ionising and bulk damage effects because they are non-cumulative. The broadest definition of a single event covers all energetic particle interactions with a device which cause an observable effect. In general, SEEs are caused by an energy transfer from the charged particle to Silicon or Silicon dioxide in microelectronics (or Gallium Arsenide in solar panels). These effects can occur in any electronics system or computer device and are not limited to the CCD. Multi-Oxide-Semiconductors (MOS) devices are particularly sensitive to such effects, especially field effect transistors (MOSFETs) which are a common circuit element. Other parts which may experience upsets include the digital signal processor, solar cells, memory devices, logic circuits, and other sensitive circuit nodes. The primary effects that a charged particle can cause include (Label 1997):

- A Single Event Upset (SEU) occurs when the charged particle causes a bit flip in a memory device (a binary transition from 0 to 1 or vice versa).
- A Single Hard Error (SHE) occurs when a SEE causes permanent damage in one bit of memory.

- A Single Event Functional Interrupt (SEFI) occurs when a SEU causes a string of code to be read incorrectly, causing temporary interruption of normal system performance.
- A Single Event Latchup (SEL) occurs in circuits when the energy deposition causes a burst in current causing a burn-out in that circuit. It is potentially catastrophic.
- A Single Event Burnout (SEB) is a highly localized SEL which causes a burnout in the drain source of MOSFETS associated with power generation.
- The MOSFETs are also sensitive to Single Event Gate Rupture (SEGR) when the charged particle interacts with an oxide gate layer, causing destruction and possible failure.

Although it is possible to calculate the number of interactions a device will have per day, or per orbit, it is not possible to predict which of the above effects it will cause. The catastrophic effects are less common, only because the volumes of material sensitive to that type of effect are small.

Integrated circuits are also susceptible to SEEs, depending on how the circuit board is manufactured. Devices manufactured on bulk substrate are highly susceptible to SEUs because circuit junctions are connected to the substrate (Johnston 1996). If the circuit is manufactured such that junction is isolated from the substrate so it can not build up electrons gathered within the substrate itself, then it is less sensitive to the radiation environment. This is accomplished using an epitaxial layering process to insulate the junctions from the surrounding material. Junctions can also be isolated in special oxides to prevent charge buildup. These latter processes are more expensive than the first, but worth the cost.

Whether an SEE happens depends both on the incoming particle's energy and on the susceptibility of the device it interacts with. The number of proton-induced upsets in a device can be calculated using a semi-empirical Bendel & Petersen 2-parameter model (Petersen 1996). This model is appropriate only for Si devices. In a similar fashion to the radiation environment models, the basis of the relationships were found applying particle interaction theories, but the coefficients and overall formulae were developed by comparing theory to actual data.

The 2 parameters in the Bendel & Petersen model relate to the cross section for proton upset in the following way:

$$\sigma = 10^{-12}\left(\frac{B}{A}\right)^{14}\left(1-e^{0.18\left(\sqrt{\frac{18}{A}}(E-A)\right)^{\frac{1}{2}}}\right)^{4} \qquad (6.3)$$

where σ is the cross section for proton upsets in cm^2/bit, B and A are the Bendel parameters in MeV, and E is the particle's energy in MeV (Petersen 1996). The cross section for upset, integrated with the energy spectra of the proton environment yields the number of upsets, or SEE rate. The term $(B/A)^{14}$ effectively describe the "limiting cross section" of the device. It is the value which best fits the device's cross section for susceptibility to a particle with infinite energy, or the maximum cross section for the device. These parameters are extremely device-dependent. On a series of parts tested by Stapor et al. (1990), both A and B ranged from about 5 - 50 MeV. However, for a given device, A and B are within a few MeV of each other. If A was low, then B was also low.

The standard method of testing a part for its durability in the cocktail of particles associated with the orbital environment is to perform ground based tests on engineering grade devices. In order to find the Bendel Parameters for a given device, the cross sections are found experimentally, usually by irradiating the device with protons at only 1 or 2 energies (as accelerator time is expensive!). From the cross section, the data are least square fit to the model and A and B are found. Alternatively, one can buy parts that are specifically designed for space and have a low susceptibility to the environment.

No ground-based testing has yet been performed on MOST parts. Hence, Figure 6.4 shows the proton induced SEU rate per day as a function of both A and B. Since the majority of tests on various electronics show that A~B, the SEU rate will likely be on the order of 1×10^{-6} SEU/day. Only radiation testing can confirm this.

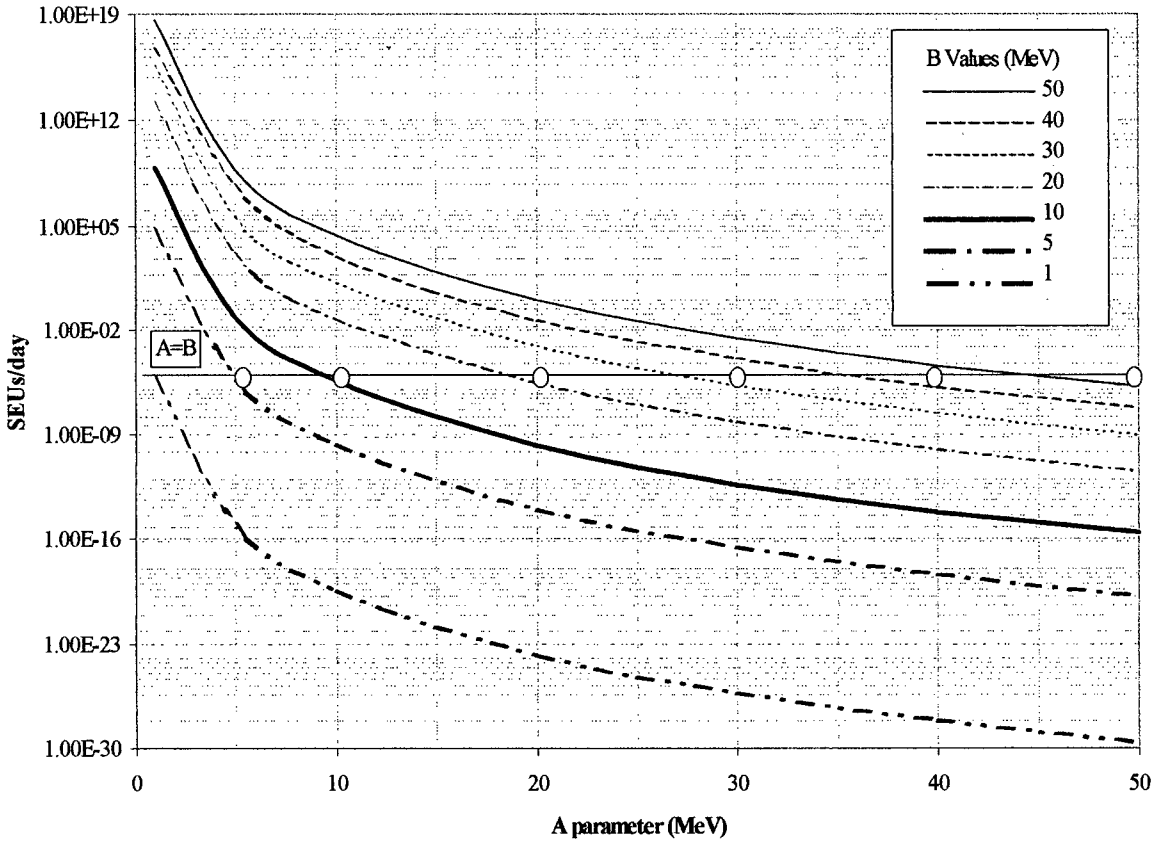

Figure 6.4 Proton induced single event effect rate as a function of Bendel and Petersen model parameters A and B for the MOST baseline orbit radiation environment.

Single event effects can also be caused by heavy ions. Since the nuclear interactions are different, a different model is used to describe the number of SEEs they may cause. Though the flux of heavy ions is much less than the proton flux, the particles are much more penetrating through the magnetosphere and spacecraft shielding because of their heavier masses and hence, may play as large, if not a larger role in the number of upsets a spacecraft experiences.

This analysis employs the Pickel and Blanford model for heavy ion upset (Pickel 1996), since it is already integrated into SPACE RADIATION 4.0. The model requires knowledge of the sensitive region of the semiconductor device, and the flux of the ions that may hit the sensitive area. The device is described in terms of the sensitive volume

($dx \times dy \times dz$) and the critical charge (Q). The critical charge is the minimum charge that must be built up in device in order to cause an effect, such as an SEU. The lower the critical charge, the easier it is to cause an upset. Q is given by 6.4:

$$Q = \{f\}LET(dz) \tag{6.4}$$

where {f} is a function of the material properties of the device, LET is the Linear Energy Transfer (LET) threshold (i.e. the minimum energy which the incident particle must have in order to confer any charge to the device through ionisation), and dz is the depth to which the device is sensitive. $\{f\}$ for Si is 0.0103, for SiO_2 it is 0.00196, and for GaAs it is 0.0177.

Again, radiation testing of the device is needed to determine the LET threshold as well as the sensitive depth. Sensitive volume can be estimated by knowing the structure of the device and making assumptions about its workings (Johnston, 1996). Since radiation testing has not been done on the majority of the MOST electronics, Figure 6.5 shows the upsets/bit/day for the MOST baseline orbit for a range of sensitive volume as a function of critical charge, and two different volume dimensions.

From figure 6.5 it is apparent that there is a plateau in the number of upsets a device experiences at low critical charges. This occurs because the device essentially saturates if exposed to more charge. At the high limit of critical charge, the curves show a very steep drop off. This makes sense, as very few particles will have sufficient energy to actually induce sufficient charge in the device to cause an effect, if the critical charge exceeds about .01 pC.

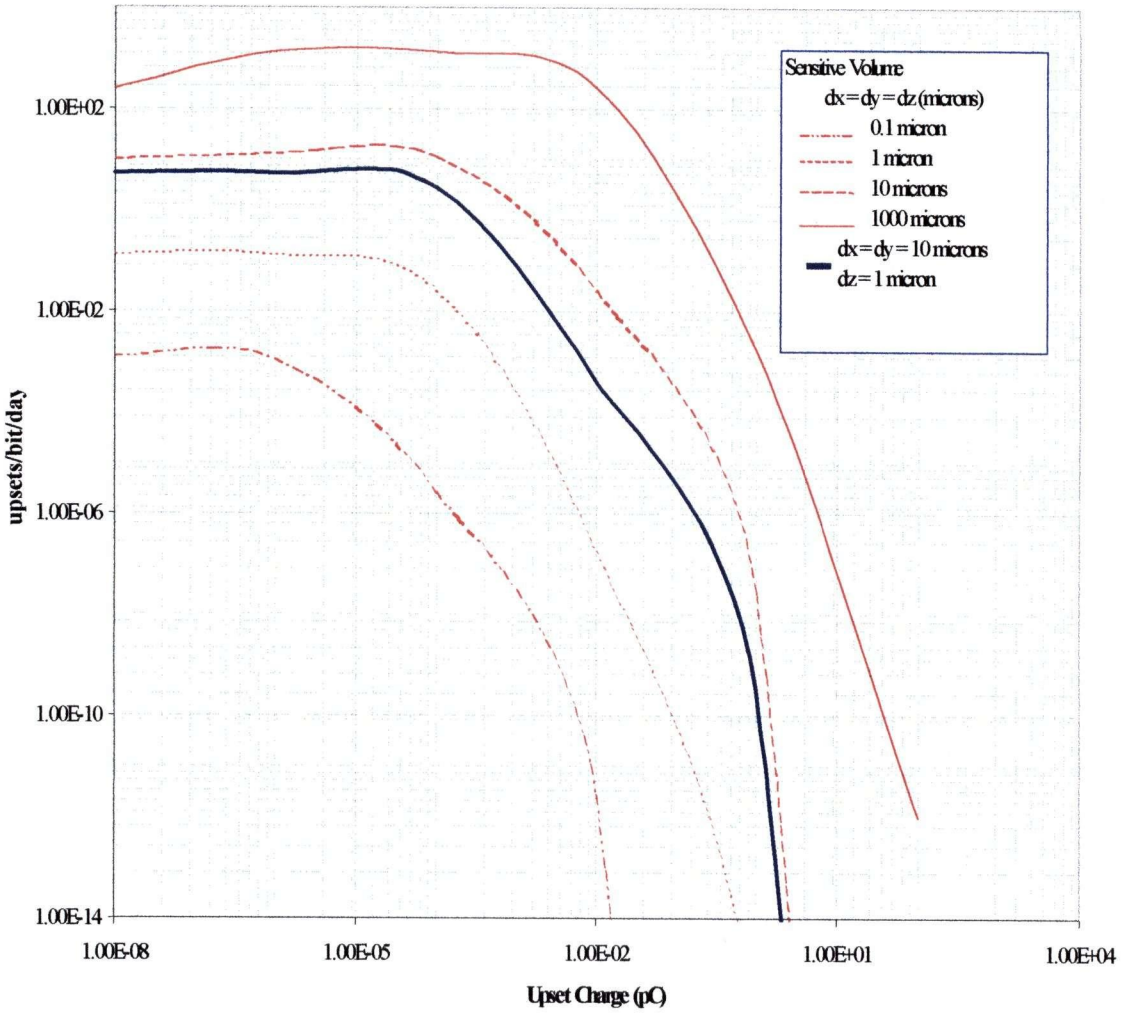

Figure 6.5 Heavy ion induced upsets for the MOST baseline orbit for a range of sensitive volume as a function of critical charge.

As the sensitive volume of the device increases, so does the upset rate. Sensitive volumes are likely not cubical as presented in Figure 6.5, but will have some rectangular shape. The depth of penetration of particles will define the direction *dz*, so realistically, *dz* will be smaller than the surface area of the device. The heavy blue line indicates this scenario. The results do not differ significantly from a symmetric cube with the same sensitive volume.

Each device which is integrated into the MOST microsatellite should be compared to the above diagram. The following questions about the device should be answered:

- What is the sensitive volume of the device?
- Will the device experience excessive upsets?
- How does the device affect other systems?

The latter question is perhaps the most important (provided the device does experience upsets). In considering any risk factor for a space mission, there is a constant battle between cost, efficiency (mass budget, delivery schedule, etc...) and risk. When is the risk great enough to warrant spending more money on a specific part? Thus, the devices themselves are not the only important piece of the puzzle. How they interact with the other systems, and what implications their failure could have on other systems will mitigate whether or not they should be flown.

Since comprehensive radiation testing has not been done, and device specifications are not currently available, it is not possible to provide a further estimate of the single event rate. Once these values are known, a complete assessment of the single effect effects can be made. All devices utilised should be radiation hardened.

Chapter 7: Mitigation of environmental damage

The radiation environment of the MOST microsatellite has been evaluated using SPACE RADIATION 4.0, to find yearly ionising doses and displacement damage. The radiation environment will slowly degrade the CCD detector in the following way:

a) dark current will increase by about 1 e^-/pixel/s over the course of one year,

b) CTE will be degraded to 99.99799% from 99.99999% over the course of one year,

c) 6% of pixels will be damages or display RTS, and

d) the detector will experience a flat-band voltage shift on the order of a few mV per year.

Other on-board microelectronics will be susceptible to Single Event Effects. Radiation testing of sensitive devices and circuits is needed to further quantify the SEE rate. The majority of these effects occur as the satellite passes through the charged particle rich region of the SAA. Thus, the combined effect may cause MOST to experience a temporary loss of data while in the densest parts of the SAA. This reduction in duty cycle will create aliases in the data set.

7.1 Recommendations for the MOST Microsatellite

The following recommendations have been made to mitigate the effects of the radiation environment on the MOST microsatellite:

a) The satellite needs a minimum of 5mm of Al shielding. Current design has about 8 mm of Invar shielding from the telescope structure itself. Excessive shielding may induce secondary reactions which may cause as much damage as primary interactions (Dyer et al. 1996). Thus, shielding should not be increased.

b) Cosmic ray hits should be removed from the MOST data set and pixel values replaced by the mean of the surrounding pixel values, or discarded.

c) The MOST data reduction algorithm should include a filter for pixels displaying Random Telegraph Signaling (RTS) using the average lifetime in the high signal

generation state vs. low state as the distinguishing signal of RTS and discard any pixels showing this effect.

d) The boundary of the SAA measured by the FUSE satellite team should be utilized to filter data taken during passage through the SAA. The data taken during this time should be analyzed and compared to the predictions presented in this study to further validate the models.

e) The satellite should not be launched into a higher altitude orbit due to the increased expanse of the SAA at higher altitudes.

7.2 Other Asteroseismology Missions

MOST will be followed by two other space satellite missions also aiming to study stars through asteroseismology: COROT and MONS. COROT has a baseline orbit similar to that of MOST with a 900 km altitude and 99.5° inclination. The primary difference is that the satellite will be in an inertial orbit so it constantly faces one half of the sky. The MONS baseline orbit is a Molniya type orbit, a highly eccentric (E=0.741) orbit with a semi major access of 26560 and an inclination of 63.4°. MONS will spend a great deal of its time far from the Earth and so, will have access to a great portion of the sky. However, it will also be outside of geomagnetic shielding and be very exposed to Solar Energetic Particles (SEPs). A comparison of the dose vs. depth curves for the three missions shows that with 5mm of spherical Al shielding, MOST and COROT will experience about equivalent doses (Figure 7.1). MONS will need to shield sensitive components with up to 10 mm of Al in order to bring down their cumulative ionising doses to a level safe for most devices. COROT has a curve slightly lower than the MOST dose vs. depth curve because the inclination of the orbit is slightly greater, and hence it experiences greater geomagnetic shielding.

Since MOST is the first of the three missions scheduled for launch, it will really be the test of concept for the other two missions. Experiences faced by the MOST microsatellite should be used by the other satellite teams in perfecting their design to withstand the orbital environment in order to perform asteroseismology.

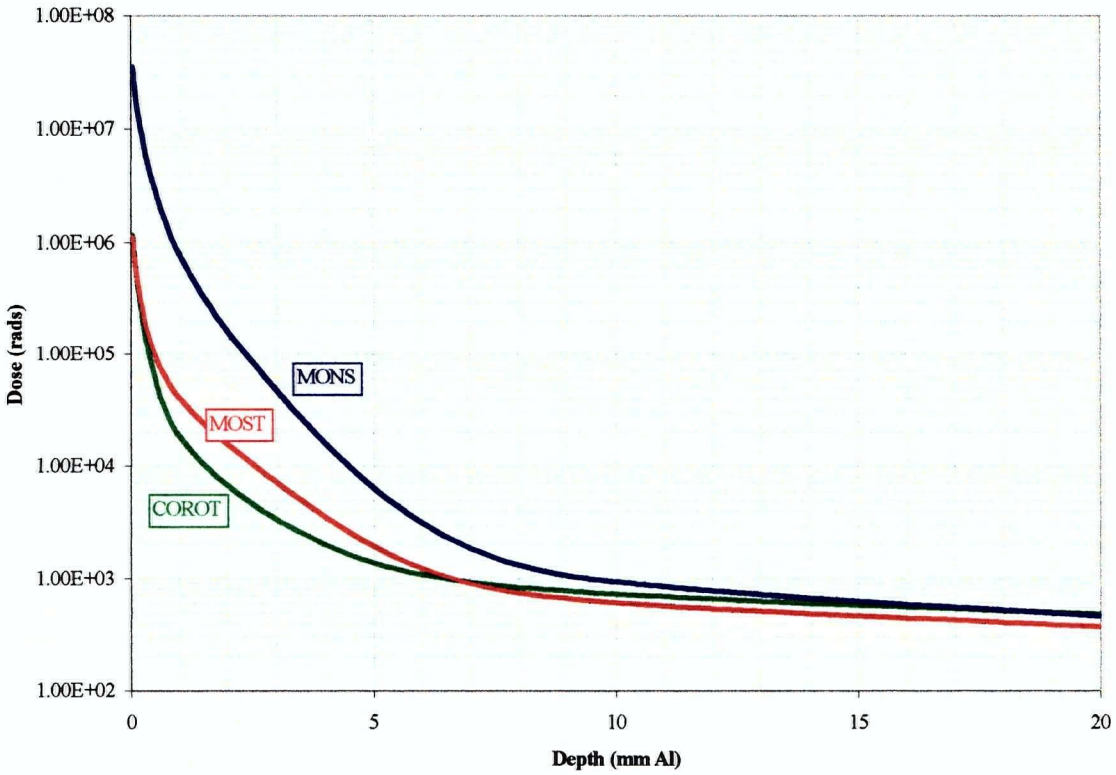

Figure 7.1 Ionising doses for the MOST (red), MONS (blue), and COROT (green) satellite missions as a function of spherical Al shielding thickness. Models are identical, for flight epochs in 2002.

7.3 Future Work

Although it has been determined that the radiation environment will not impede the sensitivity of the MOST detector over the course of the baseline mission lifetime, there are other effects due to the radiation environment which should be considered prior to launch. Spacecraft charging is a common phenomenon. Particles hit the satellite, and buildup in metallic reservoirs, a process known as di-electric charging. If the charge becomes sufficiently high, arcing will occur, and parts of the satellite may be permanently damaged.

Radiation testing of sensitive components to experimentally determine the proton upset cross sections and thus, Bendel parameters should be undertaken. If accelerator time is deemed too expensive, then an alternate fixed source (such as Cobalt^{60}) can be

used to simulate the radiation environment. Sensitive volumes of all microelectronics should be considered in order to quantify the Single Event Upset rate. In learning from a previous space satellite with Canadian involvement, FUSE, there were many more SEUs than anticipated. In fact, FUSE must uplink on board command sequences after every pass through the SAA. Since MOST will not have access to as complete a network of ground stations as FUSE, a significant attempt to reduce the SEU rate should be made.

References:

Alpert, M., 2000, Fire in the Sky: Space weather turns gusty as solar activity approaches its peak, Scientific American, July 2000

Badhwar, G.D., O'Neill, M., 1996, Galactic Cosmic Radiation Model and its Applications, Adv. Space Res., V. 17, No. 2, pp. 7-17

Bailey, P., 1993, Radiation Damage Effects in EEV CCDs, CCD Technical Note 12, EEV limited

Barth, J., 1997, NSREC Short Course: Applying Computer Simulation Tools to Radiaion Effects Problems, 1997 IEEE Nuclear and Space Radiation Effects Conference

Beaujean, R., Barz, S., Jonathal, D., Enge, W., 1996, On the Origin of Trapped Heavy Ions at L=1.4-1.6, Adv. Space Res., V. 17, No. 2, pp. 167-170

Buzasi, D., Catanzarite, J., Laher, R., Conrow, T., Shupe, D., Gautier, T. N., III, Kreidl, T., Everett, D., 2000, The Detection of Multimodal Oscillations on α Ursae Majoris, The Astrophysical Journal, V. 532, No. 2, pp. L133-L136

Chapman, S., Bartels, J., 1940, Geomagnetism, vols 1 and 2. 1049 pp. Oxford: Oxford University Press, Clarendon Press

Cronin, J.W., Gaisser, T.K., Swordy, S.P., 1997, Cosmic Rays at the Energy Fronteir, Scientific American, January 1997

Demarque, P., Guenther, D.B., 1999, Helioseismology: Probing the interior of a star, Proc. Natl. Acad. Sci., V. 96, pp. 5356-5359

Dyer, C.S., Truscott, P.R., Peerless, C.L., Watson, C.J., Evans, H.E., Knight, P., Cosby, M., Underwood, C., Cousins, T., Noulty, 1998, Updated Measurements from CREAM and CREDO and Implications for Environment and Shielding Models, IEEE Transactions on Nuclear Science, V. 45, No. 3, pp. 1584-1589

Dyer, C.S., Truscott, P.R., Peerless, C.L., Watson, C.J., Evans, H.E., Knight, P., Cosby, M., Underwood, C., Cousins, T., Noulty, R., Maag, C., 1999, Implications for space radiation environment models from CREME & CREDO measurements over half a solar cycle, Radiation Measurements, V. 30, pp. 569-578

Feynmann, J., Armstrong, T.P., Dao-Gibner, L., Silverman, S., 1990, New Interplanetary Proton Fluence Model, Journal of Spacecrafts, V. 27, No. 16, pp. 403-410

Feynmann, J., Spitale, Wang, 1993, Journal of Geophysical Research, V. 98, pp. 13281-13294

Gasser, T.K., 1990, Cosmic Rays and Particle Physics, Cambridge University Press, New York

Gussenhoven, M.S., Mullen, E.G., 1993, Space Radiation Effects Program: An Overview, IEEE Transactions on Nuclear Science, V. 40, No. 2, pp. 221 - 227

Hedin, A. E., 1991, Extension of the MSIS Thermospheric Model into the Middle and Lower Atmosphere, *J. Geophys. Res.*, V. *96*, p.1159

Huston, S.L., Kuck, G.A., Pfitzer, K.A., 1998, Solar Cycle Variation of the low-Altitude Trapped Proton Flux, Adv. Space Res., V. 21, No. 12, pp.1625-1634

Jenkins, J.M., Borucky, W.J., Dunham, E.W., McDonald, J.S., 1996, High Precision Photometry with Back-Illuminated CCDs, Planets Beyond Our Solar System and Next Generation Space Missions, ASP Conference Series, conference proceedings

Johnston, A., 1996, Effects in Electronic Devices and SEE Rates, In Single Event Effect Criticacality Analysis, NASA, Code QW

King, J.H., 1974, Solar Proton Fluences for 1977-1983 Space Missions, Journal of Spacecraft and Rockets, V. 11, no. 6, pp. 401-408

Klecker, B., 1996, Energetic Particle Environment in Near-Earth Orbit, Advances in Space Research, Vol 17, No. 2, pp. 37-45

Krischiunas, K., Sinton, W., Tholen, D., Tokunaga, A., Golisch, W., Griep, D., Kaminski, C., Impey, C., Christian, C., 1987, Atmospheric Extinction and Night-Sky Brightness at Mauna Kea, Publications of the Astronomical Society of the Pacific, V. 99, pp. 887-894

Kuchner M.J., Brown, M.E., 2000, A Search for Exozodiacal Dust and Faint Companions Near Sirius, Procyon, and Altair with the NICMOS Coronograph, astro-ph/0002043

Kuschnig, R., 2000, in preparation

Label, K., 1996, Single Event Effects Criticality Analysis, NASA Code QW

Lauriente, M., Vampola, A.L., Gosier, K., 1996, Experimental Validation of South Atlantic Anomaly Motion Using a Two-Dimensional Cross-Correlation Technique, *in* Lemaire, J.F., Heynderickx, D., Baker, D.N. (eds), Radiation Belts: Models and Standards, Geophysical Monograph Series 1997, American Geophysical Union, 1996

Mandea, M., Macmillan, S., Bondar, R., Golovkov, V., Langlais, B., Lowes, F., Olsen, N., Quinn, J., Sabaka, T., 2000, International Geomagnetic Reference Field - 2000:

International Association of Geomagnetism and Aeronomy (IAGA), Division V, Working Group 8, Physics of the Earth and Planetary Interiors, V. 120, pp. 39-42

Matthews, J.M., 1990, Good Vibrations from the Stars, New Scientist, V.27, pp. 46-50

Matthews, J.M., 1997, MOST Phase A report, Dynacon Document 97

Matthews, J.M., Kuschnig, R., 2000a, Numerical Simulation of Photometry, Most Document, MOST-UBC-0004/002

Matthews, J.M., Kuschnig, R., 2000b, Science Operations Guide, Most Document, MOST-UBC-0005/7

McIlwain, Carl E., 1961, Coordinates for Mapping the Distribution of Magnetically Trapped Particles, Journal of Geophysical Research, V. 66, No. 11

Panasyuk, M.I., 1996, Empirical Models of Terrestrial Trapped Radiation, Adv. Space Res, V. 17, No. 2, pp. 37-45

Robbins, M., 2000, The Radiation Damage Performance of Marconi CCDs, Technical Note, Marconi Document, S&C 906/424

Rigault, F., Dalmon, D., Arsenault, R., Thomas, J., Lai, O., Rouan, D., Veran, J.P., Gigan, P., Crampton, D., Flethcher, J.M., Stilburn, J., 1998, Performance of the Canada-France-Hawaii Telescope Adaptive Optics Bonnette, Publications of the Astronomical Society of the Pacific, 110: 152-164, February

Tassoul, M., 1990, Astrophysical Journal, V. 358, p. 313

Tylka, A.J., Adams, J.H.Jr., Boberg, P.R., Brownstein, B., Deitreich, W., Flueckiger, E.O., Petersen, E.L., Shea, M., Smart, D.F., Smith, E.C., 1997, CREME96: A Revision of the Cosmic Ray Effects on Micro-Electronics Code, IEEE Tans. Nucl. Sci, V. 18, p. 9499

Van Allen, James A., 1983, Origins of Magnetospheric Physics, Smithsonian Institution Press, Washington D.C.

Vette, J.I., 1966, Models of the Trapped Radiation Environment, V1-7, NASA, Washington

Walt, M., 1994, Introduction to Geomagnetically Trapped Radiation, Cambridge University Press, Cambride

Walt, M., 1996, Source and Loss Processes for Radiation Belt Processes, in Lemaire, J.F., Heynderickx, D., Baker, D.N. (eds), Radiation Belts: Models and Standards, Geophysical Monograph 97, American Geophysical Union, Washington DC

Watson, C.J., Dyer, C.S., Truscott, P.R., Peerless, C.L., Sims, A. J., Barth, J.L., 1998, The Low Earth Orbit Environment Observed using CREAM and CREDO, Advances in Space Research, V. 21, No., 12, pp 1621-1624

Appendix A: Selected MOST Target Stars

	RA hh:	mm:	ss	DEC deg	mm:	ss	RA deg	DEC deg	Proper Motion RA	DEC	Mag. V	B
Solar-Type Stars												
Procyon	7	39	20.44	5	14	21.22	114.83517	8.5884167	-0.712	-1.029	0.34	0.74
Beta Gem	7	45	21.259	28	1	36.61	116.33858	28.402542	-0.628	-0.071	1.15	2.15
Gam Leo A	10	19	57.2	19	50	37.34	154.98833	31.655583	0.307	-0.152	2.61	3.76
Eta Boo	13	54	41.217	18	24	9.72	208.67174	24.0405	-0.064	-0.363	2.68	3.26
Gam Vir	12	41	41.407	-1	-26	-58.08	190.42253	-7.742	-0.567	0.004	3.65	4.01
Bet Her	16	30	13.465	21	29	23.27	247.5561	28.346958	-0.099	-0.017	2.77	3.71
Bet Oph	17	43	28.398	4	33	54.25	265.86833	12.476042	-0.042	0.159	2.77	3.93
Zet Her	16	41	18.996	31	35	50.87	250.32915	39.961958	-0.552	0.386	2.81	3.46
Eps Vir	13	2	11.454	10	57	32.1	195.54773	24.38375	-0.275	0.017	2.83	3.77
Subdwarf												
HD224930	0	2	7	27	5	44.9	0.5291667	28.437083	0.841	-0.985	5.75	6.42
HD 76932	8	58	43.01	-16	-8	-8.1	134.67921	-18.03375	0.234	0.214	5.86	6.39
Ro-Aps												
HR1217	3	55	16.4	-12	-5	-55.4	58.818333	-13.480833	-0.062	-0.039	6	6.32
gam Equ	21	10	20.251	10	8	0.99	317.58438	12.004125	0.061	-0.14	4.69	4.95
HD176232	18	58	46.82	13	54	26.2	284.69508	26.609167	-0.008	-0.044	5.9	6.14
Wolf-Rayets												
WR 113	18	19	7.22	-11	-37	-58.8	274.78008	-20.495	-0.022	0.015	9.43	9.86
WR 128	19	48	32.1	8	12	6	297.13375	11.025			10.5	10.51
WR 123	19	3	59	-4	-49	0	285.99583	-16.25			11.27	11.74

Appendix B: Orbital Parameters

MOST Baseline Orbit:

- Altitutde: 800 km
- Inclination: 98.6°
- Orbital Period: 1.86 hours
- Duration: 1 orbit
- Date: 12/01/2000
- Start time: 0h 0min 0.00s
- Magnetic Field Model: IGRF1995
- Orbital Epoch: 2002
- Colatitude of the dipole pole: 10.47°
- Longitude of the dipole pole: -71.8°
- Dipole tilt angle: -25.2°

TIME (h)	LON. (°)	LAT.(°)	ALTITUDE (km)	B	L
0	269.6	0	800	0.217036	1.2049
0.02	268.8	3.5	800.1	0.227873	1.2336
0.03	268	7.1	800.3	0.240166	1.2726
0.05	267.2	10.6	800.6	0.253634	1.3236
0.07	266.4	14.2	801	0.267975	1.3883
0.08	265.6	17.7	801.5	0.282875	1.4694
0.1	264.8	21.3	802.2	0.298027	1.5698
0.12	263.9	24.8	802.9	0.313136	1.6939
0.13	263	28.3	803.7	0.327923	1.8472
0.15	262	31.9	804.6	0.342131	2.0376
0.17	261	35.4	805.5	0.355521	2.275
0.18	259.9	38.9	806.5	0.36787	2.5739
0.2	258.7	42.4	807.4	0.378973	2.9539
0.22	257.4	45.9	808.4	0.388643	3.4432
0.23	256	49.4	809.4	0.396727	4.0824
0.25	254.4	52.8	810.3	0.403119	4.9313
0.27	252.6	56.3	811.2	0.40778	6.0772
0.28	250.4	59.7	812	0.410761	7.6498
0.3	247.9	63.1	812.7	0.412213	9.834
0.32	244.7	66.4	813.4	0.412392	>10
0.33	240.6	69.7	813.9	0.411646	>10
0.35	235.2	72.8	814.3	0.410388	>10

0.37	227.7	75.8	814.7	0.40905	>10
0.38	216.7	78.4	814.8	0.408027	>10
0.4	200.5	80.4	814.9	0.407625	>10
0.42	178.5	81.4	814.8	0.408015	>10
0.43	155	81	814.5	0.409203	>10
0.45	136.1	79.4	814.2	0.411034	>10
0.47	123.1	76.9	813.6	0.41321	10.0863
0.48	114.3	74.1	813	0.415339	7.845
0.5	108.1	71	812.3	0.416985	6.2161
0.52	103.5	67.8	811.4	0.417721	5.0191
0.53	100	64.5	810.4	0.417171	4.1259
0.55	97.2	61.1	809.4	0.415043	3.4492
0.57	94.9	57.7	808.2	0.411148	2.9286
0.58	93	54.3	807	0.405402	2.523
0.6	91.3	50.8	805.8	0.397825	2.2032
0.62	89.8	47.4	804.6	0.388526	1.9488
0.63	88.4	43.9	803.3	0.377693	1.7452
0.65	87.2	40.4	802.1	0.365581	1.5811
0.67	86.1	36.9	800.9	0.352503	1.449
0.68	85	33.3	799.7	0.338827	1.3427
0.7	84.1	29.8	798.6	0.324976	1.2576
0.72	83.1	26.3	797.5	0.311431	1.1905
0.73	82.2	22.7	796.6	0.298722	1.1387
0.75	81.4	19.2	795.8	0.287411	1.1003
0.77	80.5	15.6	795.1	0.278047	1.0739
0.78	79.7	12.1	794.5	0.271103	1.0585
0.8	78.9	8.5	794.1	0.266888	1.0535
0.82	78.1	5	793.8	0.265479	1.0586
0.83	77.3	1.4	793.7	0.26669	1.0739
0.85	76.5	-2.1	793.7	0.270099	1.1002
0.87	75.8	-5.7	793.9	0.275124	1.1382
0.88	75	-9.2	794.2	0.281127	1.1893
0.9	74.2	-12.8	794.6	0.287504	1.2553
0.92	73.3	-16.3	795.2	0.293757	1.3383
0.93	72.5	-19.9	796	0.299521	1.4412
0.95	71.6	-23.4	796.8	0.304578	1.5674
0.97	70.7	-27	797.8	0.308835	1.7214
0.98	69.8	-30.5	798.8	0.312301	1.9082
1	68.8	-34	800	0.315058	2.1347
1.02	67.7	-37.6	801.1	0.317225	2.4086

1.03	66.6	-41.1	802.4	0.31894	2.7403
1.05	65.3	-44.6	803.6	0.320339	3.1415
1.07	64	-48.1	804.9	0.321552	3.6258
1.08	62.4	-51.5	806.1	0.322699	4.2084
1.1	60.7	-55	807.3	0.323889	4.9028
1.12	58.7	-58.4	808.5	0.325223	5.7166
1.13	56.3	-61.8	809.6	0.326784	6.6417
1.15	53.4	-65.2	810.7	0.328629	7.6385
1.17	49.7	-68.5	811.6	0.330772	8.618
1.18	44.9	-71.6	812.5	0.333169	9.4342
1.2	38.3	-74.7	813.2	0.335707	9.9106
1.22	28.7	-77.5	813.8	0.338201	9.9137
1.23	14.7	-79.8	814.3	0.340407	9.4315
1.25	354.6	-81.2	814.6	0.342044	8.5855
1.27	330.9	-81.3	814.8	0.34283	7.5619
1.28	309.9	-80.1	814.9	0.342513	6.5251
1.3	294.8	-77.9	814.8	0.340913	5.5772
1.32	284.6	-75.2	814.6	0.337942	4.7614
1.33	277.6	-72.2	814.3	0.333611	4.0834
1.35	272.5	-69	813.9	0.328033	3.5302
1.37	268.6	-65.8	813.3	0.321395	3.0824
1.38	265.6	-62.4	812.6	0.313929	2.7203
1.4	263.1	-59	811.9	0.305877	2.4266
1.42	261.1	-55.6	811	0.297459	2.1875
1.43	259.3	-52.2	810.2	0.28885	1.991
1.45	257.7	-48.7	809.2	0.280172	1.8285
1.47	256.3	-45.2	808.2	0.271503	1.6934
1.48	255.1	-41.7	807.3	0.262893	1.5804
1.5	253.9	-38.2	806.3	0.254396	1.4856
1.52	252.8	-34.7	805.3	0.246092	1.4061
1.53	251.8	-31.2	804.4	0.238109	1.3396
1.55	250.9	-27.6	803.5	0.230633	1.2845
1.57	250	-24.1	802.7	0.2239	1.2394
1.58	249.1	-20.6	802	0.218193	1.2035
1.6	248.3	-17	801.4	0.21381	1.1758
1.62	247.4	-13.5	800.9	0.211041	1.1558
1.63	246.6	-9.9	800.5	0.210135	1.1436
1.65	245.8	-6.4	800.2	0.211271	1.1387
1.67	245	-2.9	800.1	0.21452	1.1413
1.68	244.3	0.7	800	0.219871	1.1518

1.7	243.5	4.2	800	0.227162	1.171
1.72	242.7	7.8	800.3	0.236166	1.1995
1.73	241.9	11.3	800.6	0.246593	1.2383
1.75	241.1	14.9	801	0.258124	1.2888
1.77	240.2	18.4	801.6	0.270451	1.3526
1.78	239.4	22	802.2	0.283289	1.4319
1.8	238.5	25.5	803	0.296393	1.5294
1.82	237.6	29	803.8	0.309547	1.6489
1.83	236.6	32.6	804.7	0.322551	1.7953
1.85	235.6	36.1	805.6	0.335209	1.9746

Appendix C: Selected Target Star Dwell Time in the CVZ

(Time in weeks)

Solar Type Stars:

Inclination	Altitude	Radius of CVZ	Procyon	Beta Gem	Gam Leo A	Eta Boo	Gam Vir	Bet Her	Bet Oph	Zet Her	Eps Vir
			8.6	28.4	31.7	24.0	-7.7	28.3	12.5	40.0	24.4
96.0	101.4	10.1	2.8	0.0	0.0	0.0	0.0	0.0	2.3	0.0	0.0
96.2	162.1	12.8	3.6	0.0	0.0	0.0	0.0	0.0	3.2	0.0	0.0
96.4	221.5	14.9	4.3	0.0	0.0	0.0	1.3	0.0	3.9	0.0	0.0
96.6	279.5	16.7	4.8	0.0	0.0	0.0	2.5	0.0	4.5	0.0	0.0
96.8	336.3	18.2	5.3	0.0	0.0	1.7	3.2	0.0	5.0	0.0	1.4
97.0	391.9	19.6	5.7	0.0	0.0	2.8	3.7	0.0	5.5	0.0	2.6
97.2	446.3	20.8	6.0	0.0	0.0	3.6	4.2	0.0	5.8	0.0	3.4
97.4	499.6	22.0	6.4	1.9	0.0	4.2	4.6	1.9	6.2	0.0	4.0
97.6	551.9	23.0	6.7	2.9	0.0	4.7	5.0	2.9	6.5	0.0	4.6
97.8	603.2	24.0	7.0	3.6	0.7	5.1	5.3	3.6	6.8	0.0	5.0
98.0	653.6	24.9	7.2	4.1	2.3	5.5	5.6	4.2	7.1	0.0	5.4
98.2	703.1	25.7	7.5	4.6	3.1	5.9	5.9	4.6	7.4	0.0	5.8
98.4	751.6	26.5	7.7	5.1	3.7	6.2	6.1	5.1	7.6	0.0	6.1
98.6	799.4	27.3	7.9	5.4	4.2	6.5	6.3	5.5	7.8	0.0	6.5
98.8	846.3	28.0	8.1	5.8	4.7	6.8	6.6	5.8	8.1	0.0	6.7
99.0	892.5	28.7	8.3	6.1	5.1	7.1	6.8	6.1	8.3	0.0	7.0
99.2	937.9	29.3	8.5	6.4	5.5	7.3	6.9	6.4	8.4	0.0	7.3
99.4	982.6	29.9	8.7	6.7	5.8	7.6	7.1	6.7	8.6	0.0	7.5
99.6	1026.6	30.5	8.8	7.0	6.1	7.8	7.3	7.0	8.8	0.9	7.7
99.8	1069.9	31.1	9.0	7.2	6.4	8.0	7.4	7.2	9.0	2.2	8.0
100.0	1112.6	31.6	9.2	7.5	6.7	8.2	7.6	7.5	9.1	2.9	8.2
100.2	1154.7	32.1	9.3	7.7	6.9	8.4	7.7	7.7	9.3	3.5	8.4
100.4	1196.1	32.6	9.4	7.9	7.2	8.6	7.9	7.9	9.4	4.0	8.5
100.6	1237.0	33.1	9.6	8.1	7.4	8.8	8.0	8.1	9.6	4.4	8.7
100.8	1277.3	33.6	9.7	8.3	7.6	8.9	8.1	8.3	9.7	4.8	8.9
101.0	1317.0	34.0	9.8	8.5	7.8	9.1	8.2	8.5	9.9	5.2	9.1
101.2	1356.2	34.4	10.0	8.7	8.0	9.3	8.3	8.7	10.0	5.5	9.2
101.4	1394.9	34.9	10.1	8.8	8.2	9.4	8.4	8.8	10.1	5.8	9.4
101.6	1433.1	35.3	10.2	9.0	8.4	9.6	8.5	9.0	10.2	6.1	9.5
101.8	1470.9	35.6	10.3	9.1	8.6	9.7	8.6	9.2	10.3	6.3	9.7
102.0	1508.1	36.0	10.4	9.3	8.8	9.8	8.7	9.3	10.4	6.6	9.8

Metal Poor Subdwarfs:

Inclination	Altitude	HD224930	HD76932
		28.4	-18.0
96.0	101.4	0.0	0.0
96.2	162.1	0.0	0.0
96.4	221.5	0.0	0.0
96.6	279.5	0.0	0.0
96.8	336.3	0.0	0.0
97.0	391.9	0.0	0.0

97.2	446.3	0.0	0.0
97.4	499.6	1.8	0.0
97.6	551.9	2.8	0.0
97.8	603.2	3.5	0.0
98.0	653.6	4.1	0.0
98.2	703.1	4.6	0.0
98.4	751.6	5.0	0.7
98.6	799.4	5.4	1.7
98.8	846.3	5.8	2.3
99.0	892.5	6.1	2.8
99.2	937.9	6.4	3.2
99.4	982.6	6.7	3.5
99.6	1026.6	7.0	3.8
99.8	1069.9	7.2	4.0
100.0	1112.6	7.4	4.2
100.2	1154.7	7.7	4.5
100.4	1196.1	7.9	4.6
100.6	1237.0	8.1	4.8
100.8	1277.3	8.3	5.0
101.0	1317.0	8.5	5.1
101.2	1356.2	8.6	5.3
101.4	1394.9	8.8	5.4
101.6	1433.1	9.0	5.5
101.8	1470.9	9.1	5.7
102.0	1508.1	9.3	5.8

Wolf Rayet Stars:

Inclination	Altitude	WR 113	WR 128	WR 123
		-20.5	11.0	-16.3
96.0	101.4	0.0	2.6	0.0
96.2	162.1	0.0	3.4	0.0
96.4	221.5	0.0	4.1	0.0
96.6	279.5	0.0	4.7	0.0
96.8	336.3	0.0	5.1	0.0
97.0	391.9	0.0	5.6	0.0
97.2	446.3	0.0	5.9	0.0
97.4	499.6	0.0	6.3	0.0
97.6	551.9	0.0	6.6	0.0
97.8	603.2	0.0	6.9	0.0
98.0	653.6	0.0	7.2	1.6
98.2	703.1	0.0	7.4	2.3
98.4	751.6	0.0	7.7	2.9
98.6	799.4	0.0	7.9	3.3
98.8	846.3	0.0	8.1	3.6

99.0	892.5	0.0	8.3	3.9
99.2	937.9	0.0	8.5	4.2
99.4	982.6	0.5	8.7	4.5
99.6	1026.6	1.5	8.8	4.7
99.8	1069.9	2.0	9.0	4.9
100.0	1112.6	2.4	9.2	5.1
100.2	1154.7	2.8	9.3	5.3
100.4	1196.1	3.1	9.5	5.5
100.6	1237.0	3.3	9.6	5.6
100.8	1277.3	3.5	9.7	5.8
101.0	1317.0	3.7	9.9	5.9
101.2	1356.2	3.9	10.0	6.0
101.4	1394.9	4.1	10.1	6.2
101.6	1433.1	4.2	10.2	6.3
101.8	1470.9	4.4	10.3	6.4
102.0	1508.1	4.5	10.4	6.5

Ro-Ap stars:

Inclination	Altitude	HR 1217	Gam Equ	HD176232
		-13.5	12.0	26.6
96.0	101.4	0.0	2.4	0.0
96.2	162.1	0.0	3.3	0.0
96.4	221.5	0.0	4.0	0.0
96.6	279.5	0.0	4.6	0.0
96.8	336.3	0.0	5.1	0.0
97.0	391.9	0.0	5.5	0.0
97.2	446.3	0.7	5.9	2.2
97.4	499.6	2.0	6.2	3.1
97.6	551.9	2.7	6.6	3.8
97.8	603.2	3.2	6.8	4.3
98.0	653.6	3.7	7.1	4.8
98.2	703.1	4.0	7.4	5.2
98.4	751.6	4.4	7.6	5.6
98.6	799.4	4.7	7.9	5.9
98.8	846.3	4.9	8.1	6.3
99.0	892.5	5.2	8.3	6.6
99.2	937.9	5.4	8.5	6.8
99.4	982.6	5.6	8.6	7.1
99.6	1026.6	5.8	8.8	7.3
99.8	1069.9	6.0	9.0	7.6
100.0	1112.6	6.1	9.2	7.8
100.2	1154.7	6.3	9.3	8.0
100.4	1196.1	6.4	9.5	8.2
100.6	1237.0	6.6	9.6	8.4

100.8	1277.3	6.7	9.7	8.6
101.0	1317.0	6.8	9.9	8.8
101.2	1356.2	7.0	10.0	8.9
101.4	1394.9	7.1	10.1	9.1
101.6	1433.1	7.2	10.2	9.2
101.8	1470.9	7.3	10.3	9.4
102.0	1508.1	7.4	10.4	9.5

Appendix D: Maps of Trapped Protons and Electrons in the MOST Baseline Orbit

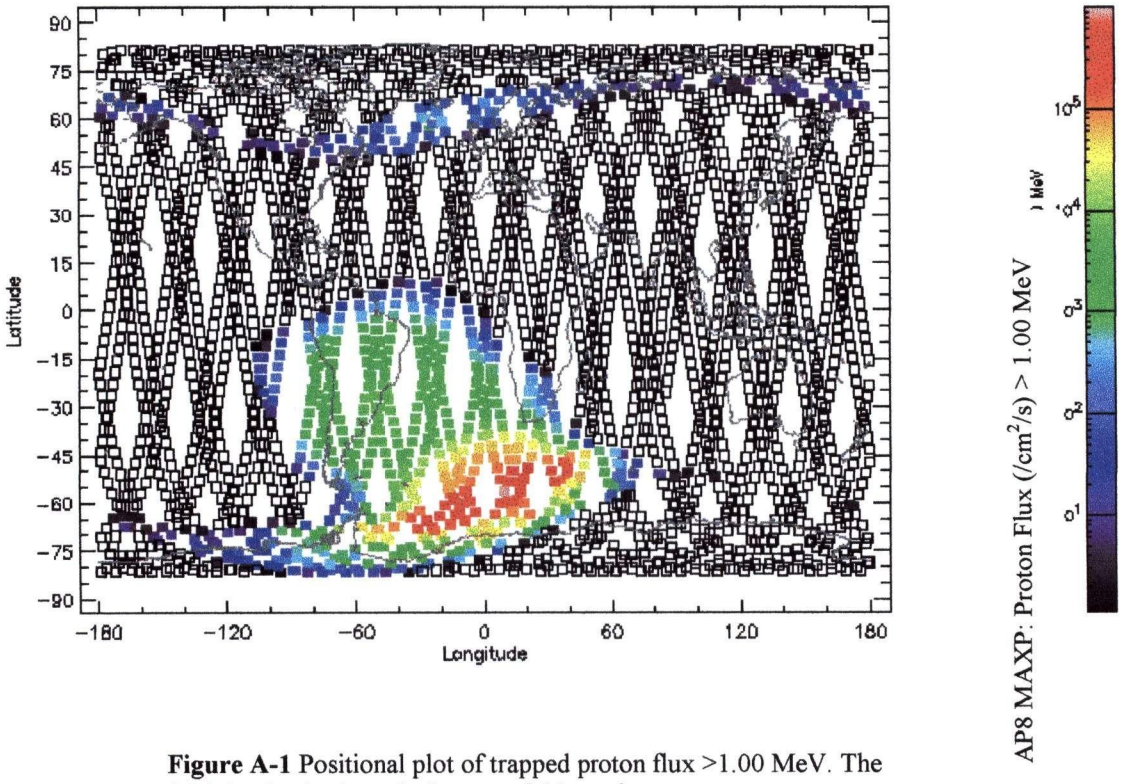

Figure A-1 Positional plot of trapped proton flux >1.00 MeV. The SAA is clearly the only feature of this environment.

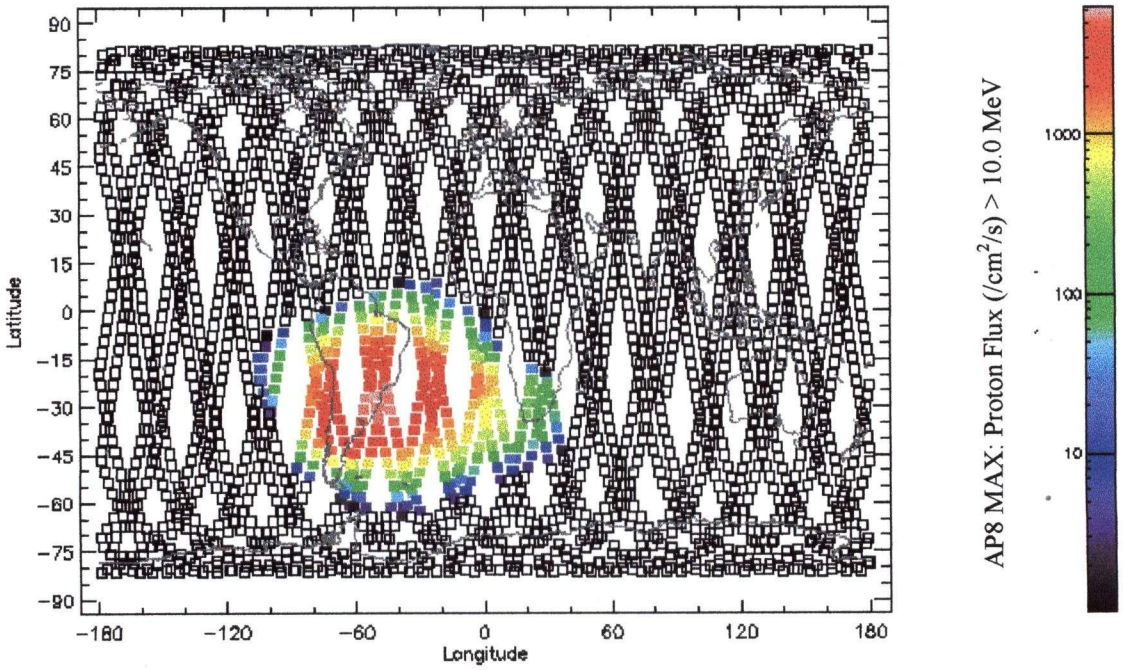

Figure A-2 Positional plot of trapped proton flux > 10 MeV.

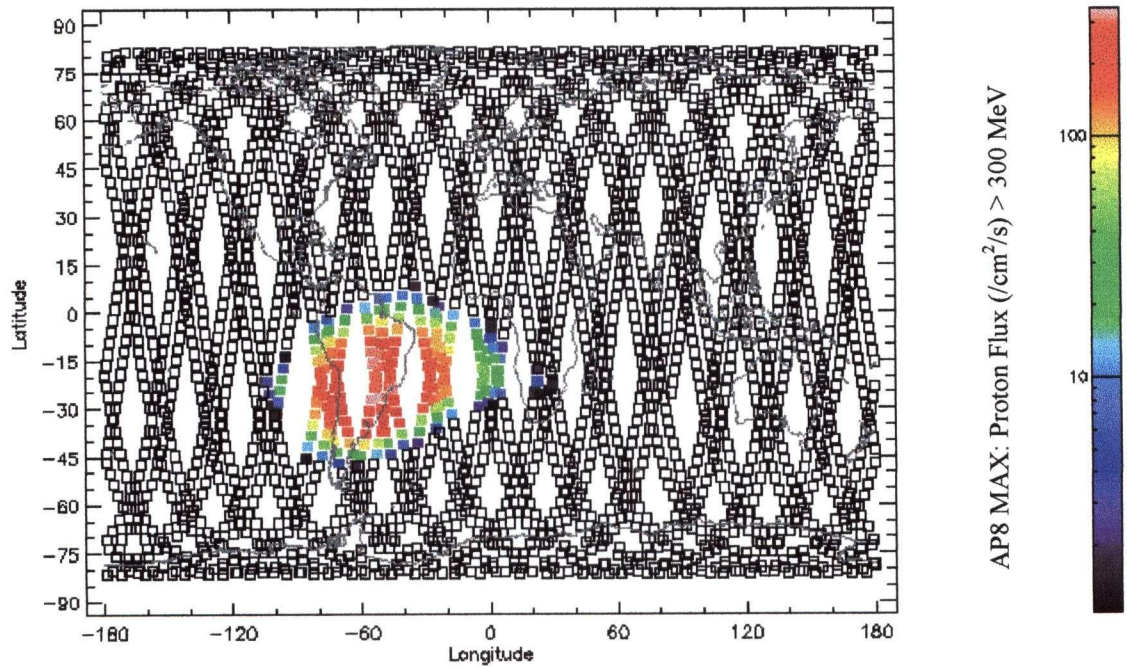

Figure A-3 Positional plot of trapped proton flux > 300 MeV. Higher energy protons remain confined to a smaller portion of the radiation belt.

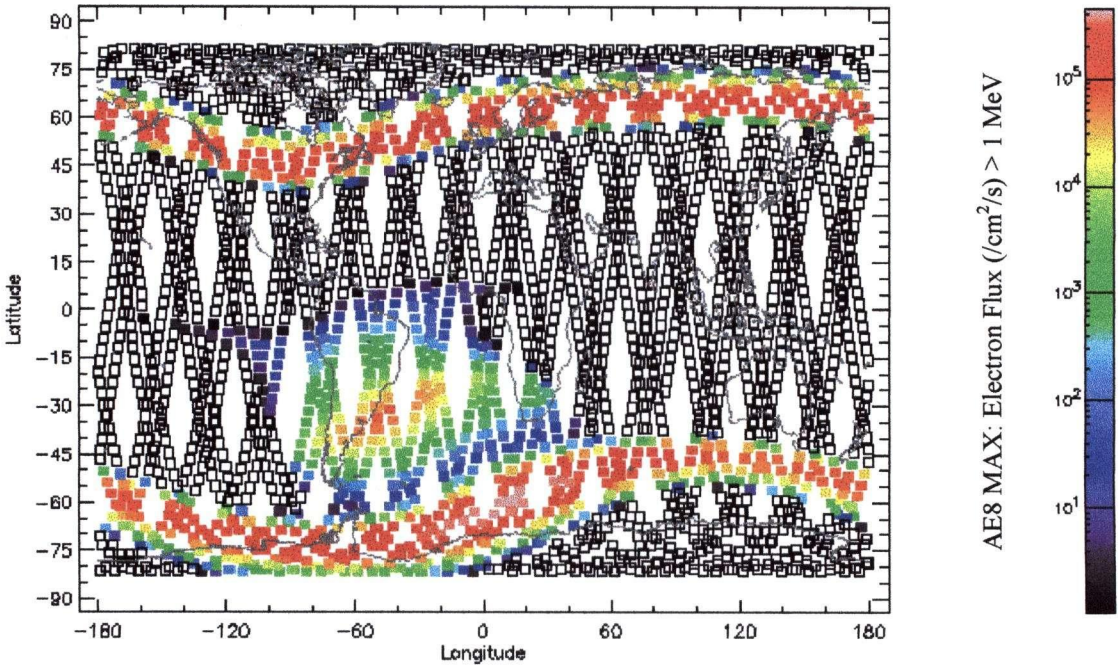

Figure A-4 Positional plot of trapped electron flux > 1.0 MeV. Bands in high and low latitudes are a result of the outer radiation belt penetrating to lower altitude.

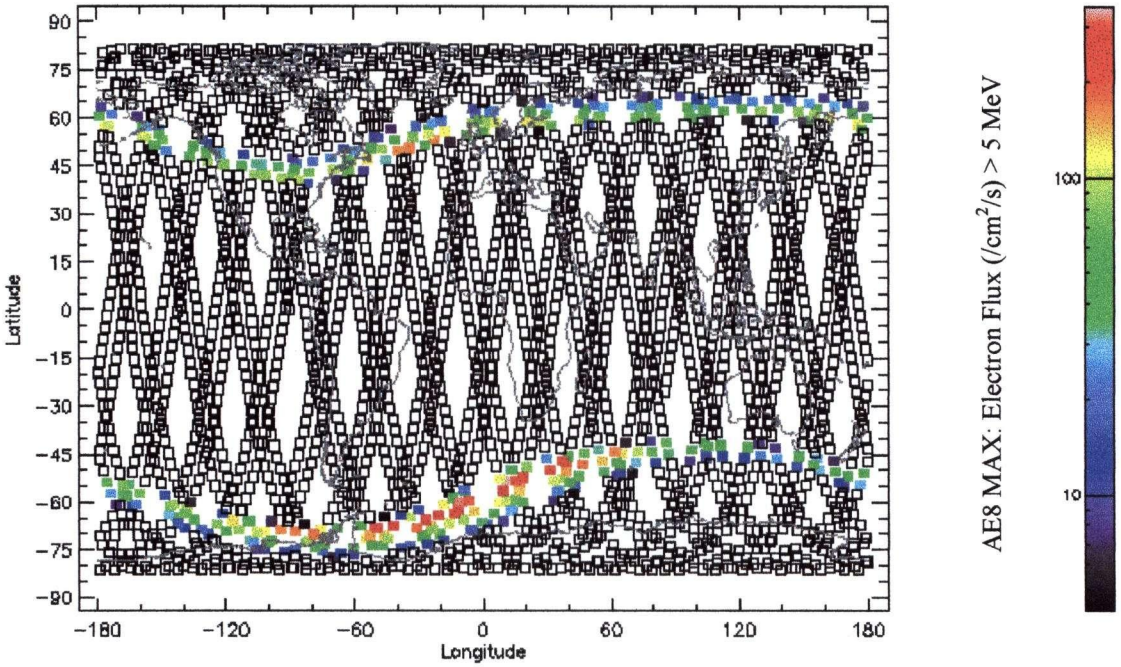

Figure A-5 Positional plot of trapped electron flux > 5.0 MeV. High-energy electrons are not found in the SAA.

Appendix E: Cumulative Doses for the MOST Microsatellite

Description of Radiation Models

	A	B	F	J	P	W
Mission Duration	3.15E+07	3.15E+07	3.15E+07	3.15E+07	3.15E+07	3.15E+07
Geomagnetospheric Conditions	normal	normal	normal	normal	normal	normal
Spacecraft Shielding	Al Cylinder	Al Cylinder	Al Cylinder	Al Cylinder	Ti Cylinder	Al Cylinder
Thickness (mm)	5	5	5	5	2	8
Inner Radius (mm)	75	75	75	75	47.5	75
Height (mm)	449	449	449	449	33	449
Radial Distance (mm)	0	0	0	0	0	0
Axial Distance (mm)	123	123	123	123	0	123
Solar Cycle	Solar Max	Solar Max	Solar Max	Solar Min	Solar Max	Solar Max
Geomagnetic Reference Field	IGRF2000	IGRF2000	IGRF	IGRF	IGRF	IGRF
Epoch	2000	2002	0	0	0	0
Solar Proton Model	JPL91	JPL91	JPL91	JPL91	JPL91	JPL91
Confidence Level	97%	97%	97%	97%	97%	97%

Heavy Ion/Proton Ionising Dose

Trapped Protons (rad/yr Si)	369	422	369	503	516	306
Solar Protons (rad/yr Si)	410	410	410	410	964	231
Galactic Cosmic Radiation (rad/yr Si)	1.54	1.54	1.54	3.65	1.58	1.51

Electron Ionising Dose

Primary Electrons	177	170	177	103	2620	7.14
Bremmstrahlung	8.79	11.6	8.79	5.31	24.2	8
Total Electron Dose	185.79	181.6	185.79	108	2644.2	15.1
TOTAL IONISING DOSE	966.33	1015.14	966.33	1024.65	4125.78	553.61

Displacement Damage

Trapped Protons (rad/yr Si)	3.30E-01	1.60E-01	3.30E-01	1.94E-01	1.85E-01	1.23E-01
Solar Protons (rad/yr Si)	5.37E-01	5.37E-01	5.37E-01	1.20E-01	2.68E-01	7.01E-02
Galactic Cosmic Radiation (rad/yr Si)	5.13E-04	5.13E-04	5.12E-04	1.20E-03	5.12E-04	5.12E-04
TOTAL DISPLACEMENT DOSE (rad/yr Si)	8.68E-01	6.98E-01	8.68E-01	3.15E-01	4.54E-01	1.94E-01
TOTAL DISPLACEMENT DOSE (1 MeV proton equivalents (protons/cm^2)	8.76E+08	7.05E+08	8.76E+08	3.18E+08	4.58E+08	1.96E+08

Doses due to SEP as modelled by the CREME code

Solar Energetic Particle Model	Ordinary Scenario	90% Worst Case Scenario	1972 Scenario	Composite Worst Case Scenario
Spacecraft Shielding	Al Cylinder	Al Cylinder	Al Cylinder	Al Cylinder
Thickness (mm)	5	5	5	5
Geomagnetospheric Conditions	normal	normal	normal	normal
Ionising Dose (rad/day Si)	9.03E-01	5.95	318	348
Displacement Dose (rad/day Si)	2.71E-04	1.75E-03	9.69E-02	1.22E-01

Solar Energetic Particle Model	Ordinary Scenario	90% Worst Case Scenario	1972 Scenario	Composite Worst Case Scenario
Spacecraft Shielding	Al Cylinder	Al Cylinder	Al Cylinder	Al Cylinder
Thickness (mm)	5	5	5	5
Geomagnetospheric Conditions	stormy	stormy	stormy	stormy
Ionising Dose (rad/day Si)	1.14	7.55	402	436
Displacement Dose (rad/day Si)	3.42E-04	2.22E-03	1.22E-01	1.50E-01

Solar Energetic Particle Model	Ordinary Scenario	90% Worst Case Scenario	1972 Scenario	Composite Worst Case Scenario
Spacecraft Shielding	Al Cylinder	Al Cylinder	Al Cylinder	Al Cylinder
Thickness (mm)	5	5	5	5
Geomagnetospheric Conditions	worst	worst	worst	worst
Ionising Dose (rad/day Si)	4.18	27.7	1460	1550
Displacement Dose (rad/day Si)	1.23E-03	8.03E-03	4.38E-01	5.10E-01

Solar Energetic Particle Model	Ordinary Scenario	90% Worst Case Scenario	1972 Scenario	Composite Worst Case Scenario
Spacecraft Shielding	Ti Cylinder	Ti Cylinder	Ti Cylinder	Ti Cylinder
Thickness (mm)	2	2	2	2
Geomagnetospheric Conditions	normal	normal	normal	normal
Ionising Dose (rad/day Si)	2.5	13.7	635	665
Displacement Dose (rad/day Si)	7.07E-04	3.86E-03	1.83E-01	2.08E-01

Solar Energetic Particle Model	Ordinary Scenario	90% Worst Case Scenario	1972 Scenario	Composite Worst Case Scenario
Spacecraft Shielding	Al Cylinder	Al Cylinder	Al Cylinder	Al Cylinder
Thickness (mm)	8	8	8	8
Geomagnetospheric	normal	normal	normal	normal

Conditions				
Ionising Dose (rad/day Si)	5.68E-01	3.65	199	230
Displacement Dose (rad/day Si)	1.76E-04	1.10E-03	6.35E-02	8.85E-02

Appendix F: Specifications Sheet for Marconi CCD47-20

Note: This is the specifications sheet for the commercial off-the-shelf model. The MOST CCD is custom designed as weel as custom packaged so the specifications found here may not be representative of the MOST CCD. For details on the MOST CCD see Section 1.3.1.

EEV

CCD47-20
High Performance CCD Sensor

FEATURES

- 1024 by 1024 1:1 Image Format
- Image Area 13.3 x 13.3 mm
- Frame Transfer Operation
- 13 µm Square Pixels
- Symmetrical Anti-static Gate Protection
- Very Low Noise Output Amplifiers
- Gated Dump Drain on Output Register
- 100% Active Area

APPLICATIONS

- Spectroscopy
- Scientific Imaging
- Star Tracking
- Medical Imaging

INTRODUCTION

This version of the CCD47-20 is a front-face illuminated, frame transfer CCD sensor with high performance low noise output amplifiers, suitable for use in slow-scan imaging systems. The image area contains a full 1024 by 1024 pixels which are 13 µm square. The output register is split, allowing either or both of the two output amplifiers to be employed, and is provided with a drain and control gate for charge dump purposes.

In common with all EEV CCD Sensors, the CCD47-20 is available with a fibre-optic window or taper, a UV coating or a phosphor coating for X-ray detection. Other variants of the CCD47-20 include IMO, back-thinned and full-frame devices.

Designers are advised to consult EEV should they be considering using CCD sensors in abnormal environments or if they require customised packaging.

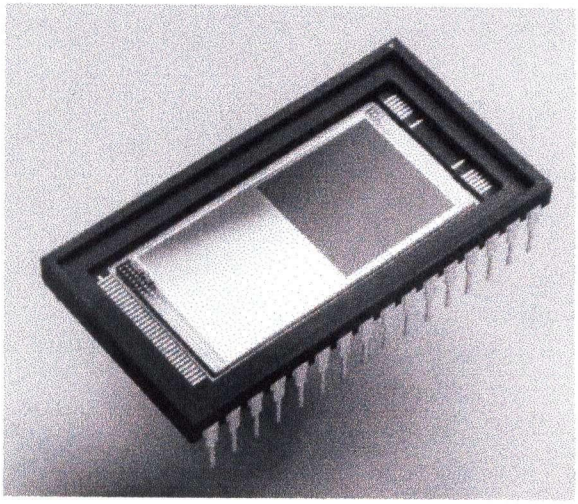

TYPICAL PERFORMANCE

Maximum readout frequency	5	MHz
Output responsivity	4.5	µV/e⁻
Peak signal	120	ke⁻/pixel
Dynamic range (at 20 kHz)	~60 000:1	
Spectral range	400 - 1100	nm
Readout noise (at 20 kHz)	2.0	e⁻ rms
QE at 700 nm	45	%

GENERAL DATA

Format

Image area	13.3 x 13.3	mm
Active pixels (H)	1024	
(V)	1024	
Pixel size	13 x 13	µm
Storage area	13.3 x 13.3	mm
Pixels (H)	1024	
(V)	1024	

Additional pixels are provided in both the image and storage areas for dark reference and over-scanning purposes.

Number of output amplifiers	2	
Weight (approx, no window)	7.5	g

Package

Package size	22.7 x 42.0 mm
Number of pins	32
Inter-pin spacing	2.54 mm
Window material	quartz or removable glass
Type	ceramic DIL array

EEV Limited, Waterhouse Lane, Chelmsford, Essex CM1 2QU England Telephone: +44 (0)1245 493493 Facsimile: +44 (0)1245 492492 e-mail: info@eev.com
Internet: www.eev.com Holding Company: The General Electric Company, p.l.c. A member of the Marconi Electro-Optics Group.

EEV, Inc. 4 Westchester Plaza, PO Box 1482, Elmsford, NY10523-1482 USA Telephone: (914) 592-6050 Facsimile: (914) 682-8922 e-mail: info@eevinc.com

PERFORMANCE

	Min	Typical	Max	
Peak charge storage (see note 1)	80k	120k	-	e^-/pixel
Peak output voltage (no binning)	-	540	-	mV
Dark signal at 293 K (see notes 2 and 3)	-	10k	20k	e^-/pixel/s
Dynamic range (see note 4)	-	60 000	-	
Charge transfer efficiency (see note 5):				
parallel	-	99.9999	-	%
serial	-	99.9993	-	%
Output amplifier responsivity (see note 3)	3.0	4.5	6.0	$\mu V/e^-$
Readout noise at 243 K (see notes 3 and 6):				
grade 0 and 1	-	2.0	4.0	rms e^-/pixel
grade 2	-	3.0	6.0	rms e^-/pixel
Maximum readout frequency (see note 7)	-	5.0	-	MHz
Response non-uniformity (std. deviation)	-	3	10	% of mean
Dark signal non-uniformity (std. deviation) (see notes 3 and 8)	-	1000	2000	e^-/pixel/s

ELECTRICAL INTERFACE CHARACTERISTICS

Electrode capacitances (measured at mid-clock level)

	Min	Typical	Max	
SØ/SØ interphase	-	3.5	-	nF
IØ/IØ interphase	-	3.5	-	nF
IØ/SS and SØ/SS	-	4.5	-	nF
RØ/RØ interphase	-	40	-	pF
RØ/(SS+DG+OD)	-	60	-	pF
ØR/SS	-	10	-	pF
Output impedance (at typ. operating condition)	-	300	-	Ω

NOTES

1. Signal level at which resolution begins to degrade.
2. Measured between 233 and 253 K and V_{SS} +9.0 V. Dark signal at any temperature T (kelvin) may be estimated from:
   $$Q_d/Q_{d0} = 122T^3e^{-6400/T}$$
   where Q_{d0} is the dark signal at T = 293 K (20 °C).
3. Test carried out at EEV on all sensors.
4. Dynamic range is the ratio of readout noise to full well capacity measured at 243 K and 20 kHz readout speed.
5. CCD characterisation measurements made using charge generated by X-ray photons of known energy.
6. Measured using a dual-slope integrator technique (i.e. correlated double sampling) with a 20 µs integration period.
7. Readout at speeds in excess of 5 MHz into a 15 pF load can be achieved but performance to the parameters given cannot be guaranteed.
8. Measured between 233 and 253 K, excluding white defects.

BLEMISH SPECIFICATION

Traps Pixels where charge is temporarily held. Traps are counted if they have a capacity greater than 200 e^- at 243 K.

Slipped columns Are counted if they have an amplitude greater than 200 e^-.

Black spots Are counted when they have a signal level of less than 90% of the local mean at a signal level of approximately half full-well.

White spots Are counted when they have a generation rate 25 times the specified maximum dark signal generation rate (measured between 233 and 253 K). The amplitude of white spots will vary in the same manner as dark current, i.e.:
$$Q_d/Q_{d0} = 122T^3e^{-6400/T}$$

White column A column which contains at least 21 white defects.

Black column A column which contains at least 21 black defects.

GRADE	0	1	2
Column defects:			
black or slipped	0	2	6
white	0	0	0
Black spots	15	25	100
Traps > 200 e^-	1	2	5
White spots	20	30	50

Grade 5 Devices which are fully functioning, with image quality below that of grade 2, and which may not meet all other performance parameters.

Minimum separation between adjacent black columns . . . . . 50 pixels

Note The effect of temperature on defects is that traps will be observed less at higher temperatures but more may appear below 233 K. The amplitude of white spots and columns will decrease rapidly with temperature.

TYPICAL OUTPUT CIRCUIT NOISE
(Measured using clamp and sample)

V_{SS} = 9 V V_{RD} = 18 V V_{OD} = 29 V

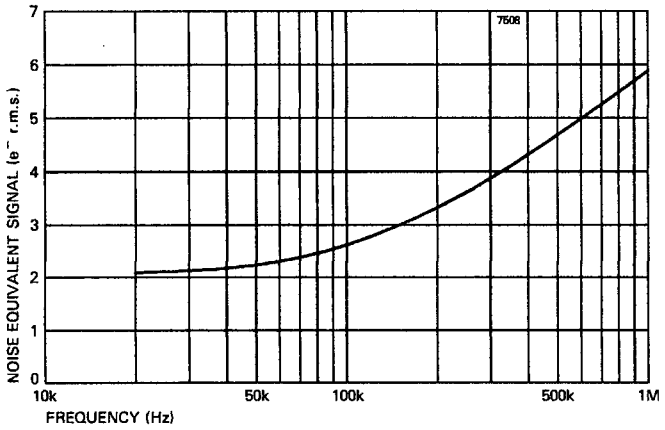

TYPICAL SPECTRAL RESPONSE
(No window)

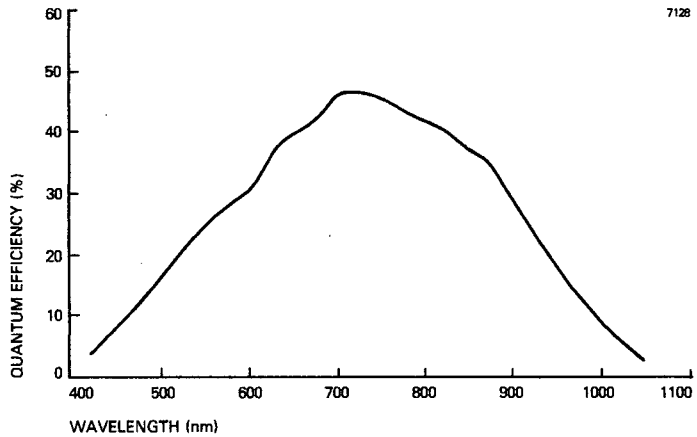

TYPICAL VARIATION OF DARK SIGNAL WITH SUBSTRATE VOLTAGE
(Two I∅ phases held low)

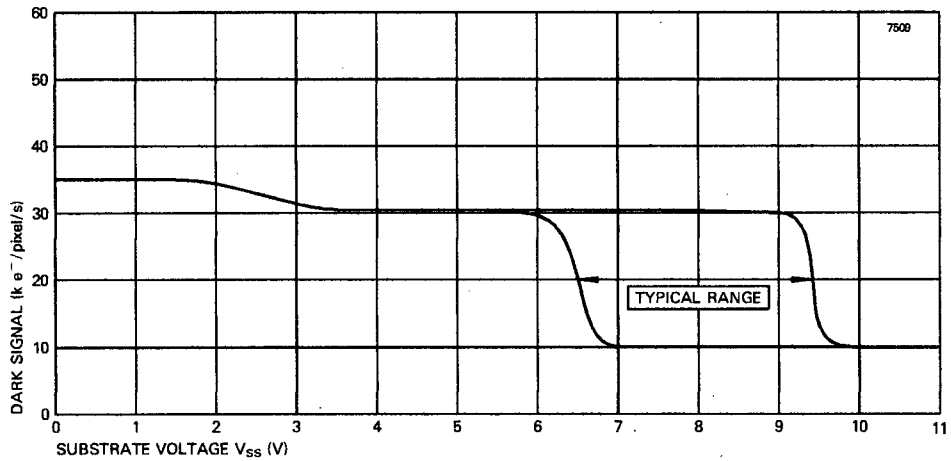

TYPICAL VARIATION OF DARK CURRENT WITH TEMPERATURE

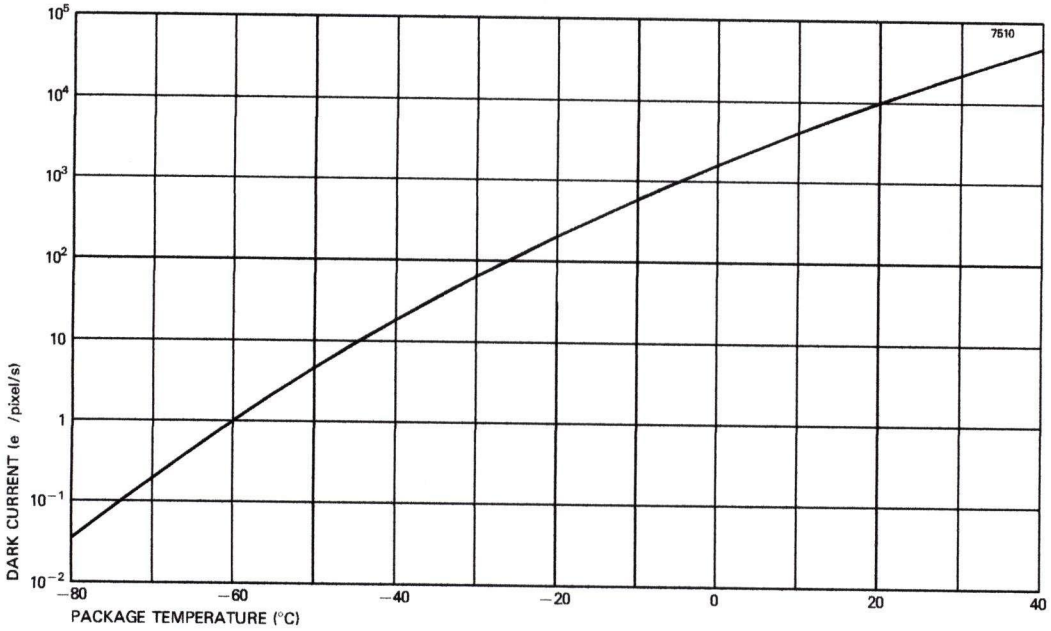

DEVICE SCHEMATIC

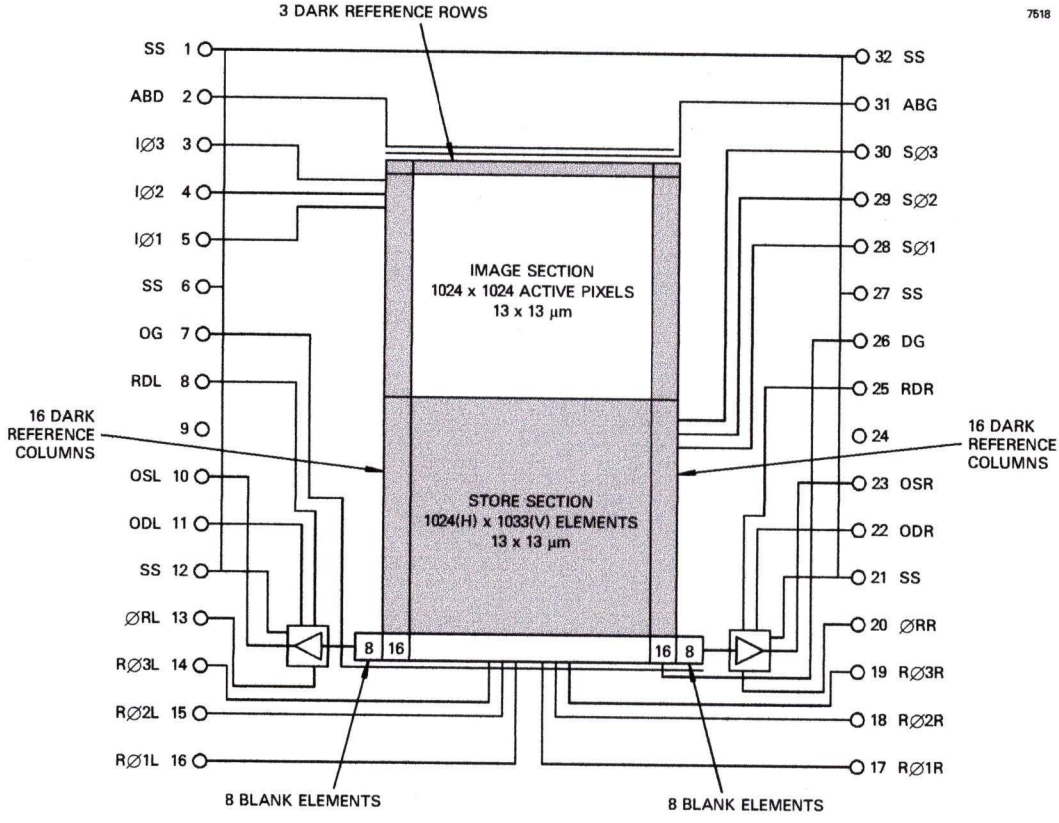

CONNECTIONS, TYPICAL VOLTAGES AND ABSOLUTE MAXIMUM RATINGS

PIN	REF	DESCRIPTION	PULSE AMPLITUDE OR DC LEVEL (V) (See note 9)			MAXIMUM RATINGS with respect to V_{SS}
			Min	Typical	Max	
1	SS	Substrate	0	9	10	-
2	ABD	Anti-blooming drain (see note 10)		V_{OD}		−0.3 to +25 V
3	IØ3	Image area clock	8	12	15	±20 V
4	IØ2	Image area clock	8	12	15	±20 V
5	IØ1	Image area clock	8	12	15	±20 V
6	SS	Substrate	0	9	10	-
7	OG	Output gate	1	3	5	±20 V
8	RDL	Reset transistor drain (left amplifier)	15	17	19	−0.3 to +25 V
9	-	No connection		-		-
10	OSL	Output transistor source (left amplifier)		see note 11		−0.3 to +25 V
11	ODL	Output transistor drain (left amplifier)	27	29	31	−0.3 to +35 V
12	SS	Substrate	0	9	10	-
13	ØRL	Output reset pulse (left amplifier)	8	12	15	±20 V
14	RØ3L	Output register clock (left section)	8	10	15	±20 V
15	RØ2L	Output register clock (left section)	8	10	15	±20 V
16	RØ1L	Output register clock (left section)	8	10	15	±20 V
17	RØ1R	Output register clock (right section)	8	10	15	±20 V
18	RØ2R	Output register clock (right section)	8	10	15	±20 V
19	RØ3R	Output register clock (right section)	8	10	15	±20 V
20	ØRR	Output reset pulse (right amplifier)	8	12	15	±20 V
21	SS	Substrate	0	9	10	-
22	ODR	Output transistor drain (right amplifier)	27	29	31	−0.3 to +35 V
23	OSR	Output transistor source (right amplifier)		see note 11		−0.3 to +25 V
24	-	No connection		-		-
25	RDR	Reset transistor drain (right amplifier)	15	17	19	−0.3 to +25 V
26	DG	Dump gate (see note 12)	-	0	-	±20 V
27	SS	Substrate	0	9	10	-
28	SØ1	Storage area clock	8	12	15	±20 V
29	SØ2	Storage area clock	8	12	15	±20 V
30	SØ3	Storage area clock	8	12	15	±20 V
31	ABG	Anti-blooming gate	0	0	5	±20 V
32	SS	Substrate	0	9	10	-

Maximum voltages between pairs of pins:

pin 10 (OSL) to pin 11 (ODL)	±15	V
pin 22 (ODR) to pin 23 (OSR)	±15	V
Maximum output transistor current	10	mA

NOTES

9. Readout register clock pulse low levels +1 V; other clock low levels 0±0.5 V.
10. Drain not incorporated, but bias is still necessary.
11. 3 to 5 V below OD. Connect to ground using a 2 to 5 mA current source or appropriate load resistor (typically 5 to 10 kΩ).
12. Non-charge dumping level shown. For operation in charge dumping mode, DG should be pulsed to 12 ± 2 V.
13. All devices will operate at the typical values given. However, some adjustment within the minimum to maximum range may be required for to optimise performance for critical applications. It should be noted that conditions for optimum performance may differ from device to device.
14. With the RØ connections shown, the device will operate through the left hand output only. In order to operate from both outputs RØ1(R) and RØ2(R) should be reversed.

FRAME TRANSFER TIMING DIAGRAM

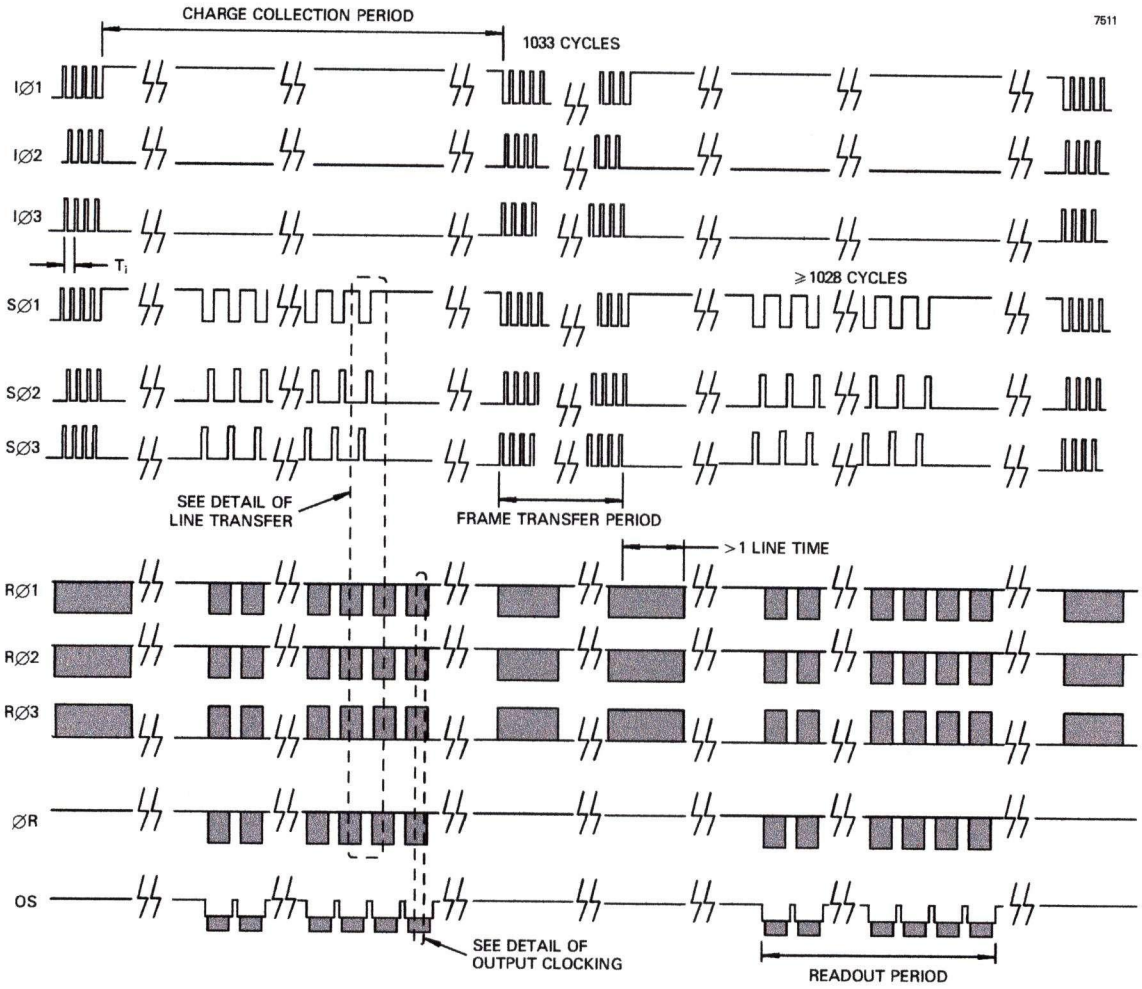

DETAIL OF LINE TRANSFER

(For output from a single amplifier)

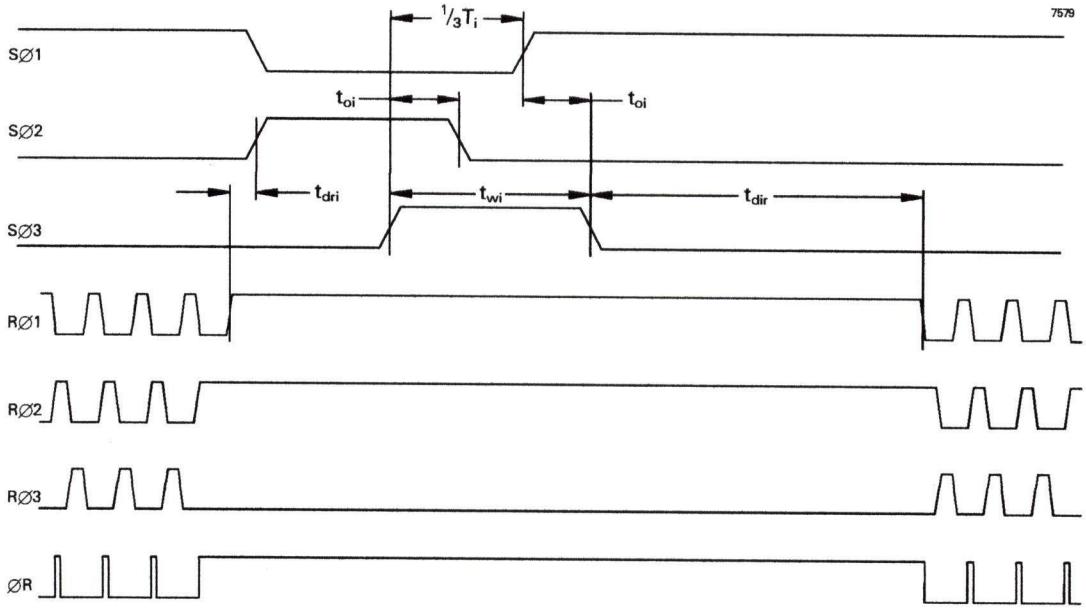

DETAIL OF VERTICAL LINE TRANSFER (Single line dump)

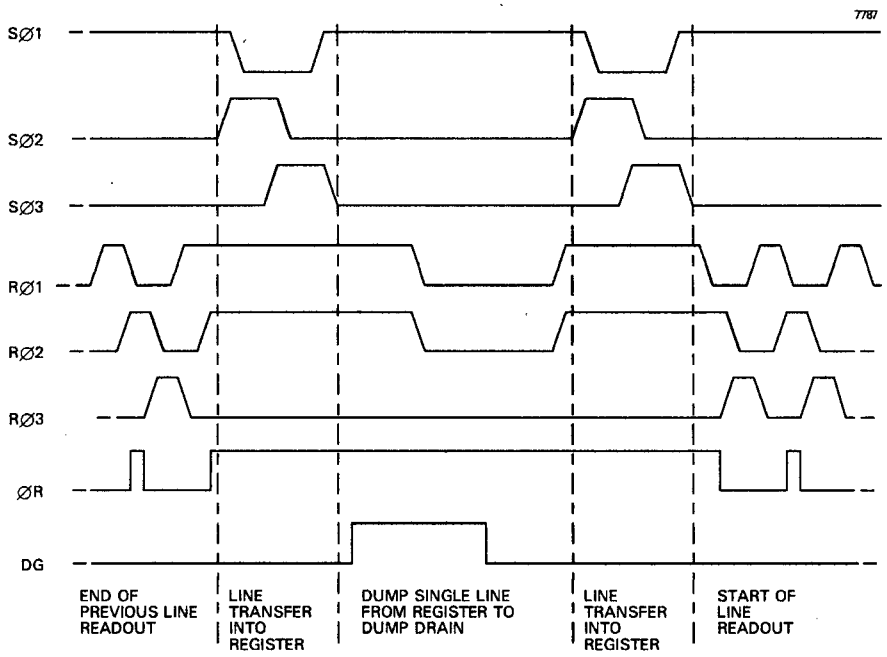

DETAIL OF VERTICAL LINE TRANSFER (Multiple line dump)

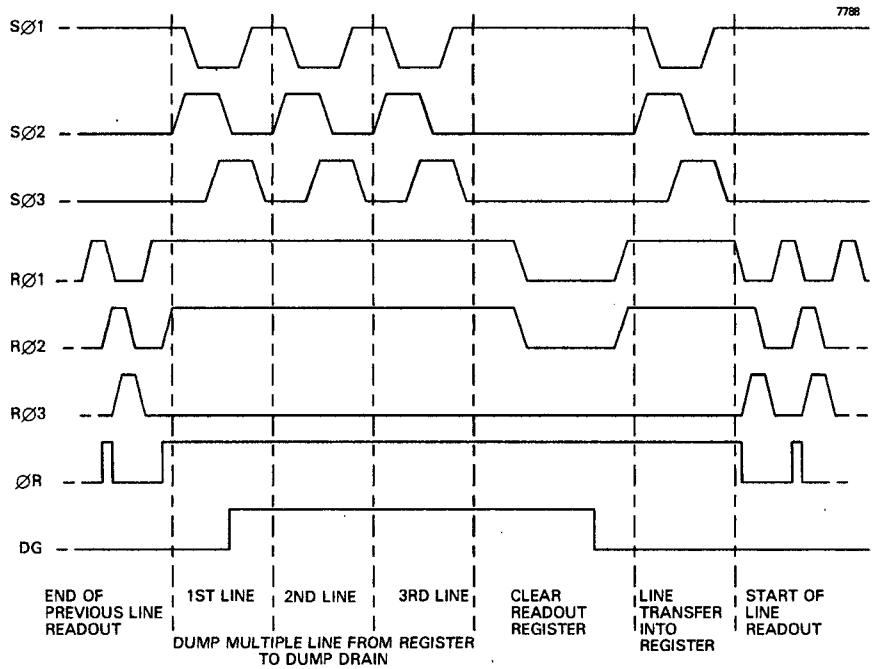

DETAIL OF OUTPUT CLOCKING

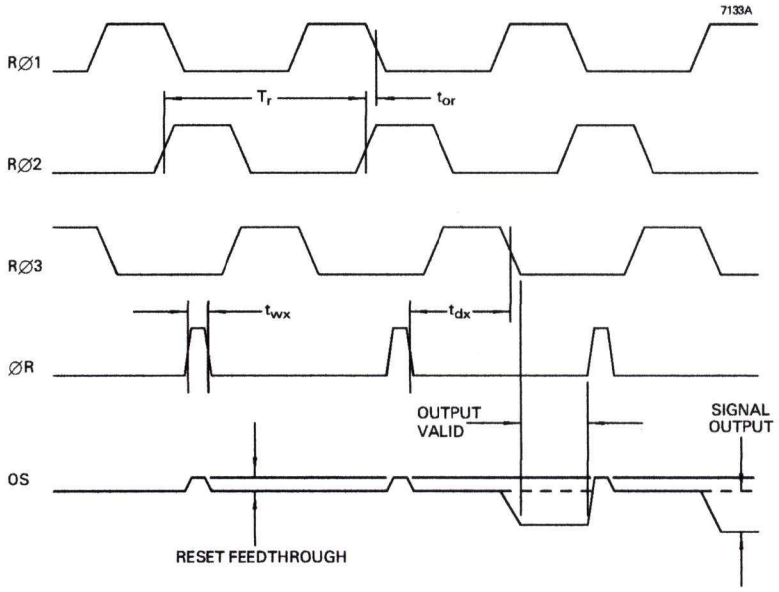

LINE OUTPUT FORMAT

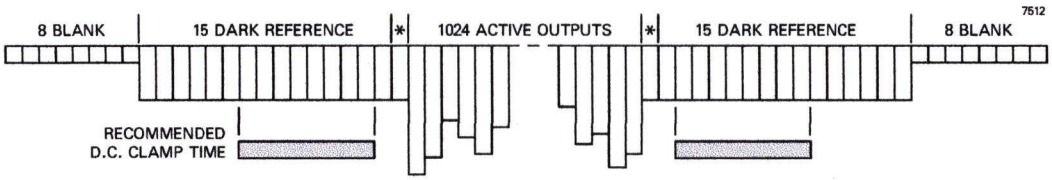

* = Partially shielded transition elements

CLOCK TIMING REQUIREMENTS

Symbol	Description	Min	Typical	Max	
T_i	Image clock period	2	5	see note 15	µs
t_{wi}	Image clock pulse width	1	2.5	see note 15	µs
t_{ri}	Image clock pulse rise time (10 to 90%)	0.1	0.5	$0.2T_i$	µs
t_{fi}	Image clock pulse fall time (10 to 90%)	t_{ri}	0.5	$0.2T_i$	µs
t_{oi}	Image clock pulse overlap	$(t_{ri}+t_{fi})/2$	0.5	$0.2T_i$	µs
t_{dir}	Delay time, SØ stop to RØ start	1	2	see note 15	µs
t_{dri}	Delay time, RØ stop to SØ start	1	1	see note 15	µs
T_r	Output register clock cycle period	200	1000	see note 15	ns
t_{rr}	Clock pulse rise time (10 to 90%)	50	$0.1T_r$	$0.3T_r$	ns
t_{fr}	Clock pulse fall time (10 to 90%)	t_{rr}	$0.1T_r$	$0.3T_r$	ns
t_{or}	Clock pulse overlap	20	$0.5t_{rr}$	$0.1T_r$	ns
t_{wx}	Reset pulse width	30	$0.1T_r$	$0.3T_r$	ns
t_{rx}, t_{fx}	Reset pulse rise and fall times	$0.2t_{wx}$	$0.5t_{rr}$	$0.1T_r$	ns
t_{dx}	Delay time, ØR low to RØ3 low	30	$0.5T_r$	$0.8T_r$	ns

NOTES

15. No maximum other than that necessary to achieve an acceptable dark signal at the longer readout times.
16. To minimise dark current, two of the IØ clocks should be held low during integration. IØ timing requirements are identical to SØ (as shown above).

OUTPUT CIRCUIT

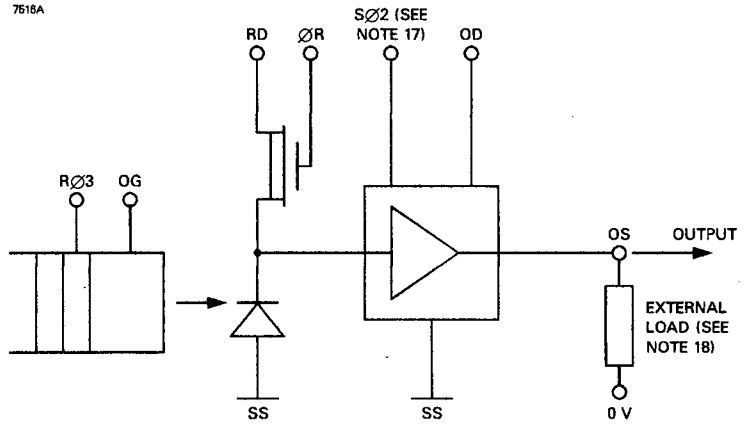

NOTES

17. The amplifier has a DC restoration circuit which is internally activated whenever SØ2 is high.
18. Not critical; can be a 2 to 5 mA constant current supply or an appropriate load resistor.

OUTLINE

(All dimensions without limits are nominal)

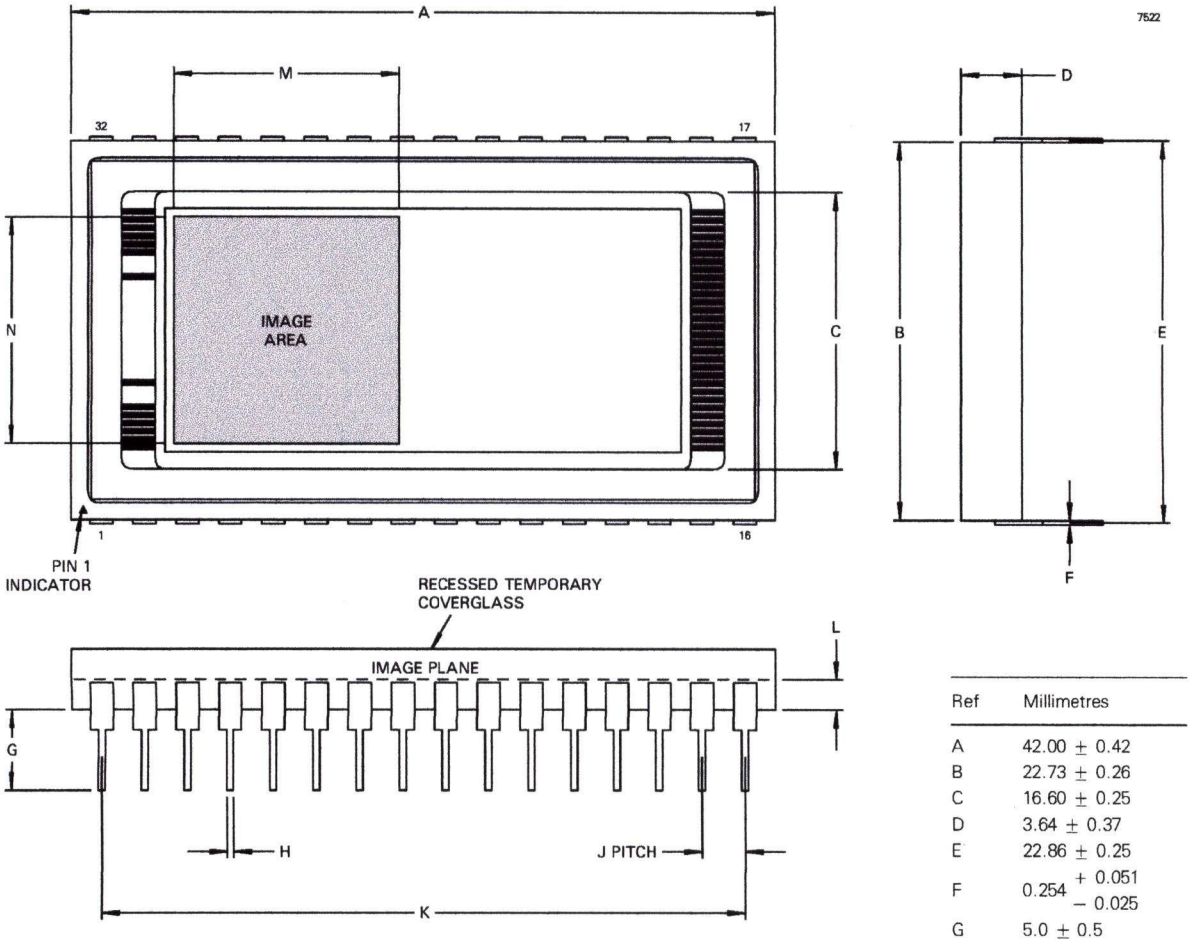

Ref	Millimetres
A	42.00 ± 0.42
B	22.73 ± 0.26
C	16.60 ± 0.25
D	3.64 ± 0.37
E	22.86 ± 0.25
F	$0.254 \begin{smallmatrix} +0.051 \\ -0.025 \end{smallmatrix}$
G	5.0 ± 0.5
H	0.457 ± 0.051
J	2.54 ± 0.13
K	38.1
L	1.65 ± 0.50
M	13.3
N	13.3

ORDERING INFORMATION

Options include:

- Temporary Quartz Window
- Permanent Quartz Window
- Temporary Glass Window
- Permanent Glass Window
- Fibre-optic Coupling
- UV Coating
- X-ray Phosphor Coating

For further information on the performance of these and other options, please contact EEV.

HANDLING CCD SENSORS

CCD sensors, in common with most high performance MOS IC devices, are static sensitive. In certain cases a discharge of static electricity may destroy or irreversibly degrade the device. Accordingly, full antistatic handling precautions should be taken whenever using a CCD sensor or module. These include:-

- Working at a fully grounded workbench
- Operator wearing a grounded wrist strap
- All receiving socket pins to be positively grounded
- Unattended CCDs should not be left out of their conducting foam or socket.

Evidence of incorrect handling will invalidate the warranty. All devices are provided with internal protection circuits to the gate electrodes (pins 3, 4, 5, 7, 13, 14, 15, 16, 17, 18, 19, 20, 26, 28, 29, 30, 31) but not to the other pins.

HIGH ENERGY RADIATION

Device parameters may begin to change if subject to greater than 10^4 rads. This corresponds to:

10^{13} of 15 MeV neutrons/cm^2
2×10^{13} of 1 MeV gamma/cm^2
4×10^{11} of ionising particles/cm^2

Certain characterisation data are held at EEV. Users planning to use CCDs in a high radiation environment are advised to contact EEV.

TEMPERATURE LIMITS

	Min	Typical	Max	
Storage	73	-	373	K
Operating	73	243	323	K

Operation or storage in humid conditions may give rise to ice on the sensor surface on cooling, causing irreversible damage.

Maximum device heating/cooling . . . . 5 K/min